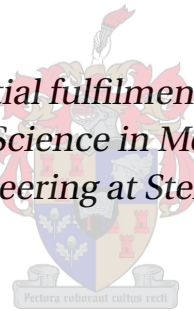


# **Discrete and porous computational fluid dynamics modelling of an air-rock bed thermal energy storage system**

by

André du Randt Louw

*Thesis presented in partial fulfilment of the requirements for the degree of Master of Science in Mechanical Engineering in the Faculty of Engineering at Stellenbosch University*



Department of Mechanical and Mechatronic Engineering,  
University of Stellenbosch,  
Private Bag X1, Matieland 7602, South Africa.

Supervisor: Mr. P. Gauché

April 2014

# Declaration

By submitting this thesis electronically, I declare that the entirety of the work contained therein is my own, original work, that I am the sole author thereof (save to the extent explicitly otherwise stated), that reproduction and publication thereof by Stellenbosch University will not infringe any third party rights and that I have not previously in its entirety or in part submitted it for obtaining any qualification.

Signature: .....

A.D.R. Louw

Date: .....

Copyright © 2014 Stellenbosch University  
All rights reserved.

# Abstract

## **Discrete and porous computational fluid dynamics modelling of an air-rock bed thermal energy storage system**

A.D.R. Louw

*Department of Mechanical and Mechatronic Engineering,  
University of Stellenbosch,  
Private Bag XI, Matieland 7602, South Africa.*

Thesis: MScEng (Mech)

April 2014

Concentrating solar power promises to be a potential solution for meeting the worlds energy needs in the future. One of the key features of this type of renewable energy technology is its ability to store energy effectively and relatively cheaply. An air-rock bed thermal energy storage system promises to be an effective and reasonably inexpensive storage system for concentrating solar power plants. Currently there is no such storage system commercially in operation in any concentrating solar power plant, and further research is required before such a system can be implemented. The main research areas to address are the thermal-mechanical behaviour of rocks, rock bed pressure drop correlations and effective and practical system designs. Recent studies have shown that the pressure drop over a packed bed of rocks is dependant on various aspects such as particle orientation relative to the flow direction, particle shape and surface roughness. The irregularity and unpredictability of the particle shapes make it difficult to formulate a general pressure drop correlation. Typical air-rock bed thermal design concepts consist of a large vertical square or cylindrical vessel in which the bed is contained. Such system designs are simple but susceptible to the ratcheting effect and large pressure drops. Several authors have proposed concepts to over-come these issues, but there remains a need for tools to prove the feasibility of the designs.

The purpose of this paper is to investigate a DEM-CFD coupled approach that can aid the development of an air-rock bed thermal energy storage system. This study specifically focuses on the use of CFD. A complementary study focusses on DEM. The two areas of focus in this study are the pressure drop and system design. A discrete CFD simulation model is used to predict pressure drop over

packed beds containing spherical and irregular particles. DEM is used to create randomly packed beds containing either spherical or irregularly shaped particles. This model is also used to determine the heat transfer between the fluid and particle surface. A porous CFD model is used to model system design concepts. Pressure drop and heat transfer data predicted by the discrete model, is used in the porous model to describe the pressure drop and thermal behaviour of a TES system.

Results from the discrete CFD model shows that it can accurately predict the pressure drop over a packed bed of spheres with an average deviation of roughly 10 % from results found in literature. The heat transfer between the fluid and particle surface also is accurately predicted, with an average deviation of between 13.36 % and 21.83 % from results found in literature. The discrete CFD model for packed beds containing irregular particles presented problems when generating a mesh for the CFD computational domain. The clump logic method was used to represent rock particles in this study. This method was proven by other studies to accurately model the rock particle and the rock packed bed structure using DEM. However, this technique presented problems when generating the surface mesh. As a result a simplified clump model was used to represent the rock particles. This simplified clump model showed characteristics of a packed bed of rocks in terms of pressure drop and heat transfer. However, the results suggest that the particles failed to represent form drag. This was attributed to absence of blunt surfaces and sharp edges of the simplified clump model normally found on rock particles. The irregular particles presented in this study proved to be inadequate for modelling universal characteristics of a packed bed of rocks in terms of pressure drop. The porous CFD model was validated against experimental measurement to predict the thermal behaviour of rock beds. The application of the porous model demonstrated that it is a useful design tool for system design concepts.

# Uittreksel

## Diskrete en poreus numeriese vloed dinamika modellering van 'n lug klip bed termiese energie stoor stelsel

*("Discrete and porous computational fluid dynamics modelling of an air-rock bed thermal energy storage system")*

A.D.R. Louw

*Departement Meganiese en Megatroniese Ingenieurswese,  
Universiteit van Stellenbosch,  
Privaatsak X1, Matieland 7602, Suid Afrika.*

Tesis: MScIng (Meg)

April 2014

Gekonsentreerde sonkrag belof om 'n potensiële toekomstige oplossing te wees vir die wêreld se groeiende energie behoeftes. Een van die belangrikste eienskappe van hierdie tipe hernubare energie tegnologie is die vermoë om energie doeltreffend en relatief goedkoop te stoor. 'n Lug-klipbed termiese energie stoorstelsel belof om 'n doeltreffende en redelik goedkoop stoorstelsel vir gekonsentreerde sonkragstasies te wees. Tans is daar geen sodanige stoorstelsel kommersieël in werking in enige gekonsentreerde sonkragstasie nie. Verdere navorsing is nodig voordat so 'n stelsel in werking gestel kan word. Die belangrikste navorsingsgebiede om aan te spreek is die termies-meganiese gedrag van klippe, klipbed drukverlies korrelasies en effektiewe en praktiese stelsel ontwerpe. Onlangse studies het getoon dat die drukverlies oor 'n gepakte bed van klippe afhanklik is van verskeie aspekte soos partikel oriëntasie tot die vloerigting, partikel vorm en oppervlak grofheid. Die onreëlmatigheid en onvoorspelbaarheid van die klip vorms maak dit moeilik om 'n algemene drukverlies korrelasie te formuleer. Tipiese lug-klipbed termiese ontwerp konsepte bestaan uit 'n groot vertikale vierkantige of silindriese houder waarin die gepakte bed is. Sodanige sisteem ontwerpe is eenvoudig, maar vatbaar vir die palrat effek en groot drukverliese. Verskeie studies het voorgestelde konsepte om hierdie kwessies te oorkom, maar daar is steeds 'n behoefte aan metodes om die haalbaarheid van die ontwerpe te bewys.

Die doel van hierdie studie is om 'n Diskreet Element Modelle (DEM) en numeriese vloed dinamika gekoppelde benadering te ontwikkel wat 'n lug-klipbed

termiese energie stoorstelsel kan ondersoek. Hierdie studie fokus spesifiek op die gebruik van numeriese vloed dinamika. 'n Aanvullende studie fokus op DEM. Die twee areas van fokus in hierdie studie is die drukverlies en stelsel ontwerp. 'n Diskrete numeriese vloed dinamika simulatie model word gebruik om drukverlies te voorspel oor gepakte beddens met sferiese en onreëlmatige partikels. DEM word gebruik om lukraak gepakte beddens van óf sferiese óf onreëlmatige partikels te skep. Hierdie model is ook gebruik om die hitte-oordrag tussen die vloeistof en partikel oppervlak te bepaal. 'n Poreuse numeriese vloed dinamika model word gebruik om die stelsel ontwerp konsepte voor te stel. Drukverlies en hitte-oordrag data, voorspel deur die diskrete model, word gebruik in die poreuse model om die drukverlies- en hittegedrag van 'n TES-stelsel te beskryf.

Resultate van die diskrete numeriese vloed dinamika model toon dat dit akkuraat die drukverlies oor 'n gepakte bed van sferiese partikels kan voorspel met 'n gemiddelde afwyking van ongeveer 10 % van die resultate wat in die literatuur aangetref word. Die hitte-oordrag tussen die vloeistof en partikel oppervlak is ook akkuraat voorspel, met 'n gemiddelde afwyking van tussen 13.36 % en 21.83 % van die resultate wat in die literatuur aangetref word. Die diskrete numeriese vloed dinamika model vir gepakte beddens met onreëlmatige partikels bied probleme wanneer 'n maas vir die numeriese vloed dinamika, numeriese domein gegenerer word. Die "clump" logika metode is gebruik om klip partikels te verteenwoordig in hierdie studie. Hierdie metode is deur ander studies bewys om akkuraat die klip partikel en die klip gepakte bed-struktuur te modelleer deur die gebruik van DEM. Hierdie tegniek het egter probleme gebied toe die oppervlak maas gegenerer is. As gevolg hiervan is 'n vereenvoudigde "clump" model gebruik om die klip partikels te verteenwoordig. Die vereenvoudigde "clump" model vertoon karakteristieke eienskappe van 'n gepakte bed van klippe in terme van drukverlies en hitte oordrag. Die resultate het egter getoon dat die partikels nie vorm weerstand verteenwoordig nie. Hierdie resultate kan toegeskryf word aan die afwesigheid van gladde oppervlaktes en skerp kante, wat normaalweg op klip partikels gevind word, in die vereenvoudigde "clump" model. Die oneweredige partikels wat in hierdie studie voorgestel word, blyk om nie geskik te wees vir die modellering van die universele karakteristieke eienskappe van 'n gepakte bed van klippe in terme van drukverlies nie. Die poreuse numeriese vloed dinamika model is met eksperimentele metings bevestig om die termiese gedrag van klipbeddens te voorspel. Die toepassing van die poreuse model demonstreer dat dit 'n nuttige ontwerp metode is vir stelsel ontwerp konsepte.

# Acknowledgements

I would like to express my sincere gratitude to the following people and organisations:

Mr Gauché for his guidance that assisted me throughout the course of my study. Who inspired with his immense knowledge, enthusiasm and encouragement.

Mr Allen for sharing his vast knowledge and experimental results. His research was elemental to my study.

Mr Mouzouris who assist with experiments and helped with various aspects concerning my study.

Mr Nel for supplying my study with DEM simulations results of packed beds. Who as a good friend, was always willing to assist and give his best advice.

STERG who supplied the funds for this study through the DST/NRF solar thermal spoke and the Stellenbosch University HOPE Project.

# Dedications

*I would like to thank my family for the opportunity and support I received and all my friends who made my time at Stellenbosch unforgettable. I would like to give special thanks to Leischen Travers whose love and unconditional support aided me in completing my work. Above all I would like to thank God for blessing me with the opportunity to study his natural world and all its mystery and power.*

# Contents

<b>Declaration</b>	<b>i</b>
<b>Abstract</b>	<b>ii</b>
<b>Uittreksel</b>	<b>iv</b>
<b>Acknowledgements</b>	<b>vi</b>
<b>Dedications</b>	<b>vii</b>
<b>Contents</b>	<b>viii</b>
<b>List of Figures</b>	<b>xii</b>
<b>List of Tables</b>	<b>xv</b>
<b>Nomenclature</b>	<b>xvi</b>
<b>1 Introduction</b>	<b>1</b>
1.1 Background . . . . .	1
1.2 SUNSPOT . . . . .	3
1.3 Objective . . . . .	4
1.4 Methodology . . . . .	4
1.5 Motivation . . . . .	4
1.6 Conclusion . . . . .	5
<b>2 Literature review</b>	<b>6</b>
2.1 Rock bed thermal energy storage for CSP . . . . .	6
2.2 Transient thermal numerical models . . . . .	8
2.3 Rock properties . . . . .	8
2.4 Discrete CFD modelling of packed beds . . . . .	9
2.4.1 Numerically generating packed beds . . . . .	11
2.4.2 Turbulence . . . . .	12
2.4.3 Meshing . . . . .	13
2.4.4 Contact treatment . . . . .	14

2.5	Conclusion . . . . .	17
<b>3</b>	<b>Methods</b>	<b>18</b>
3.1	Characteristics of packed beds . . . . .	18
3.1.1	Porous media . . . . .	18
3.1.2	Porosity . . . . .	18
3.1.3	Wall effect on bulk density . . . . .	19
3.1.4	Radial porosity variation . . . . .	19
3.1.5	Axial porosity variation . . . . .	21
3.1.6	Particle characterization . . . . .	21
3.1.7	DEM . . . . .	23
3.1.7.1	Irregular particles . . . . .	24
3.2	Flow and heat transfer through packed beds . . . . .	26
3.2.1	Pressure drop . . . . .	27
3.2.2	Heat transfer . . . . .	31
3.3	CFD . . . . .	35
3.3.1	Solvers . . . . .	37
3.3.2	Porous media condition . . . . .	37
3.4	Conclusion . . . . .	39
<b>4</b>	<b>Numerical model</b>	<b>40</b>
4.1	Discrete CFD model . . . . .	41
4.1.1	Generating a CAD model . . . . .	41
4.1.2	Contact treatment . . . . .	42
4.1.3	Channelling . . . . .	42
4.1.4	Mesh generation . . . . .	43
4.1.5	Turbulence modelling . . . . .	44
4.1.6	Boundaries and material properties . . . . .	45
4.2	Porous CFD model . . . . .	45
4.2.1	CAD model . . . . .	45
4.2.2	Mesh generation . . . . .	45
4.2.3	Turbulence modelling . . . . .	46
4.2.4	Boundaries and material properties . . . . .	46
4.3	Conclusion . . . . .	46
<b>5</b>	<b>Discrete results and validation</b>	<b>47</b>
5.1	Discrete CFD model validation . . . . .	47
5.1.1	Geometry . . . . .	47
5.1.2	Computational domain . . . . .	47
5.1.3	Turbulence model selection . . . . .	48
5.1.4	Wall channelling modification . . . . .	49
5.1.5	Mesh refinement study . . . . .	53
5.2	Spherical particle packed bed results . . . . .	54
5.3	Irregular particles packed bed results . . . . .	56

5.3.1	Results . . . . .	57
5.4	Conclusion . . . . .	59
<b>6</b>	<b>Porous results and validation</b>	<b>60</b>
6.1	Porous CFD model of shale rock bed experiment . . . . .	60
6.1.1	Porous CFD model setup . . . . .	60
6.1.2	Porous CFD model results . . . . .	62
6.2	Porous CFD model of the Sauna . . . . .	64
6.2.1	Experiment . . . . .	64
6.2.2	Computational domain . . . . .	65
6.2.3	Sauna CFD results . . . . .	66
6.3	Conclusion . . . . .	69
<b>7</b>	<b>Application</b>	<b>70</b>
7.1	Cone rock bed thermal energy storage system . . . . .	70
7.2	Results . . . . .	71
7.3	Conclusion . . . . .	74
<b>8</b>	<b>Conclusions</b>	<b>75</b>
8.1	Conclusion from work done . . . . .	75
8.2	Recommendations for future work . . . . .	77
	<b>Appendices</b>	<b>78</b>
<b>A</b>	<b>Irregular packed bed geometry</b>	<b>79</b>
A.1	Non-uniform sized sphere bed . . . . .	79
A.2	PES particle bed . . . . .	80
A.3	Elongated particle bed . . . . .	81
A.4	Pyramid particle bed . . . . .	83
<b>B</b>	<b>Computational fluid dynamics</b>	<b>85</b>
B.1	RANS turbulence models . . . . .	85
B.1.1	$k - \epsilon$ turbulence model . . . . .	86
B.1.2	Spalart-Allmaras model . . . . .	88
B.1.3	$k - \omega$ and SST $k - \omega$ model . . . . .	89
B.2	Pressure-based solvers . . . . .	90
<b>C</b>	<b>Boundary conditions</b>	<b>92</b>
C.1	Discrete CFD model's boundaries . . . . .	92
C.1.1	Boundaries . . . . .	92
C.2	Porous CFD model's boundaries . . . . .	93
C.2.1	Zones and boundaries . . . . .	93
<b>D</b>	<b>Reynolds number definition</b>	<b>94</b>
D.1	Reynolds number . . . . .	94

<i>CONTENTS</i>	xi
<b>E Material properties</b>	<b>96</b>
E.1 Rock properties . . . . .	96
E.2 Air properties . . . . .	96
E.2.1 Ideal gas law . . . . .	96
E.2.2 Viscosity . . . . .	97
E.2.3 Conductivity . . . . .	97
E.2.4 Heat capacity . . . . .	97
<b>F Solar map</b>	<b>98</b>
F.1 DNI solar map of South Africa . . . . .	98
<b>G Contact treatment method</b>	<b>99</b>
G.1 Determining which spheres are in contact . . . . .	99
<b>H Cone rock bed TES</b>	<b>102</b>
H.1 Cone rock bed TES parameters . . . . .	102
H.2 Simple Cone rock bed storage system geometry analysis . . . . .	103
H.3 CFD model setup . . . . .	106
<b>I Sample calculations</b>	<b>108</b>
I.1 Pressure drop . . . . .	108
I.2 Heat transfer . . . . .	109
<b>J Porous media</b>	<b>112</b>
J.1 Pressure source term UDF . . . . .	112
<b>K Sauna test facility</b>	<b>114</b>
K.1 Sauna . . . . .	114
<b>List of References</b>	<b>118</b>

# List of Figures

1.1	SUNSPOT cycle (Kröger, 2012) . . . . .	3
2.1	Effect of the bridge model on the global porosity (Louw <i>et al.</i> , 2012) . .	16
2.2	Local flattening and Interparticle bridge methods . . . . .	16
3.1	Bulk porosity vs. tube-to-particle diameter correlations . . . . .	20
3.2	Radial porosity variation (Mueller, 1991) . . . . .	20
3.3	Axial porosity variation (Auwerda <i>et al.</i> , 2010) . . . . .	21
3.4	Example of particle equivalent diameter . . . . .	22
3.5	Generating a packed bed with DEM (courtesy of R.G. Nel) . . . . .	23
3.6	Rock particle represented by a clump model (courtesy of R.G. Nel) . .	24
3.7	Rock particles with superimposed clump equivalents (Horn, 2012) . .	25
3.8	Equivalent clump particle shapes (Horn, 2012) . . . . .	26
3.9	Modified elongated and pyramid clump particle shapes . . . . .	26
3.10	Packed bed thermocline . . . . .	32
4.1	Numerical method process . . . . .	40
4.2	Geometry generation flow chart . . . . .	41
4.3	Spherical particles wall channelling modification . . . . .	42
4.4	Irregular particles wall channelling modification . . . . .	43
4.5	Fluid cells around contact region (first prism layer = $3 \times \delta_{BL}/10$ ) . . . .	44
4.6	Porous media geometry and boundary . . . . .	45
4.7	Hybrid mesh . . . . .	46
5.1	Sphere bed with and without channelling modification . . . . .	48
5.2	Computational domain with and without channelling modification . .	49
5.3	Wall channelling modification friction factor results . . . . .	51
5.4	Wall channelling modification heat transfer results . . . . .	51
5.5	Outlet cross sectional temperature profile . . . . .	52
	(a) $Re_p = 100$ . . . . .	52
	(b) $Re_p = 1000$ . . . . .	52
	(c) $Re_p = 4000$ . . . . .	52
5.6	Temperature contours . . . . .	53
	(a) $Re_p = 100$ . . . . .	53
	(b) $Re_p = 1000$ . . . . .	53

(c) $Re_p = 4000$ . . . . .	53
5.7 Spherical particle bed pressure drop results . . . . .	55
5.8 Spherical particle bed heat transfer results . . . . .	56
5.9 Irregular particle bed pressure drop results . . . . .	57
5.10 Irregular particle bed heat transfer results . . . . .	58
6.1 Experimental setup (Allen, 2010) . . . . .	61
(a) Thermocouple positions . . . . .	61
6.2 Porous CFD model of the shale bed . . . . .	61
6.3 Shale bed model mesh . . . . .	62
(a) Coarse . . . . .	62
(b) Medium . . . . .	62
(c) Fine . . . . .	62
6.4 CFD porous model vs. experimental results . . . . .	62
(a) $G = 0.297 \text{ kg/m}^2\text{s}$ . . . . .	62
(b) $G = 0.467 \text{ kg/m}^2\text{s}$ . . . . .	62
(c) $G = 0.842 \text{ kg/m}^2\text{s}$ . . . . .	62
6.5 Porous CFD model mesh sensitivity ( $G = 0.467 \text{ kg/m}^2\text{s}$ ) . . . . .	63
6.6 Porous CFD model $c_s$ sensitivity ( $G = 0.467 \text{ kg/m}^2\text{s}$ ) . . . . .	63
6.7 Porous CFD model time step sensitivity ( $G = 0.467 \text{ kg/m}^2\text{s}$ ) . . . . .	64
6.8 Sauna computational model . . . . .	65
(a) CAD model . . . . .	65
(b) Computational domain . . . . .	65
6.9 Sauna charging results . . . . .	67
6.10 Sauna discharging results . . . . .	67
6.11 Sauna charging pressure drop results . . . . .	68
6.12 Sauna sensitivity to particles size . . . . .	68
7.1 Cone rock bed storage . . . . .	70
7.2 Charge/Discharge temperature contours . . . . .	72
(a) Charge $t = 8 \text{ h}$ . . . . .	72
(b) Discharge $t = 30 \text{ h}$ . . . . .	72
7.3 Discharging temperature vs. time . . . . .	73
7.4 Pressure drop vs. Time . . . . .	73
(a) Charge . . . . .	73
(b) Discharge . . . . .	73
7.5 Pressure drop . . . . .	74
(a) Cross section plot . . . . .	74
(b) pressure contours . . . . .	74
A.1 Non-uniform sized sphere bed with and without channelling modification . . . . .	79
A.2 PES bed with and without channelling modification . . . . .	81
A.3 Elongated particle bed with and without channelling modification . . . . .	82

## LIST OF FIGURES

xiv

A.4	Pyramid particle bed with and without channelling modification . . . . .	83
B.1	Pressure-based solver (Fluent, 2011 <i>a</i> ) . . . . .	91
C.1	Flow domain boundaries . . . . .	92
F.1	DNI solar map of South Africa (GeoSUN AFRICA, 2012) . . . . .	98
G.1	DEM data file format example . . . . .	99
G.2	Contact treatment file format example . . . . .	100
G.3	VBA interface . . . . .	101
H.1	Pyramid geometry analysis (Autodesk Inc., 2012) . . . . .	104
H.2	Pyramid flow path length . . . . .	105
	(a) $h/Y = 0.50$ . . . . .	105
	(b) $h/Y = 0.75$ . . . . .	105
	(c) $h/Y = 0.90$ . . . . .	105
	(d) $h/Y = 1.00$ . . . . .	105
H.3	Pyramid geometry active region Autodesk Inc. (2012) . . . . .	105
H.4	Pyramid TES efficiency . . . . .	106
H.5	Cone rock bed mesh . . . . .	107
	(a) Mesh . . . . .	107
	(b) Mesh cross section . . . . .	107
K.1	Illustration of the Sauna . . . . .	114
K.2	Sauna insulation . . . . .	115
	(a) Construction material (Cengel, 2006) . . . . .	115
	(b) Insulation material (Lapinus; Thermal Ceramics) . . . . .	115
K.3	Sauna diesel burner and blower view . . . . .	116
K.4	Sauna diesel tank and measuring and control equipment view . . . . .	116
K.5	Sauna bell mouth . . . . .	117
K.6	Sauna orifice plate . . . . .	117

# List of Tables

2.1	Recommended size ranges for cap and bridge methods (Dixon <i>et al.</i> , 2013) . . . . .	16
3.1	Horn (2012) particle size and particle volume distribution . . . . .	25
4.1	Size range for bridge method . . . . .	42
4.2	Surface and volume mesh parameters . . . . .	43
5.1	Sphere bed porosity . . . . .	48
5.2	Turbulence model comparison . . . . .	49
5.3	Turbulence model comparison . . . . .	50
5.4	Wall channelling modification effect . . . . .	50
5.5	Wall channelling modification Nusselt number effect . . . . .	51
5.6	Mesh refinement . . . . .	54
5.7	Packed beds . . . . .	56
6.1	Shale rock bed experiment information (Allen, 2010) . . . . .	60
6.2	Sauna experimental information . . . . .	65
A.1	Non-uniform sized sphere bed parameters . . . . .	80
A.2	Non-uniform sized sphere bed mesh . . . . .	80
A.3	PES bed parameters . . . . .	81
A.4	PES bed mesh . . . . .	81
A.5	Elongated bed parameters . . . . .	82
A.6	Elongated mesh . . . . .	82
A.7	Pyramid bed parameters . . . . .	83
A.8	Pyramid mesh . . . . .	84
E.1	South African rock properties . . . . .	96
E.2	Rock properties experimentally measured by Zanganeh <i>et al.</i> (2012) . . . . .	96
H.1	Pyramid TES dimensions . . . . .	103
H.2	Ankerlig gas turbine exhaust data (Eskom, 2013) . . . . .	103
I.1	Pressure drop calculation input data . . . . .	108
I.2	Heat transfer calculation input data . . . . .	109

# Nomenclature

## Constants

$$g = 9.81 \text{ m/s}^2$$

## Variables

$A$	Area
$A_{cs}$	Cross-sectional area of the bed
$A_p$	Particle surface area
$a$	Cone TES flow path length
$a_{fs}$	Specific surface area of the bed
$C_2$	Inertial resistance coefficient
$c_p$	Specific heat capacity at constant pressure
$c_s$	Solid heat capacity
$D$	Bed diameter
$d_b$	Inter-particle bridge diameter
$d_p$	Particle diameter
$d_{p_{sv}}$	Equivalent particle diameter based on spherical specific surface area
$d_{p_v}$	Equivalent particle diameter based on spherical volume
$f$	Friction factor
$H$	Bed height
$H_{sph}$	Distance between two particle's surfaces
$h$	Surface heat transfer or Cone TES inlet solid shaft length
$h_v$	Volumetric heat transfer coefficient
$G$	Mass flow flux
$k$	Permeability or Turbulent kinetic energy
$k_f$	Fluid thermal conductivity
$k_s$	Solid thermal conductivity
$k_{eff}$	Effective thermal conductivity
$L$	Bed length
$Nu$	Nusselt number

$Nu_v$	Volumetric Nusselt number
$P$	Pressure
$Pr$	Prandtl number
$R$	Drag force per unit area or Gas constant for air
$Re_{Erg}$	Ergun Reynolds number
$Re_p$	Particle Reynolds number
$Re_1$	Carman Reynolds number
$Re_2$	Allen Reynolds number
$r$	Radial distance from container wall
$S$	Source term
$S_v$	Specific surface area
$T$	Temperature
$T_{in}$	Inlet temperature
$T_b$	Bulk mean fluid temperature
$T_L$	Particles surface temperature
$T_{out}$	Outlet temperature
$t$	Time
$t_{ins}$	Insulation thickness
$U_0$	Superficial velocity
$u$	Interstitial velocity
$u'$	Fluctuating velocity component
$\bar{u}$	Mean velocity component
$V$	Fluid volume
$V_p$	Particle Volume
$V_S$	Solid volume
$V_T$	Total bed volume
$V_V$	Void volume
$\dot{V}$	Fluid volume flow rate
$Y$	Cone TES total height
$y^+$	Dimensionless wall distance
$\alpha$	Viscous resistance coefficient
$\alpha_{ax}$	Axial diffusivity
$\gamma$	Arbitrary scalar
$\delta_{BL}$	Theoretical boundary layer thickness
$\epsilon$	Viscous dissipation
$\epsilon$	Porosity

$\varepsilon_r$	Radial porosity
$\eta_{Vol}$	Cone TES volume efficiency
$\theta$	Angle of repose
$\kappa$	von Karman's constant
$\mu$	Dynamic viscosity
$\mu_t$	Dynamic turbulent viscosity
$\nu$	Kinematic viscosity
$\nu_t$	Turbulent kinematic viscosity
$\rho$	Density
$\psi$	Sphericity
$\Psi$	Cone TES flow path angle
$\omega$	Turbulent frequency

**Subscripts**

f	Fluid
s	Solid

**Acronyms**

BCC	Body Centred Cubic
CFD	Computational Fluid Dynamics
CSP	Concentrating Solar Power
DEM	Discrete Element Method
DNI	Direct Normal Irradiance
EVM	Eddy Viscosity Model
FCC	Face Centred Cubic
LES	Large Eddy Simulations
PV	Photo Voltaic
RANS	Reynolds-Averaging Navier-Stokes
RSM	Reynolds Stress Model
SC	Simple Cubic
SUNSPOT	<u>S</u> tellenbosch <u>U</u> niversity <u>S</u> olar <u>P</u> ower <u>T</u> hermodynamic (cycle)
TES	Thermal Energy Storage

# 1. Introduction

Solar energy is considered one of the most prospective sources of energy to meet energy demands and increasing fuel prices and prevent the increase of Greenhouse gases. (Banks and Schäffler, 2006).

There are two types of technologies which can convert solar radiation to electrical power, the one is photo voltaic (PV) and the other one is solar thermal power plants. PV cells consist of two semi-conductor layers which release electrons when exposed to sunlight. Solar thermal power technologies, such as concentrating solar power (CSP), capture the sun's thermal energy and convert it to electrical power by means of a heat engine coupled to a generator. A key feature of CSP technology is its ability to store energy relatively efficiently and cheaply. An air-rock bed thermal energy storage (TES) system promises to be an effective and reasonably inexpensive storage system for CSP plants. The intermittent nature of solar energy requires an energy storage system to effectively utilize this source of energy.

The study aims to develop a porous computational fluid dynamics (CFD) model, using ANSYS FLUENT (Fluent, 2011*a*), to model an air-rock bed TES system for CSP plant. A coupled discrete element method (DEM) and CFD approach is investigated to determine the flow and heat transfer characteristics through a packed bed for the porous CFD model.

This chapter will discuss background information concerning CSP and TES systems, the SUNSPOT cycle, the study objectives, methodology and motivation.

## 1.1 Background

South Africa has some of the highest direct normal irradiance (DNI) levels in the world. The parts of the country with the most solar radiation lie in the central and western regions (see solar map in Figure F.1 in Appendix F). The Upington region in particular has very high long-term annual average DNI values measured to be 2816 kWh/m<sup>2</sup>. This measurement is higher than those taken in Spain and the USA, countries where multiple CSP plants have already been constructed and DNI values at these plants are between 2000-2100 kWh/m<sup>2</sup> and approximately 2700 kWh/m<sup>2</sup> per annum respectively (Muirhead and Eaton, 2013).

There exist four main CSP collector technologies: parabolic dish, central receiver, parabolic trough and linear Fresnel. The most proven of these technolo-

gies is the parabolic trough with the most commercial plants in operation. Central receiver tower CSP plants are starting to catch up with more commercial plants that have come into operation in recent years. The fundamental components of all CSP technologies are the power block, solar field and TES system.

The two main factors that negatively affect the growth of CSP plants are the high initial capital cost and the large area required for these plants. The solar field and the TES systems are two of the most expensive components of a CSP plant. For the case of a 50 MW parabolic trough CSP plant with 7 hours of storage, approximately 30% and 9% of the initial capital cost is for the solar field and TES system respectively (IEA, 2010). Therefore, reducing the size of the solar field and developing a low-cost TES system is important for the future development of CSP.

The function of a TES system is to store the excess thermal energy captured during the day and release it during the night or periods of bad weather. This function improves the dispatchability and capacity factor of CSP plants and also enables it to provide base load power, which increases the grid penetration of renewable power. The recently built Gemasolar CSP plant in Spain demonstrates what can be achieved with a large TES system. It is the first commercial-scale CSP plant to use a central receiver with molten salt as storage material, with a full load storage capacity of up to 15 hours. This enables the plant to achieve an annual capacity factor of approximately 74% (NREL, 2012*b*). Other CSP plants in operation with 7-9 hours of storage have capacity factors in the range of 36-39%, and those without storage ranges between 21-27%. Most commercial CSP plants, however, are currently being built with 7-9 hours of storage capacity (NREL, 2012*b*). A TES system allows solar energy to be dispatched when needed, to reduce the net peak demands that continually move into the evening thereby displacing the need for more expensive gas-fired generation during these periods and offsetting the need to build new gas-fired power stations (NREL, 2012*a*).

Currently the most common commercially used TES system for CSP is molten salt storage, usually configured in a 2-tank indirect storage system. This type of system uses expensive storage material and heat exchangers, and there is a relatively small temperature difference between the hot and cold tank. To reduce the cost and environmental impact of storage systems, an air-rock bed storage system could be a possible solution because of its inherent properties. The storage material for an air-rock bed is non-flammable, non-toxic and inexpensive. The large surface area of a packed bed also improves heat transfer between air and rock.

The University of Stellenbosch is investigating a concept that is purported to make CSP more economically feasible. The Stellenbosch University Solar Power Ther-modynamic (SUNSPOT) cycle concept proposed, by Kröger (2012), is a combined cycle plant with a low cost TES system. The SUNSPOT cycle is discussed in section 1.2.

## 1.2 SUNSPOT

The SUNSPOT cycle (Figure 1.1) consists of a primary Brayton (gas turbine) and a secondary Rankine (steam turbine) cycle (Kröger, 2012). A combined cycle power plant can achieve a higher efficiency than a single cycle power plant (Kehlhofer *et al.*, 1999).

Ambient air is drawn in and compressed, which then flows to the central receiver tower where it is heated to more than  $800\text{ }^{\circ}\text{C}$  by solar energy. The solar energy is concentrated on the receiver by means of a heliostat field. A combustion chamber is used as an auxiliary heat source that adds additional energy to prevent temperature fluctuation due to weather effects. It can also serve to increase the gas turbine air inlet temperature to above a  $1000\text{ }^{\circ}\text{C}$ , in order to reach higher cycle efficiency (Allen, 2010). The heated air then flows to the gas turbine where it is expanded and leaves the turbine at around  $500\text{ }^{\circ}\text{C}$ . The exhaust gases from the gas turbine are used to transfer thermal energy to the TES system. The stored heat is used to generate steam via a boiler for the steam cycle during the night or bad weather periods. The exhaust gases can also be directly used to generate steam for the steam cycle during the day. Dry cooling or hybrid cooling is used because solar power plants are usually situated in water scarce areas. The advantage of using stored heat during the night for the steam cycle is that the ambient temperature is lower, which means that dry cooling will be more effective (Allen, 2010).

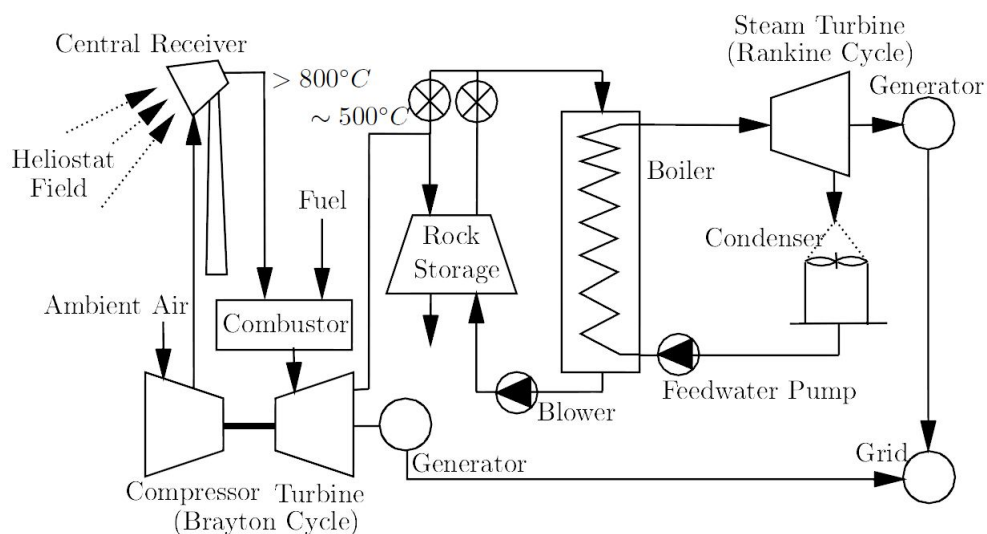


Figure 1.1: SUNSPOT cycle (Kröger, 2012)

### 1.3 Objective

To help develop air-rock bed TES systems further, research is required in the following areas namely thermal-mechanical behaviour of rocks, rock bed pressure drop and effective and practical system designs. The pumping power required for an air-rock bed is directly related to the pressure drop over the bed. Therefore, the accurate prediction of it is crucial for system design.

The objective of this study is to develop a porous CFD model for system modelling of air-rock bed TES system design concepts. Furthermore the study also aims to develop a discrete CFD model using a DEM-CFD coupled approach to provide the flow and heat transfer data for the air-rock bed porous CFD model.

The numerical methods under investigation is the DEM and CFD. The numerical method which this study focuses on is CFD and a study completed by Nel (2013) focuses on the use of DEM for modelling packed beds of rocks.

### 1.4 Methodology

A discrete CFD model is used to determine the pressure drop and heat transfer results of a packed bed. A porous CFD model is used to model air-rock bed system design concepts.

Two types of beds are investigated with the discrete CFD model: spherical packed beds and irregular packed beds. A spherical bed refers to a bed containing only uniformly sized spheres. An irregular bed refers to a bed containing either non-uniform sized spheres or any other type of particle shape other than a sphere. The spherical packed bed is used to establish a method of modelling flow and heat transfer through a packed bed using a discrete CFD model. The established method for the spherical packed beds, in terms of turbulence model, mesh strategy and contact treatment, are then assumed also valid for irregular packed beds. The irregular packed beds are used to model a rock bed. Pressure drop and heat transfer correlations from literature are used in the porous CFD model to predict the pressure drop and thermal behaviour of an air-rock bed TES system. The results from the discrete CFD models can also be used.

In order to validate the discrete and porous CFD models experimental measurement and results from literature are used.

### 1.5 Motivation

Electricity in South Africa is supplied by Eskom, who is currently responsible for generating roughly 95% of the country's electricity. The growing demand for electricity in the country has been at approximately 3% per annum. This growth places strain on the existing power generation capacity and must be increased to meet future demands. The need for a greater power generation capacity and a growing awareness of environmental impact and climate change has called upon

a more sustainable solution to increase the countries generating capacity (Eskom, 2007). The present energy demand is about 250 TWh per year and it is projected that the energy demand will increase to 290 TWh in the year 2018 (Banks and Schäffler, 2006).

Considering the excellent solar resources in South Africa, CSP is an attractive technology to help the country meet their energy demand. An effective and more affordable air-rock bed storage system can aid the development of CSP. Previous studies have shown the feasibility of air-rock bed TES systems, but much more research is required before there can be commercial use of this system.

Nearly all pressure drop and heat transfer correlations for packed beds has been obtained by experimental methods, which are time consuming and expensive. The increase of computational power in recent years has enabled discrete CFD modelling of flow and heat transfer through packed beds containing over a thousand particles. Previous studies have modelled flow and/or heat transfer through packed beds using CFD (Bai *et al.*, 2009; Calis *et al.*, 2001; Eppinger *et al.*, 2010; Freund *et al.*, 2003; Logtenberg and Dixon, 1998*a*). These studies show that, although difficult, CFD can model flow through a packed bed.

Most numerical models found in literature to model an air-rock bed storage system are one dimensional plug flow models. Recently a need has arisen to model more complex system configurations that include features such as internal channels, which could possibly improve heat transfer and lower the pressure drop. These complex features would be difficult to model with the one dimensional models. CFD has long been used to model flow and heat transfer through complex three dimensional computational domains and can be a possible design tool to investigate and develop different TES systems.

## 1.6 Conclusion

CSP technology shows the potential to make the world less dependent on conventional fossil fuel energy sources. However, there still remains research to be done to make the technologies economically competitive. The excellent local solar resources, together with the proposed SUNSPOT cycle, could potentially make CSP more economically feasible in South Africa.

A key feature of the SUNSPOT cycle is the air-rock bed TES system, addressed in this study. A need has been identified to numerically model an air-rock bed TES system with the focus on development and optimization. Numerical methods such as DEM and CFD possesses the ability to model air-rock beds accurately. This study investigates CFD as a numerical analysis tool for air-rock bed TES systems.

The following chapters discuss literature regarding the topic of this study, methods used to setup the models, results and validation and finally the conclusion is given.

## 2. Literature review

### 2.1 Rock bed thermal energy storage for CSP

The topic of rock bed thermal storage systems has interested researchers for decades, and many studies have explored the feasibility, performance and behaviour of rock bed thermal storage systems. In this section a brief discussion of previous work concerning packed bed storage is given.

A study conducted by Fricker (1991) mentions that rock shows potential for being a low cost, high temperature storage material, but notes that more research is needed into the thermal-mechanical behaviour of rocks and pressure drop through a packed bed of rocks. Allen (2010) shows the performance characteristic of a packed bed thermal energy storage system for CSP plants, specifically focusing on using rock or slag as a storage medium with air as the heat transfer medium. A thermal cycling test done at around 773 K, showed that dolerite and granite are potentially suitable for CSP application. Fricker (1991) also suggests granite as a suitable storage material. A study later done by Allen *et al.* (2012) shows that there are large deposits of gneiss, granite and dolerite in the region with the best solar resources in South Africa. They recommend that more thermal cycling tests at temperatures up to 773 K be done on these rocks to determine if they can withstand several thousand charge/discharge cycles.

Experimental measurements taken by Allen *et al.* (2012) show the shortcomings of the well-known Ergun correlation for predicting the pressure drop of a packed bed. The study indicates that the pressure drop is dependent on the particle shape, surface roughness and packing arrangement. It is recommended that packed beds containing irregular particles should have correlations specific to the type of material used and packing method, rather than a general correlation. Earlier work done by Singh *et al.* (2006) also shows through experiments that the particle shape affects the pressure drop. Furthermore the work develops correlations for the pressure drop, both being functions of the Reynolds number, sphericity and porosity. Experimental work done by Chandra and Willits (1981) also indicated that Reynolds number, particle size and porosity affect the pressure drop.

Löf and Hawley (1948) present the earliest work found by this study that determines the heat transfer coefficient through a packed bed of rocks. The authors demonstrate that the heat transfer is dependent on the mass flux and the parti-

cle size, and the inlet temperature has no apparent effect. Chandra and Willits (1981) later demonstrate that the inlet temperature has no influence on the heat transfer coefficient. The study found it is dependent on the mass flux and particle size. The work of Singh *et al.* (2006), however, shows that the heat transfer coefficient is dependent on the particle shape, porosity and Reynolds number. Experimental work by Malling and Thodos (1967) done on packed beds of spheres demonstrate that heat transfer is dependent on the Reynolds number and porosity. Wakoa *et al.* (1979) obtain published heat transfer data from several different authors for steady and unsteady measurements and correct them for axial fluid thermal dispersion coefficients. A correlation of the corrected heat transfer data is presented which includes fluid axial thermal dispersion. The correlation is dependent of the Reynolds number and Prandtl number.

Bed parameters that have been shown to influence the bed performance characteristics such as the thermal stratification, overall efficiency and capacity factor are the particle size, bed dimensions, flow rate and storage material.

The size of the particles have a profound effect on the performance of the TES system. Smaller particles have shown to yield the highest second law availability and most efficient use of the storage volume, but results in a higher pressure drop over the system (Sanderson and Cunningham, 1995*b*). Sanderson and Cunningham (1995*a,b*) recommends a particle size larger than 13 mm to keep the pressure drop to a minimum. Hänchen *et al.* (2010) mention that even though the pumping power increases with decreasing particle size, the highest overall efficiency is still obtained for the smallest particle sizes because the improved thermal stratification ensures the energy is extracted more effectively. Singh *et al.* (2008) simulate the performance of a packed bed TES system for large size storage materials of five different shapes. The study demonstrates that the shape of the particle also influences temperature stratification and the energy stored.

Hänchen *et al.* (2010) further shows that the most important storage material propriety is the heat capacity and the conductivity of the material only has a minor effect. A lower heat capacity value is shown to improve the capacity factor of the bed. Increasing the bed length is shown to increase the overall efficiency but reduce the capacity factor of the bed. Lower flow rate is shown to increase the overall efficiency but decrease the capacity factor (Hänchen *et al.*, 2010). Allen (2010) recommends using a flow rate below  $0.2 \text{ kg/m}^2\text{s}$ . Zavattoni *et al.* (2011) reproduce an experimental rock bed TES system using 3-D CFD simulations to determine the effect of the axial porosity variation. Comparing the CFD simulation with experimental results show that the axial porosity variation has an effect on the time-temperature profile and pressure drop. The quadratic axial porosity distribution compares the best with the experimental results.

## 2.2 Transient thermal numerical models

Numerical models have played a key role in enabling researchers to determine the performance characteristic and behaviour of packed bed storage. Two types of transient thermal numerical models are found in literature: one dimensional single-phase models and one dimensional two-phase models.

Most of the work reviewed in this study uses a two-phase model to describe the motion of the thermal wave through a packed bed TES system. Two-phase models assume non-thermal equilibrium and heat transfer between the solid and fluid phases and the motion of the thermal wave is described by the effective conductivity and heat transfer coefficient. Schumann (1929) discusses the first analytical two-phase thermal model for a packed bed. The Schumann model makes the following assumptions: no axial conduction, single uniform particle temperatures ( $Bi \ll 1$ ), temperature independent solid and fluid properties, plug flow, no temperature gradient in the radial direction and no losses to the environment.

Zanganeh *et al.* (2012) develop a numerical model which includes axial conduction, radiation between particles, temperature dependent solid and fluid material properties and heat losses through the walls to the environment. The results show that the effect of axial conduction is small, and the radiation between particles has a relatively larger effect, especially at high temperature, though not significantly. The following studies also did work concerning one dimensional two-phase models: Al-nimr *et al.* (1996); Coutier and Farber (1982); Heller and Gauché (2012); Mawire and McPherson (2007); Mawire *et al.* (2009); Sagara and Nakahara (1991); Sanderson and Cunningham (1995*b*); Singh *et al.* (2008).

Single-phase models assume thermal equilibrium, and no heat is transferred between the fluid and solid phases. The motion of the thermal wave is described by the packed beds effective thermal conductivity. Equivalent single-phase models, which combine the effect of solid to fluid convective heat transfer and axial conduction, have been developed by authors such as Vortmeyer and Schaefer (1974) and Riaz (1978).

## 2.3 Rock properties

Allen *et al.* (2012) determine the suitability and availability of South African rocks for use in a TES system. The investigations conclude that dolerite (also known as diabase), granite and gneiss show potential for use in a TES system, all of which are found in the Northern Cape where the highest solar resources in South Africa are found.

Jones (2003) characterizes the thermal properties of different types of rocks found in the Witwatersrand mining region of South Africa. Allen (2010) experimentally determines the thermal properties of shale (from southern Namibia), granite (found near Calvinia, Northern Cape, South Africa) and dolerite (found

near Kenhart, Northern Cape, South Africa). The thermal properties from the studies mentioned are given in Table E.1 (Appendix E). Jones (2003) notes that the heat capacity is fairly invariant for different types of rock; however, the same cannot be said for the density and thermal conductivity as seen in the table.

Zanganeh *et al.* (2012) experimentally measures the thermal properties of five different rocks from the Rafzerfeld area in Zurich, Switzerland. The thermal conductivity of each rock is determined at four different temperatures and demonstrates the temperature dependence of the property. Table E.2 (Appendix E) shows the measured results. The results show that the thermal conductivity decreases with increasing temperature, in all cases except for Gabbro, which had the lowest thermal conductivity of the rocks tested and stayed fairly constant. Dolerite may pass into Gabbro with increased grain size (Britannica, 2013).

## 2.4 Discrete CFD modelling of packed beds

There have been several studies that investigate the use of a CFD or a combined DEM-CFD approach to numerically solve the flow and heat transfer through a packed bed. These studies are mostly for the chemical and process industry for fixed bed reactors. The majority of the literature reviewed considers spherical particles, while only a few consider other particle shapes.

Nijemeisland and Dixon (2001) modelled convective heat transfer in a gas-solid fixed bed using CFD. The CFD simulation was done for a bed consisting of 44 spheres in a specifically arranged packing in a tube with an aspect ratio ( $D/d_p$ ) of 2, for particle Reynolds number ( $Re_p$ ) up to 1922. The CFD model builds on experience gained from preliminary studies done by Logtenberg and Dixon (1998*a,b*) and Logtenberg *et al.* (1999). These studies conclude that CFD is a promising tool to evaluate heat transfer behaviour in a fixed bed reactor. Validation of the results is made with measured temperature profiles in an experimental setup with the same geometry. Excellent agreement is obtained between experimental and simulation results after several correction factors. The correction factors were necessary because of non-ideal experimental measurements and phenomenon that were not included in the CFD model.

Calis *et al.* (2001) assess whether commercial CFD software can be applied to accurately predict single-phase pressure drop characteristics through composite structured packed beds and whether it can be used to derive simple algebraic pressure drop correlations. The simulated packed beds were structured packed beds with aspect ratios between 1 and 2. The study validates that commercial CFD software can adequately predict the pressure drop characteristics of a packed bed reactor. The results show good agreement with experimental results with a deviation of about 10%. Romkes *et al.* (2003) follow a similar approach to determine if CFD can be used to accurately predict the rate of mass and heat transfer from catalyst particle-to-fluid in a composite structured packing. The authors develop simple heat transfer correlations for this type of pack-

ing. The same geometries used in Calis *et al.* (2001) are again used in the Romkes *et al.* (2003) study. The results show that commercial CFD software can be used to sufficiently predict the particle-to-fluid heat transfer of a single sphere. The predicted heat/mass transfer for the packed beds shows an average error of 15%.

Guardo *et al.* (2004) simulate the flow and heat transfer through a non-regular packed bed containing 44 spheres with CFD at  $Re_p$  between 84 and 912. The study reports that both laminar and turbulent solutions agree well with the Ergun equation. This was attributed to the similar velocity fields obtained by both laminar and turbulent models and because, fundamentally, the pressure drop is related to the velocity field and not affected by mixing parameters. On the other hand, the study concludes that the wall Nusselt number is greatly affected by the mixing parameters and near-wall treatment. The laminar solution over predicts in the turbulent regime, and the turbulent solution under predicts in the laminar transitional regime. The same geometry is again used in Guardo *et al.* (2006) to study convective heat transfer at low and high pressures. This study simulates flow through the packed bed at  $Re_p$  approximately between 0.1 and 1000. The results shows good agreement with heat transfer correlations for a randomly packed bed of sphere found in literature. The study notices that for the laminar and transition flow regimes, the predicted Nusselt number is not so sensitive to the mesh density around the particle. However, in the turbulent flow regime the mesh density plays a remarkable role, and it is recommended that the mesh size around the particle must be properly defined.

Bai *et al.* (2009) use a DEM-CFD coupled approach to model a reactor bed with aspect ratios smaller than 4 containing cylinders or spheres. The study concludes that the predicted CFD results for the cylinders and spheres agree well with experimental measurement. The authors comment that the study shows the potential of a DEM-CFD approach as an optimization tool for a packed bed reactor design. Possibilities to further extend the DEM-CFD approach to model more complex catalyst particle shapes such as ring or penta-ring are also presented. Yang *et al.* (2010) numerically study the flow and heat transfer through structured packed beds (SC, BCC and FCC) with spherical or ellipsoidal particles. The study shows that the Ergun (1952) and Wakao *et al.* (1979) correlations for pressure drop and heat transfer of randomly packed beds, respectively, over predicts the friction factor and Nusselt number for structured packing. It also argues that the particle shape effects both the flow and heat transfer through the structure packing.

The following are also studies done regarding CFD and packed beds: Atmakidis and Kenig (2009); Baker and Tabor (2010); Delele *et al.* (2008); Eppinger *et al.* (2010); Ookawara *et al.* (2007).

From the previous studies, it was determined that the three most important factors to consider when modelling a packed bed in CFD, are the geometry (generating a packed bed and contact treatment), turbulence modelling and the mesh. The following sections discuss these factors in more detail.

### 2.4.1 Numerically generating packed beds

Two main approaches are often used in literature. One is to use a strict algorithm that simulates the particle flow and interactions according to physical laws such as DEM. The other approach uses synthetic techniques, such as a rain model that drops a particle randomly in to a vessel until it makes contact with another particle; after which the packing fraction is increased by either a Monte-Carlo shaking routine or a method that extracts particles randomly from a regularly packed bed (Auwerda *et al.*, 2010).

Ookawara *et al.* (2007) generate a realistic randomly packed bed of spherical particles using DEM. The aspect ratios of the beds ranged between 4 and 8. The study shows that the porosity of the numerically generated bed compares well with results found in literature. Eppinger *et al.* (2010) also use DEM to generate randomly packed beds of spherical particles. The created beds contain between 80 and 750 particles with aspect ratio between 3 and 10. The study demonstrated that the local and global porosity agrees well with known correlations found in literature. Furthermore, Bai *et al.* (2009) use a DEM-CFD coupled approach to model a reactor bed with aspect ratios smaller than 4 containing cylinders or spheres. The commercial DEM software, PFC<sup>3D</sup>, is used to generate the packed beds. Clump logic is used to create the packed bed containing cylindrical particles. Each of the cylindrical particles contained 1000 spherical particles to approximate the shape of a cylinder.

Atmakidis and Kenig (2009) study the influence of confining on the pressure drop in packed beds with moderate aspect ratios. Structured and random packed beds are tested here. The aspect ratios ranged from 1 to 5.5 and 2 to 7 for the structured and random packed beds, respectively. The random bed was generated by employing a ballistic decomposition method. This method drops a large number of particles in a tube in order to place one particle. The particles with the lowest position became part of the packed bed. The global porosities of the bed were then compared against known correlations in literature and is found to be higher. The authors attributed this to the fact that the particles were shrunk to eliminate contact points. Other authors to use similar methods are: Baker and Tabor (2010); Freund *et al.* (2003); Magnico (2003).

Auwerda *et al.* (2010) compare DEM, Monte-Carlo rejection method and expanding system method to experimental results. The objective of this study is to validate the ability of the three numerical methods to generate realistic pebble beds with a similar global porosity and radial porosity profile as the experimental bed. The experimental bed consisted of 5457 acrylic pebbles and had an aspect ratio of 18. Gamma-ray scanning is used to measure the global porosity and radial porosity profile of the bed. The study shows that both DEM and the expanding systems method agree well with experimental results. However, the Monte-Carlo rejection method does not agree well with the experimental results, giving higher global porosities, and it cannot accurately reproduce the radial porosity oscillation observed in the experimental bed.

## 2.4.2 Turbulence

Eisfeld and Schnitzlein (2001) defines the flow regimes within a packed bed with the particle Reynolds Number ( $Re_p$ ). The laminar, transitional and turbulent flow regimes occur in the ranges  $Re_p < 10$ ,  $10 \leq Re_p \leq 300$  and  $Re_p > 300$ , respectively.

A time dependent solution of the Navier-Stokes equation for a high Reynolds number turbulent flow in complex geometries, such as packed beds, is currently beyond our computational capabilities. To avoid directly simulating the small scale eddies, two methods have been developed that transform the Navier-Stokes equation. The one method is Reynolds-Averaging Navier-Stokes (RANS) and the other is large eddy simulations (LES). Both of these methods add additional terms that need to be solved (Dixon *et al.*, 2006). LES requires more computational power and has not been used extensively in CFD simulation of packed beds. Coussirat *et al.* (2007) mention that currently it is not computationally affordable to use LES. Dixon *et al.* (2011) also mention that the small time-steps and high cell count required makes it too expensive. The RANS turbulence models, which have been used the most in previous packed bed CFD studies, are the  $k-\epsilon$  (standard, re-normalised group and realizable),  $k-\omega$  and Spalart-Allmaras (S-A) models.

Gunjal *et al.* (2005) used the standard  $k-\epsilon$  turbulence model to account for the turbulent stresses. Transition flow regime is modelled as turbulent flow because of the uncertainties in simulating transitional flow regimes in a complex geometry. Nijemeisland and Dixon (2004) use the re-normalised group (RNG)  $k-\epsilon$  turbulence model to model the turbulence, as the RNG  $k-\epsilon$  model is more responsive to strain and streamline curvature which is expected in packed beds.

Guardo *et al.* (2005) determine the most accurate RANS turbulence model for wall-to-fluid heat transfer in a packed bed. The  $k-\epsilon$ ,  $k-\omega$  and S-A turbulence models all predict the pressure drop accurately, according to the Ergun equation. However, the study finds that the S-A turbulence model predicts the pressure drop and heat transfer better than the other RANS models investigated. This is believed to be because the model uses a coupling between the wall functions and damping functions for near-wall treatment, moreover it does not include additional diffusion or dissipation terms, and it does not present the stagnation point anomaly.

Lee *et al.* (2007) investigate turbulence induced heat transfer in the packed bed of spheres of a core reactor using LES and RANS. The  $k-\omega$  model from the RANS turbulence models and the LES were selected to model the turbulence. Results indicate that the LES predicts a higher pressure drop, a more random flow field, a higher vortices magnitude and higher temperatures at local hot spots on the pebble surface than the  $k-\omega$  RANS turbulence model.

Coussirat *et al.* (2007) study the performance of the stress-transport models in predicting the particle to fluid heat transfer. The eddy viscosity models (EVM) are compared to the Reynolds stress model (RSM). Here, the EVM turbulence models results are comparable to the RSM turbulence model, and the

added computational cost of the RSM models is not justified.

Dixon *et al.* (2011) use a single-sphere test case to validate meshes for CFD simulations of fixed bed reactors. The study finds that the shear-stress transport (SST)  $k - \omega$  model accurately predicts the  $Nu$  as long as the mesh at the particle surface is fine enough and covers about 60% of the boundary layer.

### 2.4.3 Meshing

The construction of the mesh is an important part in CFD modelling. The accuracy is strongly affected by the mesh and it must be selected with enough detail to describe the flow accurately, but coarse enough to complete the simulation in reasonable time. There are mainly two types of mesh that exist: structured and unstructured. Unstructured mesh is more suitable for complex geometries such as those found in packed beds. This section discusses the different mesh strategies found in literature for packed beds.

Calis *et al.* (2001) use a tetrahedral and prism layers mesh in their simulations. The edge lengths are  $d_p/32$  and  $d_p/13$  for laminar and turbulent flow simulations respectively. The laminar flow mesh uses five prism cell layers on the particle and wall surfaces, with the first prism layer thickness equal to about  $0.004d_p$  and a growth rate of 1.2. Atmakidis and Kenig (2009) also used a similar mesh for laminar flow simulations in their study. No prism layers are used for turbulent flow mesh.

Dixon and Nijemeisland (2001) use a tetrahedral mesh for their simulation. They mention that an unstructured mesh is necessary for the complex geometry of packed beds and that great care must be taken when meshing the areas in the particle-to-particle and particle-to-wall contact region.

Magnico (2003) simulate the fluid flow ranging from  $Re_p$ , 7 to 200, through a packed bed for using the direct numerical simulation (DNS) approach. The randomly packed bed consisted of several hundred spheres with aspect ratios of between 5.96 and 7.8. A structured grid was used which the author states avoids meshing problems around the contact points between particles. The spatial resolution used for the simulations was equal to  $d_p/40$  resulting in a mesh size between about 9 and 17 million cells for beds with 326 to 620 particles.

Ookawara *et al.* (2007) use a tetrahedral mesh in their packed bed simulations. Details about the mesh size is not given but Dixon *et al.* (2013) estimate that a mesh size of  $d_p/10$  was used in the Ookawara *et al.* (2007) study. Kuroki *et al.* (2007) did complementary work to the previously mentioned study, showing that the mesh size has an effect on  $Nu$ . The study concludes that the minimum mesh density can be determined by looking at the thickness of the momentum boundary layer related to the  $Re_p$  and the first cell height. The authors mention that the purpose of this hypothetical approach is to enable the modelling of real pack beds while keeping the mesh size within a reasonable size.

Bai *et al.* (2009) use an unstructured tetrahedral mesh for two packed beds containing spheres and cylinders. The spherical and cylindrical bed particles are

reduced by 0.5% and 1% respectively. A mesh of two different sizes,  $d_p/14$  and  $d_p/10$  were needed to avoid grid generation problems respectively. The mesh size was taken as the edge length of a tetrahedral element.

Eppinger *et al.* (2010) specified a surface mesh size and then generated the volume mesh based on the surface mesh. The triangle edge sizes for the surface mesh of the particles were between  $d_p/25$  to  $d_p/10$ . Two boundary layers were used with a total thickness of  $0.03d_p$ . The mesh sizes range from 1 to 5.7 million for packed beds containing 80 to 750 particles.

Dixon *et al.* (2011) systematically develop a mesh for a fixed packed bed reactor by validating the mesh of a single sphere case. The study found that the total thickness of the prism layers must be approximately 60% of the momentum boundary layer thickness. It is recommended that the first layer thickness is thin enough to keep the  $y^+$  value below 2. The boundary layer thickness is approximated in their study by equation 2.4.1. This gives the momentum boundary layer thickness at the forward stagnation point and the assumption is made that it holds for the entire particle. This equation is only used as a guide to develop a mesh.

$$\frac{\delta_{BL}}{d_p} = 1.13Re_p^{-0.5} \quad (2.4.1)$$

Dixon *et al.* (2012) use a tetrahedral mesh without prism layers. The criterion they looked at was the radial temperature profile. They concluded that an unstructured mesh with cells sizes of  $d_p/20$  and no boundary layer was sufficient for their simulations. The authors also performed a mesh refinement study with mesh sizes of  $d_p/15$ ,  $d_p/20$  and  $d_p/25$ . The mesh sizes were 11.34, 27.36 and 42.82 million, respectively for a bed containing 1000 spheres. The results were found to be very close for all three meshes and it suggests that even the coarse mesh is independent. However, at lower  $Re$ , the  $d_p/15$  mesh showed that it could possibly be too coarse.

#### 2.4.4 Contact treatment

Contact treatment is a crucial factor when trying to model a packed bed in CFD. Mathematically a contact point has an area of zero. Therefore to represent it mathematically with a mesh would require infinitely fine or highly skew cells. Very fine cells could lead to a large computational cost and very skew cells could cause convergence problems (Eppinger *et al.*, 2010). To overcome this problem various methods found in literature have been developed and can be grouped into two categories: global and local methods. This section discusses the global contact treatment methods followed by the local contact treatment method.

The most used contact treatment method found in literature is shrinking the particles in the packed bed by a certain percentage of the particle's diameter to create gaps between the particles. The diameter of the particles is usually decreased in the range of between 0.5% and 2%. This allows cells to be generated

between the particles, avoiding fine and skew cells. However, the contraction of the particles reduces the solid fraction of the bed, and therefore a porosity correction and pressure drop correction is usually required. Studies that have used this method include: Augier *et al.* (2010); Bai *et al.* (2009); Calis *et al.* (2001); Nijemeisland and Dixon (2001); Reddy and Joshi (2008); Yang *et al.* (2010).

Another method is to enlarge the particle diameter so that the particles overlap each other in the vicinity of the contact point, thus eliminating the contact point by replacing it with a contact line. This allows cells to be generated around the contact lines. This method also changes the solid fraction of the bed and a porosity and pressure drop correction is required. Guardo *et al.* (2004) use this method, however the method was criticised by Ookawara *et al.* (2007), commenting that enlarging the particles could possibly result in additional narrow regions between particles which would cause meshing problems.

Eppinger *et al.* (2010) resolve the contact point problem by locally flattening the particle in the region of the contact point as well as particles in near contact with each other or the wall. They did this by meshing the particles surfaces and calculating the distance between the surfaces; if two surfaces are closer than a preset minimum distance, the vertices of the surface elements were moved to the preset minimum distance. The minimum distance allowed between two surfaces was set to 12% of the mesh size (see Section 2.4.3). This allowed cells to be generated between the particles. This method caused only a small modification to the geometry and as a result did not require any correction for the porosity and pressure drop.

Ookawara *et al.* (2007) connect the particles in contact or in near contact with each other or the wall with a cylindrical bridge. The authors refer to this method as the interparticle bridge model. Using this method resolved the problem of fine cells and skew cells being generated around the contact point. The study assumed that the cylindrical bridge existed in the stagnation region observed experimentally and numerically by Suekane *et al.* (2003) and Gunjal *et al.* (2005) respectively in the region of the contact point. The study concludes that macroscopic flow properties such as the pressure drop are not affected by the cylindrical bridge between the particles. No information is provided about the effect of the interparticle bridge on the porosity (Ookawara *et al.*, 2007). Louw *et al.* (2012) investigates the effect of the bridge model on porosity for structured and randomly packed beds. Figure 2.1 shows that the denser packed beds are affected more by the bridge model. The study recommends a bridge size in the range of  $0.2 \leq d_b/d_p \leq 0.3$  based on the porosity and pressure drop. An illustration of the local flattening and bridge particle treatments are shown in Figure 2.2.

Dixon *et al.* (2013) determine the effect of the four methods discussed above on the drag coefficient and heat flow for particle-to-particle and particle-to-wall contact. They refer to the methods used by Eppinger *et al.* (2010) and Ookawara *et al.* (2007) as the cap and bridge contact treatment methods. The current study will also use these terms when describing these methods. Dixon *et al.* (2013) recommend using the cap and bridge methods for flow and pressure drop. For

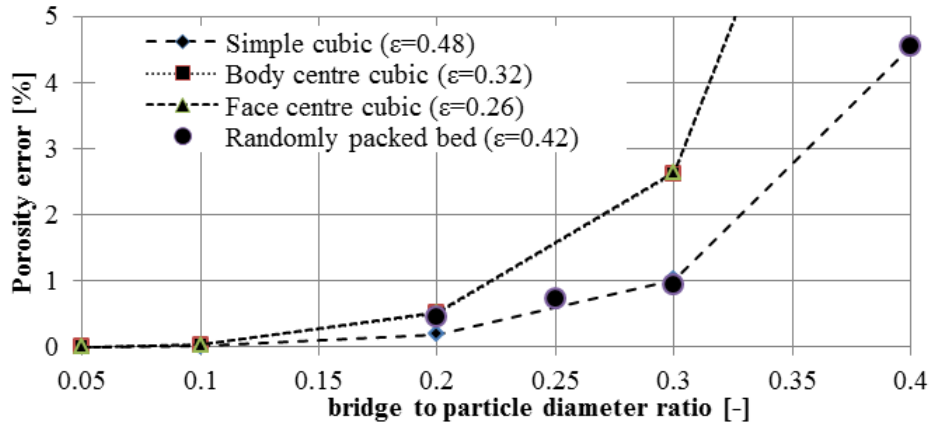
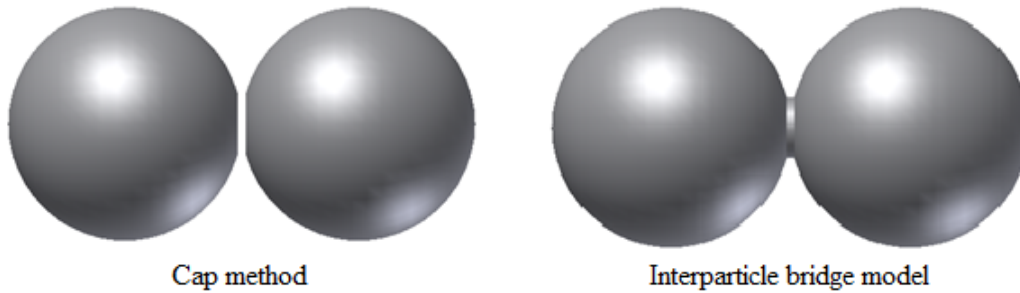

 Figure 2.1: Effect of the bridge model on the global porosity (Louw *et al.*, 2012)


Figure 2.2: Local flattening and Interparticle bridge methods

conjugated heat transfer problems where the particles are meshed, the bridge model is preferred. This model sets the bridge conductivity to a calculated effective conductivity ( $k_{\text{eff,bridge}}$ ) that replaces the original particle-fluid-particle conduction pathways with a single bridge conduction pathway. The recommended gap ( $H_{\text{sph}}$ ) and bridge sizes ( $d_b$ ) for the cap and bridge model respectively are shown in table 2.1.

 Table 2.1: Recommended size ranges for cap and bridge methods (Dixon *et al.*, 2013)

Method	$Re_p \leq 2000$	$Re_p \geq 2000$
Cap (Flow and pressure drop)	$0.005d_p \leq H_{\text{sph}} \leq 0.013d_p$	$H_{\text{sph}} \leq 0.007d_p$
Bridge (Flow and pressure drop)	$0.1 \leq d_b/d_p \leq 0.4$	$d_b/d_p \leq 0.2$
Bridge (Heat transfer)	$d_b/d_p \leq 0.2$	$d_b/d_p \leq 0.1$

## 2.5 Conclusion

To date no commercial CSP plant in the world uses an air-rock bed TES system. However, there is much interest in this type of TES system. The potential high efficiencies of such a system, the inexpensive and environmentally friendly material and the availability of suitable rock types in South Africa are the key driving points that make this system attractive.

Previous work shows the importance of modelling an air-rock bed system from a system design point of view. The increase in computational power over the past year has enabled us to model thousands of charge/discharge cycles to determine the long term behaviour of such a storage system. The optimum combination of storage parameters, such as particle size, bed height, mass flux, temperature porosity, bed layout and so on, can be calculated using numerical models.

The most common numerical method found in the literature reviewed to simulate an air-rock TES system, is a one dimensional plug flow numerical model. These models are able to include the effect of thermal losses to the environment, radiation between the particles and voids, axial conduction, destratification and temperature gradients in large particles. However the models found only simulated fairly simple bed geometries such as cylindrical or rectangular beds.

There is not a lot of literature found regarding discrete CFD simulations of flow through a packed bed containing other particles than spheres. No clear cut method to model irregularly shaped particles such as rocks could be established. However the literature shows that CFD does potentially possess the capability to model flow through a packed bed of rocks.

## 3. Methods

### 3.1 Characteristics of packed beds

This section describes porous media with specific focus on packed beds as a porous media. The typical characteristics of packed beds, which DEM must reproduce, are outlined. The characteristics are porosity (global, radial and axial variation), the effect of confining walls and particle size and shape.

#### 3.1.1 Porous media

According to Bejan and Nield (2006), a porous media is defined as a material consisting of a solid matrix with interconnecting voids that allow one or more fluids to pass through the material. Following this definition, a packed bed of particles can thus be considered a porous media. The distribution of the pores in a randomly packed bed in terms of size and shape is highly irregular, and, therefore, the flow through these pores is also highly irregular. In experiments, the quantities of interest are measured over areas that contain many pores, and such space average quantities change in a regular manner with respect to time and space and hence are applicable theoretical treatments (Bejan and Nield, 2006).

#### 3.1.2 Porosity

Porosity is defined as the fraction of the total volume of the medium occupied by void space. The porosity ( $\varepsilon$ ) is calculated by Equation 3.1.1

$$\varepsilon = \frac{V_V}{V_T} = 1 - \frac{V_S}{V_T} \quad (3.1.1)$$

where  $V_V$ ,  $V_S$  and  $V_T$  represent the void, solid and total volume of the porous media respectively. For packed beds of spheres of uniform diameter the porosity can vary between the limits of 0.26 (rhombohedra) and 0.48 (SC). Non-uniform particle sizes tend to lead to smaller porosities than uniform particle sizes because smaller particles fill the pores formed by larger ones (Bejan and Nield, 2006).

### 3.1.3 Wall effect on bulk density

The particle size to tube diameter ratio referred to in this study as the aspect ratio ( $D/d_p$ ), has an effect on the bulk porosity (Atmakidis and Kenig, 2009).

The bulk porosity increases with increasing aspect ratio from 1 to 2 for a packed bed of spheres. Below or equal to 2, the spheres cannot slip past one another and are forced to arrange in a staggered string formation leaving large void spaces. As the aspect ratio increases beyond 2, the porosity decreases (Dixon, 1988). Three different regions in terms of the mechanism of the wall effect exist. Region one is for beds with an aspect ratio greater or equal to about 3.9, where the disordered packing outweighs the ordered packing. The second region is the transition region, where the transition from disorder dominated packing to ordered dominated packing takes place and lies approximately between  $2 \leq D/d_p \leq 3.9$ . In the third region, only ordered packing can be observed, and the region is about  $D/d_p \leq 2$  (Zho and Yu, 1995). Equation 3.1.2 is the correlation for the bed porosity as a function of the aspect ratio from the experimental work of Dixon (1988).

$$\varepsilon = 0.4 + 0.05 \frac{d_p}{D} + 0.412 \left( \frac{d_p}{D} \right)^2, \text{ for } \frac{D}{d_p} \geq 2 \quad (3.1.2)$$

The equation shows that for an infinitely large bed, the porosity strives to 0.4. The loose and dense packing correlations of Zho and Yu (1995) are represented below in Equation 3.1.3 and 3.1.4 respectively.

$$\varepsilon = 0.4 + 0.01 \left( e^{10.686 \frac{d_p}{D}} - 1 \right), \text{ for } \frac{D}{d_p} \geq 3.906 \quad (3.1.3)$$

$$\varepsilon = 0.372 + 0.002 \left( e^{10.686 \frac{d_p}{D}} - 1 \right), \text{ for } \frac{D}{d_p} \geq 3.906 \quad (3.1.4)$$

The correlations show that for an infinitely large loose and densely packed bed, the porosity strives towards 0.4 and 0.372 respectively. All three correlations are plotted in Figure 3.1. It can be seen from the figure that Equation 3.1.2 is more comparable to Equation 3.1.3. This could possibly be because Dixon (1988) packing method of slowly pouring the particles by hand without attempting to induce settling, resulted in a fairly loose packing. As seen in Figure 3.1, for an aspect ratio above 30, disorder packing seems to be totally dominant and the wall effect on the global porosity appears negligible.

### 3.1.4 Radial porosity variation

The surrounding walls of a packed bed influence the radial porosity. For the case of a packed bed of uniform spheres, the spheres at the container walls are well-ordered with each other. The subsequent layers away from the wall become less ordered, until a totally randomized packing is attained (Mueller, 1991). The

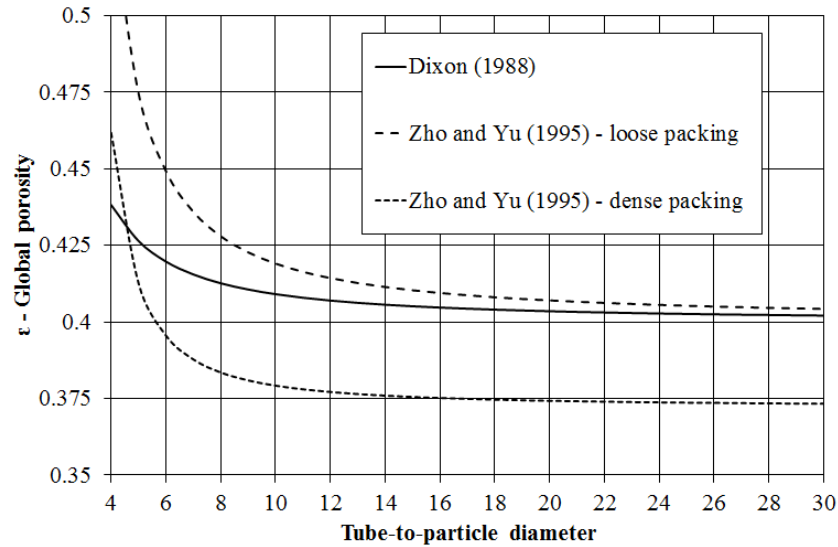


Figure 3.1: Bulk porosity vs. tube-to-particle diameter correlations

porosity variation represents a damped oscillatory behaviour in the region near to the wall and approaches a constant porosity at 4 to 5 particle diameters away from the wall. This variation is considered to greatly influence the calculation of the pressure drop for beds with small aspect ratios (smaller than 10) (Eppinger *et al.*, 2010). The flow and heat transfer is also affected (Theron, 2011).

Mueller (1991) correlated experimental data from literature to produce an empirical model which consists of a principle equation for the radial porosity distribution and includes a damping function. The empirical correlation has been determined for the radial porosity  $\epsilon_r$  at a position  $r$  away from the wall. Mueller's correlation is shown in Figure 3.2 for beds with aspect ratios larger than 2.61.

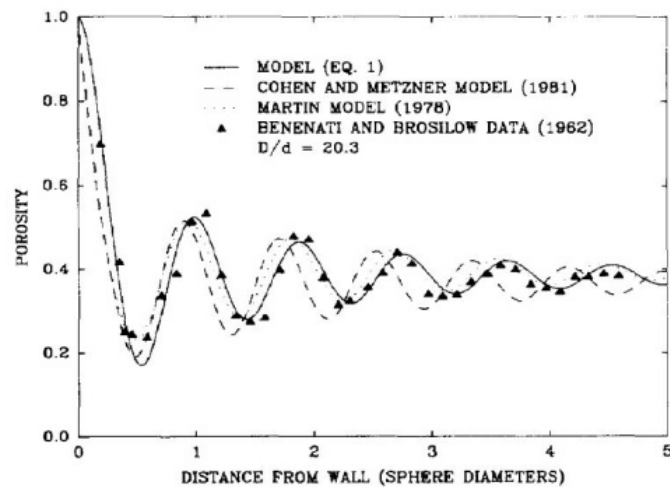


Figure 3.2: Radial porosity variation (Mueller, 1991)

### 3.1.5 Axial porosity variation

Auwerda *et al.* (2010) determine the axial porosity variation of three computationally generated packed beds containing spheres using DEM, Monte Carlo rejection and expanding system. The aspect ratio of the bed was 18 with a height to particle size ratio of more than 18. Figure 3.3 shows the results of the axial porosity variation. As seen in the Figure 3.3, the porosity at the top of the bed is

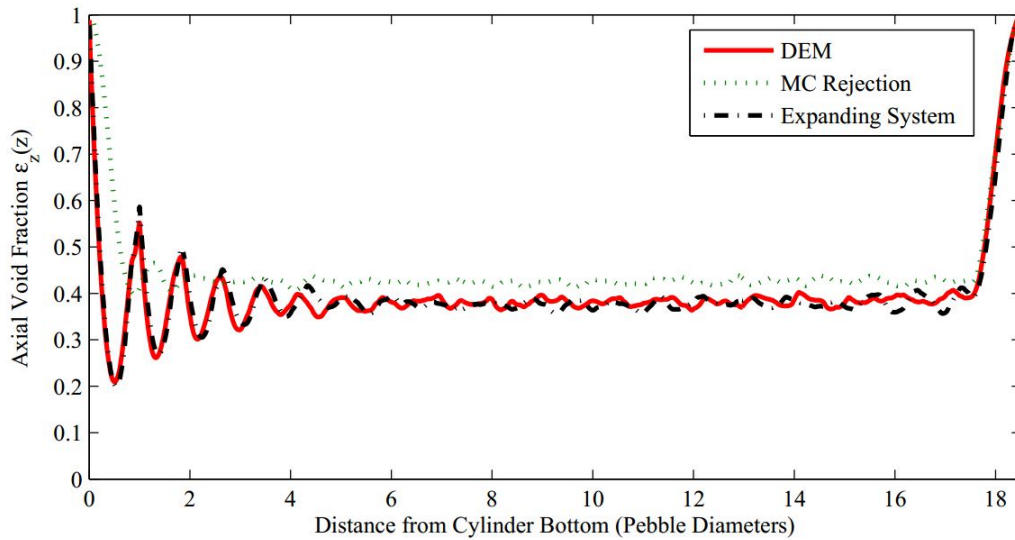


Figure 3.3: Axial porosity variation (Auwerda *et al.*, 2010)

nearly unity, and no damped oscillation or boundary effect is seen as one would expect, because it is a free boundary, which imposes no restraints on the location of the spheres (Auwerda *et al.*, 2010). The axial porosity variation at the bottom of the packing resembles the same damped oscillation behaviour as for the radial porosity variation. Both the magnitude and period are actually comparable with the radial porosity variation, and likewise, after 4 to 5 particles the porosity in the axial direction stays nearly constant (Auwerda *et al.*, 2010).

### 3.1.6 Particle characterization

Describing the size of an irregular particle is not simple, especially for rock particles that have a highly irregular shape. Equivalent spherical diameters are commonly used to simplify the description where some physical property of the particle is related to a sphere with a similar property (e.g. volume, surface area, circumference, specific surface area). The equivalent spherical diameter for the same particle varies depending on the chosen property used to relate it to a sphere, as shown in Figure 3.4. According to Holdich (2002) the most appropriate property to use for fluid flow is the specific surface area ( $S_v$ ) of the particle,

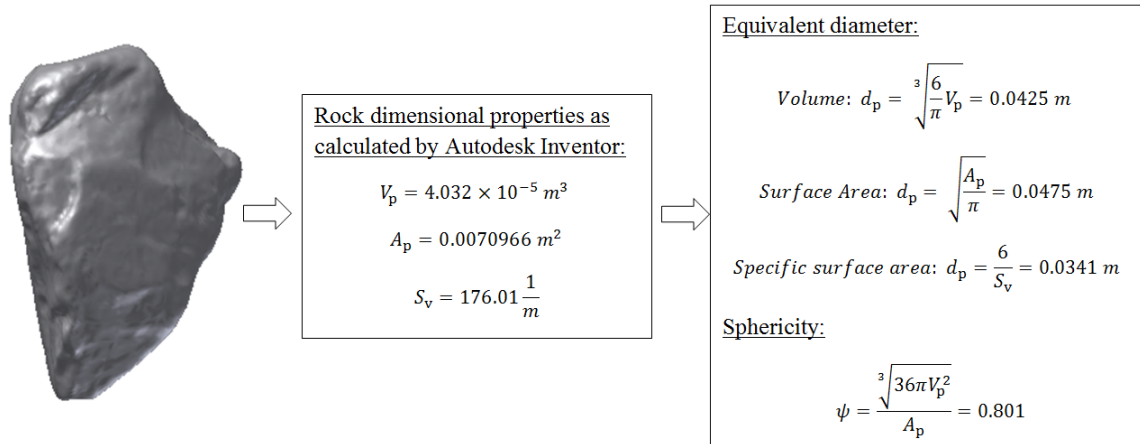


Figure 3.4: Example of particle equivalent diameter

which is defined as the surface area divided by the volume of the particle as given in Equation 3.1.5.

$$S_v = \frac{A_p}{V_p} \quad (3.1.5)$$

For a single sphere it can be shown that  $S_v = 6/d_p$ ; therefore, the equation for the equivalent spherical diameter based on the specific surface area is

$$d_{p_{Sv}} = \frac{6V_p}{A_p} = \frac{6}{S_v} \quad (3.1.6)$$

For irregular particles, an equivalent particle size based on the side length of a cube with an equal volume is suggest by work discussed in Allen (2010).

To describe the shape of a particle the Wadells sphericity (Equation 3.1.8) is often used, which uses the fact that a sphere has the smallest surface area per unit volume of any shape (Singh *et al.*, 2006). Therefore the sphericity ( $\psi$ ) will be either unity or a fraction.

$$\psi = \frac{\text{surface area of a sphere of equal volume to the particle}}{\text{surface area of particle}} \quad (3.1.7)$$

$$\Rightarrow \psi = \frac{(36\pi V_p^2)^{1/3}}{A_p} \quad (3.1.8)$$

The following relationship between the equivalent spherical diameter based on volume, specific surface area and the sphericity should be noted.

$$d_{p_{Sv}} = d_{p_v} \psi = \left( \frac{6V_p}{\pi} \right)^{1/3} \frac{(36\pi V_p^2)^{1/3}}{A_p} = \frac{6V_p}{A_p} \quad (3.1.9)$$

When determining the particle size for a packed bed containing non-uniform particles, an average particle size must be determined. Allen *et al.* (2012) determined the average particle size for a packed bed containing non-uniform rocks

by using a three dimensional laser scanning technique for a sample set of the rock particles contained in the bed. The particle's surface area and volume is determined for each rock in the sample set. After obtaining all the data, the Equation 3.1.10 is used to determine the average particle size of the rock bed (Allen, 2012).

$$d_{p_{sv}} = \frac{6 \sum V_p}{\sum A_p} \quad (3.1.10)$$

The same method is used in this study to determine the average particle size in a packed bed containing non-uniform particles.

### 3.1.7 DEM

DEM is a numerical method used to generate the random packing of particles under the influence of gravity. It computes the stresses and displacements in a volume containing a large number of granular particles. The interactions between each particle are considered explicitly. The shape of the particle is specified by the user and is mostly spherical or ellipsoidal particles. Figure 3.5 graphically illustrates the DEM process of drop particles from the top into a cylindrical container. The commercial DEM software, *PFC<sup>3D</sup>*, is used in this study. It can

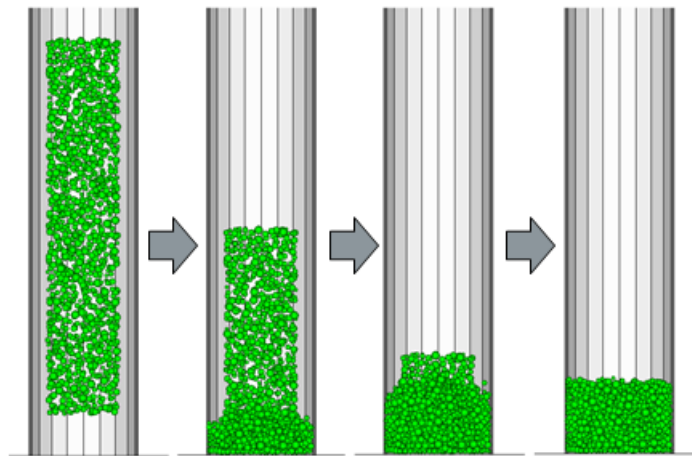


Figure 3.5: Generating a packed bed with DEM (courtesy of R.G. Nel)

only model spherical particles and uses clump logic to model irregular particles (Itasca Consulting Group, 2003). Clump logic approximates a particle shaped by clumping together a number of spheres. The accuracy of the particle shape increases as the number of spheres per clump increase, but this also increases the computational costs. Therefore, an optimum relationship between accuracy and computational cost must be found when creating a clump. When creating a

bed containing clump particles for CFD application the following should be considered: each clump particle must not be overly complicated so that it requires a very fine mesh as this is very computationally expensive, especially if the bed contains hundreds of particles.

The detail regarding the DEM theory and model setup is beyond the scope of this study. The reader should refer to Nel (2013) for more information regarding DEM and rock packed beds. Nel (2013) provides the geometries used in this study by using DEM. This author's work ensured that the geometries used were accurate in terms of porosity and particle shape.

### 3.1.7.1 Irregular particles

With clump logic, non-spherical particle shapes are represented by a number of spheres clumped together. The rocks' irregular shape can be modelled by means of the clump logic. Firstly the actual rock particle is scanned to create a numerical model of the rock particle and then the shape can be approximated by a clump model. This process is illustrated in Figure 3.6. The figure shows that the accu-

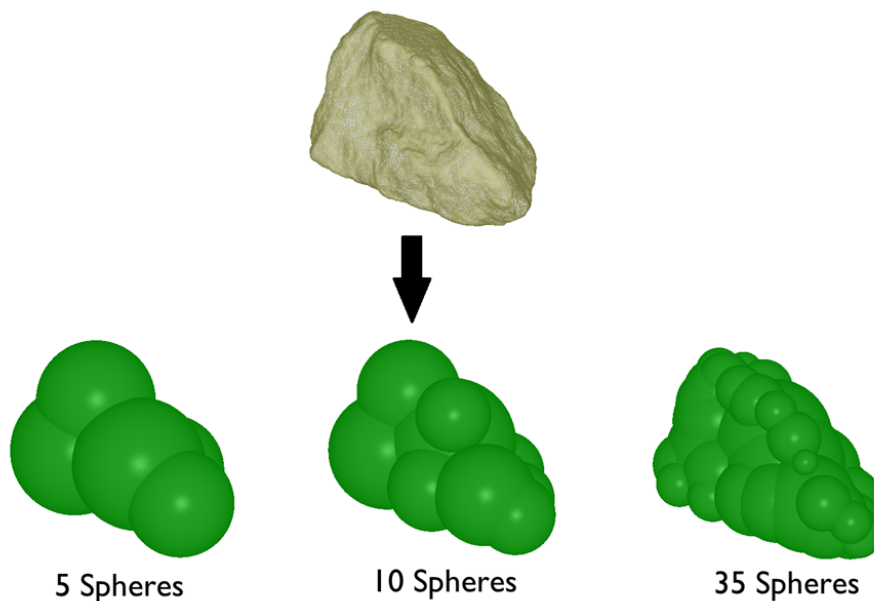


Figure 3.6: Rock particle represented by a clump model (courtesy of R.G. Nel)

racy of the approximated rock shape can be improved by increasing the number of spheres that represent it, but this also increases the computational cost.

DEM can accurately model the packing of rock particles under the influence of gravity by representing the actual shape of the rock particle with a clump model (Nel, 2013). However, doing so presents problems for CFD application because the particle surface of the rock clump model is very complex, as can be

seen in Figure 3.6. Preliminary mesh trials done by this study found that such a bed requires a very fine surface mesh, and a bed containing hundreds of particles would be computationally very expensive. Therefore, it is necessary to find simpler particle shapes to represent the rock particles in the packed bed.

A study by Horn (2012) presents a possible solution to this problem. The study used visual inspection to determine rock particles size and shape distribution. Three typical shapes were identified from eight random samples taken from a large rock pile. The study assumed that only three shapes, namely, spherical, elongated and pyramid were present in the larger sample. The rock particles that were used were crushed rock using a roller mill with a hole opening of 25 mm. The results from the simulation agreed well with experimental results. The three rock types were found to be valid assumptions. The following size distribution for the particles given in Table 3.1 was used in the simulation. A Gaussian distribution of the radii was generated. The particle radii corresponded to the radii of a sphere with an equivalent volume. The Table also shows the distribution of each type of particle in the bed based on the total number of clump particles.

Table 3.1: Horn (2012) particle size and particle volume distribution

Shape	Minimum radii [mm]	Maximum radii [mm]	Particle distribution [%]
Spherical	7.5	10.5	20.80%
Elongated	12	15	41.70%
Pyramid	15	16.2	37.50%

The equivalent clump models are shown in Figure 3.7 and Figure 3.8. It can be seen that the elongated and pyramid equivalent shapes simply consist of two and four equivalent diameter spheres clumped together respectively.

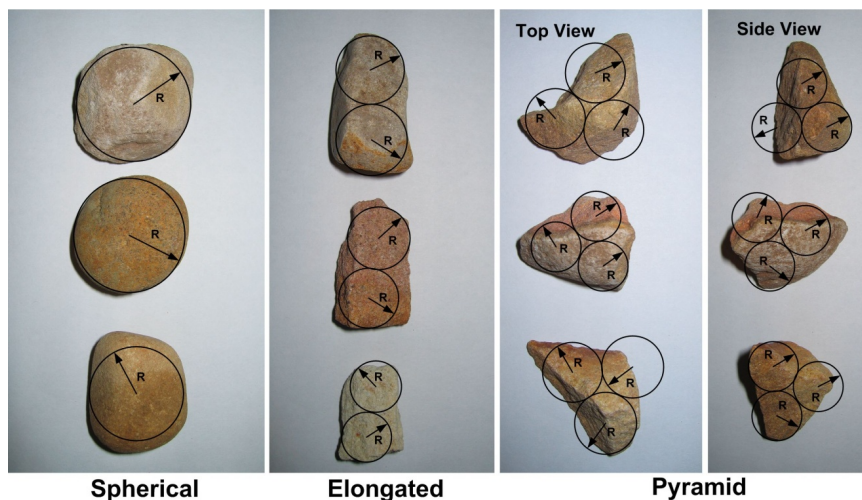


Figure 3.7: Rock particles with superimposed clump equivalents (Horn, 2012)

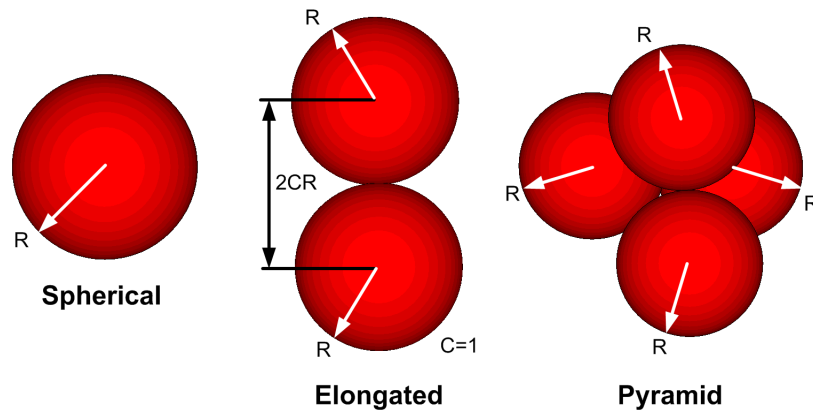


Figure 3.8: Equivalent clump particle shapes (Horn, 2012)

The elongated and pyramid shapes, however, must be modified to eliminate the contact point in the elongated particle and the void in the pyramid particle. A third sphere with half the radius of the other two spheres is added to the elongated particle and a fifth sphere with the same diameter as the other four spheres is added to the pyramid particles. The modified equivalent particle shapes are shown in Figure 3.9.

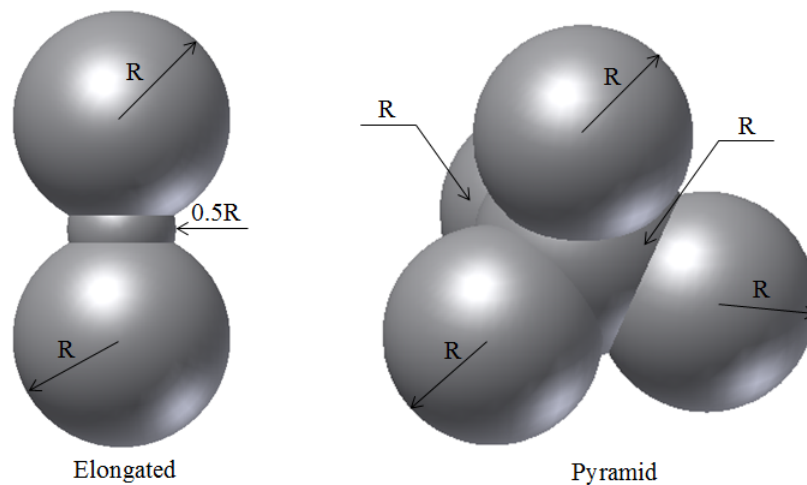


Figure 3.9: Modified elongated and pyramid clump particle shapes

## 3.2 Flow and heat transfer through packed beds

This section discusses correlations found in literature for packed beds friction factors and heat transfer coefficients. The Reynolds number definitions for packed beds are discussed in Appendix D.

### 3.2.1 Pressure drop

The relationship between the pressure gradient and the flow velocity in a porous media was firstly experimentally established by Darcy in 1856 (Verboven *et al.*, 2006). The relationship is known as Darcy's law and it is given below (Holdich, 2002).

$$\frac{\Delta P}{L} = -\frac{\mu}{k} \frac{dV}{dt} \frac{1}{A_{cs}} \quad (3.2.1)$$

where  $A_{cs}$  is the cross-sectional area of the bed,  $V$  is the volume of fluid flowing in time  $t$ ,  $\mu$  is the fluid viscosity and  $k$  is the permeability of the bed. Noting that the superficial velocity  $U_0$  is

$$U_0 = \frac{\dot{V}}{A_{cs}} = \frac{dV}{dt} \frac{1}{A_{cs}} \quad (3.2.2)$$

Equation 3.2.1 can be rewritten as

$$\frac{\Delta P}{L} = -\frac{\mu}{k} U_0 \quad (3.2.3)$$

The viscosity and permeability provides the flow resistance. The permeability  $k$  depends on many factors, but the most important is the pore size, the porosity and the pore geometry (Verboven *et al.*, 2006). The Kozeny-Carman equation gives an analytical expression for the permeability given. It was derived from the Hagen-Poiseuille equation and assumed that the flow through a porous media can be represented as flow through a large bundle of parallel channels (Holdich, 2002). The equation is shown below

$$\frac{\Delta P}{L} = -\mu \left[ \frac{36K(1-\varepsilon)^2}{\varepsilon^3 d_p^2} \right] U_0 \quad (3.2.4)$$

This shows that the permeability is dependent on the porosity and particle diameter (Holdich, 2002). Forchheimer (1930), found in Carman (1937), shows that Darcy's law breaks down for larger flow velocities. Carman (1937) notes that turbulence occurs at  $Re_1 = 2$  (see Appendix D) and is very similar to the onset of turbulence in a straight pipe, but the transition from laminar to turbulent is very gradual. Forchheimer suggest that this may be due to the variation in pore size within the bed, with the turbulence first occurring in the larger pore sizes, and proposes the following type of equation

$$\Delta P = aU_0 + bU_0^n \quad (3.2.5)$$

where  $a$ ,  $b$  and  $n$  are bed characteristic constants with  $n$  between 1.6 and 2.0 (Carman, 1937). An inertial term is added to the Darcy equation which considers

the inertial effects that dominate in high fluid velocity flow. The Forchheimer law is given below (Verboven *et al.*, 2006).

$$\frac{\Delta P}{L} = -\frac{\mu}{k}U_0 - \frac{C\rho_f}{k^{1/2}}U_0^2 \quad (3.2.6)$$

here  $C$  is the Forchheimer coefficient and  $\rho_f$  is the fluid density. The Forchheimer coefficient,  $C$ , is primarily dependant on the geometry of the pore space.

Ergun (1952), found in Verboven *et al.* (2006), derives the most well-known formulation, shown in Equation 3.2.6. Ergun showed that for a porous medium that consisted of near spherical particles, the permeability,  $k$ , and Forchheimer coefficient,  $C$ , is as shown below (Verboven *et al.*, 2006).

$$\frac{1}{k} = -\frac{K_1(1-\varepsilon)^2}{\varepsilon^3 d_p^2} \quad (3.2.7)$$

$$C = -\frac{K_2}{K_1^{1/2}\varepsilon^{3/2}} \quad (3.2.8)$$

where  $K_1$  and  $K_2$  are constants. Substituting Equations 3.2.7 and 3.2.8 into Equation 3.2.6,

$$\frac{\Delta P}{L} = \left( \frac{K_1(1-\varepsilon)}{U_0 d_p} \mu + K_2 \right) \frac{(1-\varepsilon)}{d_p \varepsilon^3} \rho_f U_0^2 \quad (3.2.9)$$

noting that,  $Re_{Erg} = \rho_f U_0 d_p / (1-\varepsilon)\mu$  (see Appendix D), Equation 3.2.9 can be rewritten as,

$$\frac{K_1}{Re_{Erg}} + K_2 = \frac{\Delta P}{L} \frac{\varepsilon^3}{(1-\varepsilon)} \frac{d_p}{\rho_f U_0^2} \quad (3.2.10)$$

where the friction factor is defined as

$$f_{Erg} = \frac{\Delta P}{L} \frac{\varepsilon^3}{(1-\varepsilon)} \frac{d_p}{\rho_f U_0^2} \quad (3.2.11)$$

The values for  $K_1$  and  $K_2$  for randomly stacked spheres differ from source to source. The original parameters are 150 and 1.75 for  $K_1$  and  $K_2$  respectively, others have suggested 180 and 1.8. Particles that deviate greatly from a sphere in terms of surface roughness and particle shape have been shown to have other values of these constants (Verboven *et al.*, 2006).

Carman (1937) notes that the decrease in permeability compares less to the onset of turbulence and more to the increase in resistance displayed by curve calipers as compared with straight calipers; therefore Forchheimer's hypothesis is not used. The author extended the pipe flow analogy to cover both the laminar and turbulent flow regimes. This method related the shear stress at the surface of the solid particles to the pressure drop. The friction factor is defined as  $R/\rho_f U^2$ ,

with  $R$  representing the drag force per unit area. The surface area of the particles is defined as  $S_v(1 - \varepsilon)LA_{cs}$ , where  $L$  and  $A_{cs}$  make up the length and cross sectional area of the packed bed. The drag force is equal to  $R \cdot S_v(1 - \varepsilon)LA_{cs}$ . The pressure drop force per unit area on the fluid is given as  $\Delta PA_{cs}\varepsilon$ . The shear force,  $R$ , is determined by doing a force balance of the drag force and pressure force on the fluid, and with some algebra it can be shown that the packed bed friction factor is defined as given in Equation 3.2.12 (Holdich, 2002).

$$f_{\text{Carman}} = \frac{\Delta P}{L} \frac{\varepsilon^3}{S_v(1 - \varepsilon)} \frac{1}{\rho_f U_0^2} \quad (3.2.12)$$

Carman (1937) plots several sets of experimental data (for glass spheres and lead shot particles) found in literature with the friction factor as given in Equation 3.2.12 on the vertical axis and  $Re_1$  on the horizontal axis. The particle sizes ranged from 0.0025 m to 0.0905 m and the porosity ranged from 0.30 to 0.42. The flow range is between  $0.01 \leq Re_1 \leq 13000$ . The Equation shown below is said to best fit the data

$$f_{\text{Carman}} = \frac{5}{Re_1} + \frac{0.4}{Re_1^{0.1}} \quad (3.2.13)$$

The author points out that Equation 3.2.13 is a Forchheimer type equation. If we combine Equation 3.2.12 and 3.2.13, it is more clear, as shown in Equation 3.2.14

$$\frac{\Delta P}{L} = \frac{5S_v^2(1 - \varepsilon)^2\mu}{\varepsilon^3} U_0 + \frac{0.4S_v^{1.1}(1 - \varepsilon)^{1.1}\mu^{0.1}\rho_f^{0.9}}{\varepsilon^3} U_0^{1.9} \quad (3.2.14)$$

with  $a = (5LS_v^2(1 - \varepsilon)^2\mu/\varepsilon^3)$ ,  $b = (0.4LS_v^{1.1}(1 - \varepsilon)^{1.1}\mu^{0.1}\rho_f^{0.9})/(\varepsilon^3)$  and  $n = 1.9$  (refer to Equation 3.2.5). Carman (1937) also plots pressure drop data of non-spherical particles (wire spirals, saddles and lessing rings) gathered from literature. At low Reynolds numbers both non-spherical particles and spherical particles have similar friction factors. Only the saddle and wire spirals agree well with the sphere results, even in the turbulent region. The shape factor of both the particles are known. The shape factor is similar to the sphericity and work on the principle of a sphere having the minimum specific area. There is unity for the shape factor of a sphere and less than unity for all non-spherical particles. At  $0.5 \leq Re_1 \leq 20$  the lessing rings show a steady deviation from the curve after which it remains roughly double the value of the sphere results. The authors propose that the differences between the particles are because the entire surface areas of the spiral and saddle particles are equally exposed to the flow, where the interior of the ring particles may be a source for eddies and dead spaces for higher flow rates. The authors suggest using a value 2.5 times higher than  $f = 0.4/Re_1^{0.1}$  for a fixed bed containing ring particles when designing a bed that will operate in the turbulent flow regime to ensure a safe design. Therefore it is proposed that  $f = 1.0/Re_1^{0.1}$  for the turbulent regime for beds containing ring particles.

Allen *et al.* (2012) propose using the apparent friction factor for duct flow ( $f_{\text{duct}}$ ) to predict the pressure drop, arguing that it accounts for skin friction and form drag.

$$f_{\text{duct}} = \frac{\Delta P}{L} \frac{2d_h}{\rho_f u^2} \quad (3.2.15)$$

The Reynolds number for a duct is,  $Re_{\text{duct}} = \rho_f u d_h / \mu$ , where the  $d_h$  is the hydraulic radius and  $u$  is the average flow speed through the duct. The author considers a structured packing which is divided into repeatable control volumes with the pitch in the flow direction denoted by  $P_l$ . The hydraulic diameter is defined in Equation 3.2.16 below,

$$d_h = \frac{4A_{\text{cs}}P_l}{\sum A_p} = \frac{4\varepsilon \sum V_p}{(1-\varepsilon) \sum A_p} \quad (3.2.16)$$

where  $A_{\text{cs}} = V_v / P_l$  and  $V_v = \varepsilon \sum V_p / (1-\varepsilon)$  and  $A_{\text{cs}}$  is average fluid cross sectional area and  $V_{\text{void}}$  is the void volume. The duct flow velocity is related to the superficial velocity.

$$u = \frac{U_0}{\varepsilon} \quad (3.2.17)$$

where  $u$  is the flow speed through the duct. The duct Reynolds number ( $Re_{\text{duct}}$ ) can now be written as,

$$Re_2 = \frac{4\rho_f U_0 \sum V_p}{(1-\varepsilon)\mu \sum A_p} \quad (3.2.18)$$

$Re_2$  is referred to as the Allen Reynolds number in this study. The relationship of  $Re_2$  with  $Re_1$  and  $Re_{\text{Erg}}$  are the following  $Re_2 = 4 \cdot Re_1$  and  $Re_2 = (2/3) \cdot Re_{\text{Erg}}$ . Substituting Equations 3.2.16 and 3.2.17 in 3.2.15 results in

$$f_{\text{Allen}} = \frac{\Delta P}{L} \frac{\varepsilon^3}{(1-\varepsilon)\rho_f U_0^2} \frac{\sum V_p}{\sum A_p} \quad (3.2.19)$$

Equation 3.2.19 is equal to Equation 3.2.12, noting that  $S_v = \sum A_p / \sum V_p$ . Allen *et al.* (2012) correlated an algebraic equation for the friction factor of a randomly packed bed of spheres from experimental results and from results from literature. The equation is also a Forchheimer type equation.

$$f_{\text{Allen}} = \frac{22.4}{Re_2} + \frac{0.546}{Re_2^{0.12}} \quad (3.2.20)$$

Allen *et al.* (2012) show with experiments that the Ergun equation over predicts the pressure drop for  $Re_2 > 500$  ( $Re_{\text{Erg}} = 750$ ). This deviation increases as the Reynolds number increases. Furthermore they did experiments with non-spherical particles and showed that surface roughness and particle shape has a large effect

on the pressure drop. Experimental results from randomly packed beds containing smooth squares and rough spheres show a notable higher pressure drop than for the smooth sphere. Beds containing crushed rock particles were also tested, showing that the packing direction of the rock particles plays a major role on the pressure drop. Co-current packing showed 50% higher pressure drop factors than for cross-current packing for the same particles. Although not all the experiments for the different particles was done for low Reynolds numbers ( $Re_2 \leq \pm 10$ ), they all seem to tend to the same approximate value of  $f$  for spherical particles in the laminar regime, no matter the particle shape, roughness or packing. This is similar to the observation made by Carman (1937).

Singh *et al.* (2006) correlate an equation that can be used to determine the pressure drop over a bed with non-spherical elements. Five different shapes were tested, and the friction factor was defined as

$$f_s = \frac{\Delta P}{L} \frac{d_p}{\rho_f U_0^2} \quad (3.2.21)$$

The correlation for the friction factor is given below and is a function of the Reynolds number ( $Re_p$ ), porosity and sphericity.

$$f_s = \frac{4.466}{Re_p^{0.2} \varepsilon^{2.945}} \psi^{0.696} e^{11.85(\log \psi)^2} \quad (3.2.22)$$

Equation 3.2.22 applies to the following range of bed parameters,  $1047 \leq Re_p \leq 2674$ ,  $0.306 \leq \varepsilon \leq 0.63$  and  $0.55 \leq \psi \leq 1.0$ .

Nuclear Safety Standards Commission (KTA) (1981) correlates an equation from experimental results for the pressure drop over a packed bed of smooth spheres. The definition they used for the friction factor and the correlation is given below (Nuclear Safety Standards Commission (KTA), 1981).

$$f_{KTA} = \frac{\Delta P}{L} \frac{\varepsilon^3}{(1-\varepsilon)} \frac{2d_p}{\rho_f U_0^2} \quad (3.2.23)$$

$$f_{KTA} = \frac{320}{1-\varepsilon} + \frac{6}{1-\varepsilon} Re_p^{0.1} \quad (3.2.24)$$

This equation applies to the following range of bed parameters,  $1 \leq Re_p \leq 100000$ ,  $0.36 \leq \varepsilon \leq 0.42$  and  $H \geq 5d_p$

### 3.2.2 Heat transfer

All three heat transfer mechanisms (conduction, convection and radiation) occur inside a packed bed during charging or discharging. When the packed bed is being charged or discharged, the dominant heat transfer mechanism is forced

convection; radiation and conductive heat transfer play a lesser role, depending on the flow rate. When the flow rate through the bed is zero or very low conduction, radiation and natural convection play a larger role. In Figure 3.10 the thermocline region in a packed bed is illustrated. The thermocline region is the transitional region in the bed between the hot and cold bed zones.

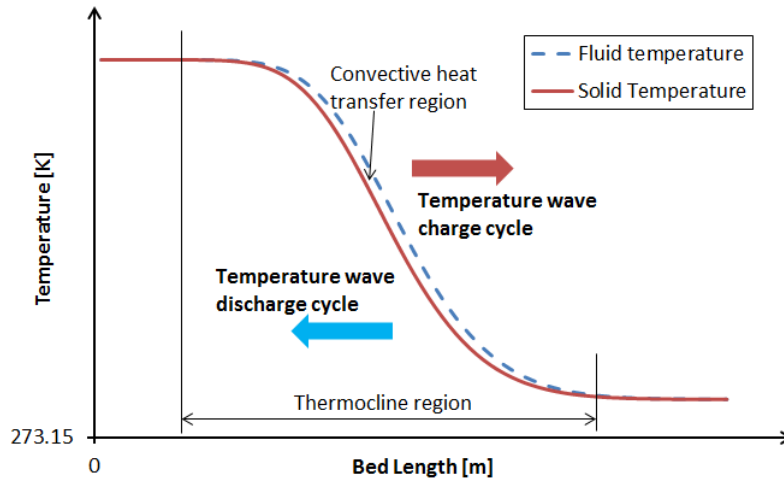


Figure 3.10: Packed bed thermocline

An effective thermal conductivity ( $k_{\text{eff}}$ ) is normally used for the packed beds. Generally the effective thermal conductivity is derived by lumping together all the relevant heat transfer mechanisms (van Antwerpen *et al.*, 2010). Vortmeyer and Schaefer (1974) lump together the effective stagnant conductivity and convective heat transfer mechanisms in order to derive an effective thermal conductivity for their one dimensional thermal model to describe the motion of the thermal wave. Bauer (1990), found in van Antwerpen *et al.* (2010), split the effective thermal conductivity of a packed bed in to three components: 1) effective stagnant conductivity, 2) enhanced fluid effective conductivity and 3) enhanced effective conductivity, due to the motion of both the fluid and solid phases. The third component is not applicable to this study because of the fixed solid structure of the rock packed bed. The second component is accounted for in the Nusselt number correlation.

The  $k_{\text{eff}}$  of interest is the stagnant fluid effective thermal conductivity, which consists of: a) conduction through the stagnant fluid and solid particles, b) conduction through the contact area between particles and c) radiation between the particles (van Antwerpen *et al.*, 2010). van Antwerpen *et al.* (2010) observed that the conduction through the contact area can be neglected for  $k_s/k_f < 10^3$  for a packed bed of spheres. From Tables E.1 and E.2 it can be seen that the  $k_s/k_f$  values do not exceed  $10^3$  for an air-rock bed. Therefore it is assumed in this study that for an air-rock bed the conduction through the contact area between rock particles can be neglected for the  $k_{\text{eff}}$ . This assumption may not be valid because

the contact area between rock particles should be larger. The coordination number and the contact angle also have a significant effect on  $k_{\text{eff}}$  (van Antwerpen *et al.*, 2010).

The upper and lower bounds of the solid and fluid effective thermal conductivity are given by  $k_{\text{a,eff}} = \epsilon k_f + (1 - \epsilon) k_s$  (parallel) and  $1/k_{\text{H,eff}} = k_f/\epsilon + k_s/(1 - \epsilon)$  (series) respectively as noted by Deissler and Boegli (1958), found in van Antwerpen *et al.* (2010). They are also the upper and lower bound for other thermal conductivity correlations. Additionally as long as there is no natural convection, experimental measurements for any porous structure saturated with a stagnant are also within these bounds (van Antwerpen *et al.*, 2010).

In convection studies, it is common practice to use the Nusselt number ( $Nu$ ) to non-dimensionalise the heat transfer coefficient ( $h$ ). The Nusselt number represents the ratio between convective and conductive heat transfer through a fluid layer. For a Nusselt number of 1 the heat transfer is purely conductive (Cengel, 2006). The Nusselt number is given in Equation 3.2.25

$$Nu = \frac{hL}{k_f} \quad (3.2.25)$$

where  $L$  is the characteristic length and  $k_f$  is the fluid conductivity. The characteristic length used for convective heat transfer in packed beds is  $d_p$ . It is convenient to use the volumetric heat transfer coefficient ( $h_v$ ) when study convective heat transfer through a packed bed. The surface heat transfer coefficient ( $h$ ) is related to the volumetric heat transfer coefficient as shown

$$h_v = a_{fs} h \quad (3.2.26)$$

where  $a_{fs}$  is the specific surface area of the bed and is given by

$$a_{fs} = \frac{6(1 - \epsilon)}{d_p} = S_v(1 - \epsilon) \quad (3.2.27)$$

This represents the wetted surface area per unit volume in the packed bed.

Löf and Hawley (1948) experimentally determined the heat transfer coefficient of a packed bed containing loose solids through transient methods. Their experiment consisted of a bed of gravel through which heated air was pumped. The inlet air temperature ranged between 37.78 °C and 121.11 °C and the flow rate ranged between 0.0789 and 0.4367 kg/m<sup>2</sup>s. The bed porosity ranged from 0.426 to 0.454. The volumetric heat transfer coefficient was determined by generating the Schumann curves from the knowledge of the bed properties and comparing the time-temperature experimental results to them. From the experimental data, an equation for the volumetric heat transfer coefficient was correlated and is shown below.

$$h_v = 652 \frac{G}{d_p}^{0.7} \quad (3.2.28)$$

As seen from Equation 3.2.28, the heat transfer between fluid and solid only depends on the particle diameter and flow rate. The study also reported that the inlet temperature had no effect on the heat transfer coefficient.

Chandra and Willits (1981) examine the experimental results of Löf and Hawley (1948) and note a variation of up to 50% for  $h_v$  with the inlet temperature, suggesting that the inlet temperature does have an effect on  $h_v$  and thus requires further investigation. An experimental study confirmed that the inlet temperature has a negligible effect on the  $h_v$  and that it was only dependent on the flow rate and particle size. The study indicated that the porosity had no significant effect on  $h_v$ . The modified Nusselt is used in this study and defined as

$$Nu_v = \frac{h_v d_p^2}{k_f} \quad (3.2.29)$$

The equation for  $Nu_v$  is correlated from experimental results.

$$Nu_v = 1.45 \frac{\rho V d_p^{0.7}}{\mu_f} \quad (3.2.30)$$

The correlation is valid for the following range  $100 \leq Re_p \leq 1000$ .

Coutier and Farber (1982) determine the volumetric heat transfer coefficient of a randomly packed rock bed by comparing experimental results to a theoretical model similar to the method used in the Löf and Hawley (1948) study. The difference, however, is that the theoretical model this study used, accounted for thermal losses and conduction within the bed, which is neglected in the Schumann model. The expression below was correlated from the data.

$$h_v = 700 \frac{G}{d_p} \quad (3.2.31)$$

This expression also shows that the heat transfer between the solids and fluid in a rock bed only depends on the flow rate and particle size. The correlation is valid for the following range  $100 \leq Re_p \leq 1000$ .

Singh *et al.* (2006) investigate the effect of system and operating parameters on,  $Nu_v$ , for a packed bed solar TES system. The study use five different particle shapes to determine the particle shape's effect. The equation below was correlated from the results.

$$Nu_v = 0.437 Re_p^{0.75} \psi^{3.35} \varepsilon^{-1.62} e^{29.03(\log \psi)^2} \quad (3.2.32)$$

The study determined that  $Nu_v$  is dependent on the flow rate, particle size and shape, and porosity. The particles sphericity and size ranged between  $0.55 \leq \psi \leq 1.0$  and  $125 \text{ mm} \leq d_p \leq 186 \text{ mm}$  respectively. The Reynolds number approximately ranged between  $1047 \leq Re_p \leq 2674$ .

Wakoa *et al.* (1979) correct published heat transfer data for packed beds from numerous sources, by including the axial fluid thermal dispersion. Equation 3.2.33

shows the Nusselt number from the study. The expression also shows that the heat transfer between the solids and fluid in a rock bed only depends on the flow rate and particle size, the expression is shown below.

$$Nu = 2 + 1.1Pr^{1/3}Re_p^{0.6} \quad (3.2.33)$$

The corrected data was correlated and valid for  $15 \leq Re_p \leq 8500$ .

Nuclear Safety Standards Commission (KTA) (1983) presents an equation for the heat transfer from uniform sized spherical particles in a packed bed to a gas flowing through it. The Nusselt number is calculated by Equation 3.2.34

$$Nu = 1.27 \frac{Pr^{1/3}}{\epsilon^{1.18}} Re_p^{0.36} + 0.33 \frac{Pr^{1/2}}{\epsilon^{1.07}} Re_p^{0.86} = 70.05 \quad (3.2.34)$$

This equation applies to the following range of bed parameters,  $100 < Re_p < 100000$ ,  $0.36 < \epsilon < 0.42$ ,  $D/d_p > 20$  and  $H > 5d_p$

### 3.3 CFD

Computational power in the last few years has increased enough that it is now possible to numerically solve the flow, mass and energy balance of complex 3-D geometries such as a packed bed using CFD. Commercial CFD codes consist of three main elements, namely a pre-processor, a solver and a post-processor.

The pre-processor element involves all the necessary steps to input a flow problem into a CFD program. These steps define the geometry (computational domain) of the problem, subdivided the geometry into a large number of small control volumes called cells, select physical and chemical phenomena that need to be modelled, define fluid properties and specify boundary conditions. The velocity, pressure, temperature, fluid density and so on (flow problem's solution) are defined at nodes on the sides of each cell. The accuracy of the flow problem solution is dependant on the number of cells within the computational domain. A larger number of cells for a given geometry, results in a more accurate solution, but it also increases the computational cost. Therefore, a mesh must be carefully developed to obtain an accurate solution without being too computationally expensive. Usually a non-uniform mesh is used to create an optimal mesh for a problem by making the mesh finer in regions where large variations occur and coarser in regions where relatively little change takes place from point to point (Versteeg and Malalasekera, 2007).

The solver element is where a solution to the flow problem is generated by solving the governing equations iteratively. The steps involved in this element are the integration of the governing equations, discretisation and use of an iterative method to solve the algebraic equations. The governing equations are usually the continuity, Navier-Stokes and energy equations, and these are shown below in Equations 3.3.1, 3.3.2 and 3.3.3 respectively (Versteeg and Malalasekera, 2007).

The relevant RANS turbulence models are described in Appendix B.

$$\frac{\partial \rho}{\partial t} + \text{div}(\rho \mathbf{u}) = 0 \quad (3.3.1)$$

$$\frac{\partial(\rho u)}{\partial t} + \text{div}(\rho u \mathbf{u}) = -\frac{\partial P}{\partial x} + \text{div}(\mu \text{ grad } u) + S_{m_x} \quad (3.3.2a)$$

$$\frac{\partial(\rho v)}{\partial t} + \text{div}(\rho v \mathbf{u}) = -\frac{\partial P}{\partial y} + \text{div}(\mu \text{ grad } v) + S_{m_y} \quad (3.3.2b)$$

$$\frac{\partial(\rho w)}{\partial t} + \text{div}(\rho w \mathbf{u}) = -\frac{\partial P}{\partial z} + \text{div}(\mu \text{ grad } w) + S_{m_z} \quad (3.3.2c)$$

$$\frac{\partial(\rho i)}{\partial t} + \text{div}(\rho i \mathbf{u}) = -P \text{ div } \mathbf{u} + \text{div}(k \text{ grad } T) + \phi + S_{m_i} \quad (3.3.3)$$

where  $\text{div } \mathbf{u} = \frac{\partial u}{\partial x} + \frac{\partial v}{\partial y} + \frac{\partial w}{\partial z}$ . The dissipation function that describe the effects of the viscous stresses in the energy equation, which are shown to be equal to Equation 3.3.4.

$$\phi = \mu \left\{ \left[ \left( \frac{\partial u}{\partial x} \right)^2 + \left( \frac{\partial v}{\partial y} \right)^2 + \left( \frac{\partial w}{\partial z} \right)^2 \right] + \left( \frac{\partial u}{\partial y} + \frac{\partial v}{\partial x} \right)^2 + \left( \frac{\partial u}{\partial z} + \frac{\partial w}{\partial x} \right)^2 + \left( \frac{\partial v}{\partial z} + \frac{\partial w}{\partial y} \right)^2 \right\} - \frac{2}{3} \mu (\text{div } \mathbf{u})^2 \quad (3.3.4)$$

The governing equations are integrated over the control volume and approximation techniques (discretisation) are used to convert them to an exact form where conservation of the relevant properties is expressed for each finite cell. An example of such techniques is the upwind differences scheme, which obeys the transportiveness requirement by assuming that the relevant flow variables of the upstream face of a cell are equal to that of the upstream node point. It also satisfies the boundedness and conservativeness fundamental properties of discretisation schemes. To minimize numerical errors, higher-order discretisation schemes are used, such as second-order and third-order schemes. The discretisation errors are reduced by involving more points and in so doing bring a wider influence. The resulting algebraic equations are non-linear due to the complex physical phenomena they represent, and they are solved using numerical methods (Versteeg and Malalasekera, 2007). Refer to Section 3.3.1 for more detail regarding these numerical methods.

The post-processing element is where the solution can be evaluated. Commercial CFD packages are equipped with powerful and versatile visualization tools that can include vector and contour plots, particle tracking and more. The visualization tools clearly display the solution of the flow problem, which enables non-specialists to understand the data (Versteeg and Malalasekera, 2007).

### 3.3.1 Solvers

ANSYS FLUENT provides two iterative methods to solve the algebraic equations: the pressure-based and the density-based solver. The pressure based solver was developed for low-speed incompressible flows. The density-based solver was developed for high speed compressible flows. Nevertheless, they have recently been extended and improved to operate for a wide range of flows. Both methods use the momentum equation to determine the velocity field. The pressure-based solver determines the pressure field from a pressure or pressure correction equation that is determined by altering the continuity and momentum equations. The density-based solver uses the continuity equation to determine the density field and the equations of state to determine the pressure field (Fluent, 2011*a*). Flow through a packed bed is kept at a relatively low speed in order to minimize the pressure drop; therefore this study will focus on the pressure-based solver approach.

Two pressure-based algorithms are available in ANSYS FLUENT: the segregated algorithm and the coupled algorithm. The segregated algorithm is more memory efficient because the governing equations are decoupled and solved sequentially, meaning that the discretised equations only have to be stored one at a time. The segregated method, however, converges relatively slowly. The coupled algorithm converges relatively fast but uses 1.5-2 times more memory because more than one discretised equation has to be stored at the same time (Fluent, 2011*a*). Figure B.1 in Appendix B, graphically shows the two algorithms.

A well-know segregated algorithm is the SIMPLE algorithm, where initially the pressure and velocity fields and other relevant flow variables are guessed. The guessed pressure field is used to solve the momentum equations and a pressure correction equation, which is deduced from the continuity equation; the pressure and velocity fields are then corrected from these results. The corrected pressure and velocity fields are then used to solve all the other transport equations (e.g. Energy,  $k$ ,  $\epsilon$ ). The results are then tested for convergence; if they converge the solution is stopped, otherwise the steps are repeated until the solution converges (Versteeg and Malalasekera, 2007).

### 3.3.2 Porous media condition

The porous media condition in ANSYS FLUENT 14.0 can be used to model the flow through a variety of applications, which include packed bed, filter paper, perforated plates and tube bundles. The porous media condition is applied to a cell zone. The model applies the porous media approach and physical laws to the continuity, momentum, energy and other scalar equations. The pressure drop and heat transfer is calculated according to the user inputs given (Fluent, 2011*b*).

To add to the pressure gradient in the porous cells, a simple momentum sink that results from two terms is added to the momentum equations, as seen in

Equation 3.3.2. The first term accounts for the viscous losses and the second term for the inertial losses. The source term is shown below in Equation 3.3.5 (Fluent, 2011*b*).

$$S_{M_i} = - \left( \sum_{j=1}^3 D_{ij} \mu u_j + \sum_{j=1}^3 C_{ij} \frac{1}{2} \rho |u| u_i \right) \quad (3.3.5)$$

where  $D$  and  $C$  are the diagonal matrix for the permeability and inertial resistance factor with  $1/\alpha$  and  $C_2$  on the diagonals respectively. The magnitude of the velocity is represented by  $|u|$ . As seen in Equation 3.3.5, the source term creates a pressure drop that is proportional to the velocity or velocity squared in the cell. The first term is Darcy's Law and is valid in laminar flow regime. The pressure drop is proportional to the velocity. The inertial resistance factor provides a correction for inertial losses at higher flow velocities. The coefficient  $C_2$  can be viewed as a loss coefficient per unit length along the flow direction, which allows the pressure drop to be viewed as a function of dynamic head. Equation 3.3.6 shows the simple form of the source term if the porous media is homogenous Fluent (2011*b*).

$$S_{M_i} = - \left( \frac{\mu}{\alpha} u_i + C_2 \frac{1}{2} \rho |u| u_i \right) \quad (3.3.6)$$

To ensure continuity of the velocity vectors in the porous media, the porous condition uses a superficial velocity based on the volume flow rate. This superficial velocity formulation does not take into account the porosity when calculating the convection and diffusion terms of the transport equation. This limits the accuracy of the porous model for cases where the velocity values and gradients are important. However, ANSYS FLUENT 14.0 does allow the user to select an option where the physical velocity is modelled in the porous media and where the porosity does appear in the transport equations Fluent (2011*b*). The physical velocity in the governing equations can be represented by

$$U_{\text{superficial}} = \varepsilon U_{\text{physical}} \quad (3.3.7)$$

The porous media condition also by default assumes that the porosity in the media is isotropic. A user defined function (UDF) can be used to specify a porosity that varies with space when assuming thermal equilibrium.

When modelling heat transfer in a porous media, the porous media model can assume thermal equilibrium or non-thermal equilibrium. Only the conduction and transient terms of the energy equation are modified for the porous media model. The energy equation for thermal equilibrium is given in Equation 3.3.8. This equation assumes that there is no heat transfer between fluid and solid ( $T_f = T_s = T$ ).

$$\frac{\partial}{\partial t} [\varepsilon \rho_f i_f + (1 - \varepsilon) \rho_s i_s] + \text{div}(\varepsilon \rho_f i_f \mathbf{u}) = P \text{div} \mathbf{u} + \text{div}(k_{\text{eff}} \text{grad} T) + \phi + S_{m_f}^i \quad (3.3.8)$$

When the non-thermal equilibrium option is enabled a dual cell approach is used by FLUENT where a new cell zone is created that is identical to the porous cell zone and positioned exactly in the same space. Now there exists two cells: one solid and one fluid. The solid zone only considers heat transfer from the fluid. The energy equation for the fluid and solid regions are solved separately. The heat transfer between these two cells are represented by  $h_v(T_f - T_s)$  and  $h_v(T_s - T_f)$ . The energy equations are shown in Equations 3.3.9 and 3.3.10.

$$\frac{\partial}{\partial t}(\varepsilon \rho_f i_f) + \text{div}(\varepsilon \rho_f i_f \mathbf{u}) = P \text{div} \mathbf{u} + \text{div}(\varepsilon k_f \text{grad } T_f) + \phi + S_{m_f}^i + h_{fs} A_{fs}(T_f - T_s) \quad (3.3.9)$$

$$\frac{\partial}{\partial t}[(1 - \varepsilon) \rho_s i_s] = \text{div}[(1 - \varepsilon) k_s \text{grad } T_s] + S_{m_s}^i + h_{fs} A_{fs}(T_s - T_f) \quad (3.3.10)$$

When modelling turbulence, the standard transport equations ( $k$ ,  $\varepsilon$ ,  $\omega$ , etc.) are solved for the porous media. The turbulence in the media neglects any effect the porous media might have on the turbulence generation or dissipation rates. This assumption might be reasonable for porous media where the permeability is relatively larger and the geometric scale of the media does not interact with the scale of the turbulent eddies. FLUENT also allows the turbulence to be suppressed in the porous cell zone.

The effect that the porosity has on the time-derivative term of all scalar transport equations and the continuity equation is accounted for when modelling a transient problem. The time-derivative term is transformed as shown

$$\frac{\partial}{\partial t}(\varepsilon \rho \gamma) \quad (3.3.11)$$

where  $\gamma$  is an arbitrary scalar.

### 3.4 Conclusion

The structure of the packed bed is shown in this chapter to be dependent on the bed height and width. If the bed width is too narrow relative to the particle diameter, the wall will have a significant effect on the flow field. An air-rock bed TES system will have a very large aspect ratio ( $D/d_p > 30$ ), and therefore it is not necessary to model the flow field near the wall with the CFD model in this study. Unfortunately, computation power limitations do not allow us to model beds with aspect ratios larger than 30 with discrete CFD models. An alternative, more computationally economical method has to be used to predict the flow through the central bulk packing. The bed height must also be equal or larger than 10 particle diameters to minimize the effect of axial porosity variation. The following section discusses the numerical model setups.

## 4. Numerical model

This chapter describes the numerical method used in this study to model flow and heat transfer through air-rock bed TES systems. Figure 4.1 shows a flow diagram of the numerical method and illustrates the link between the discrete and porous CFD models.

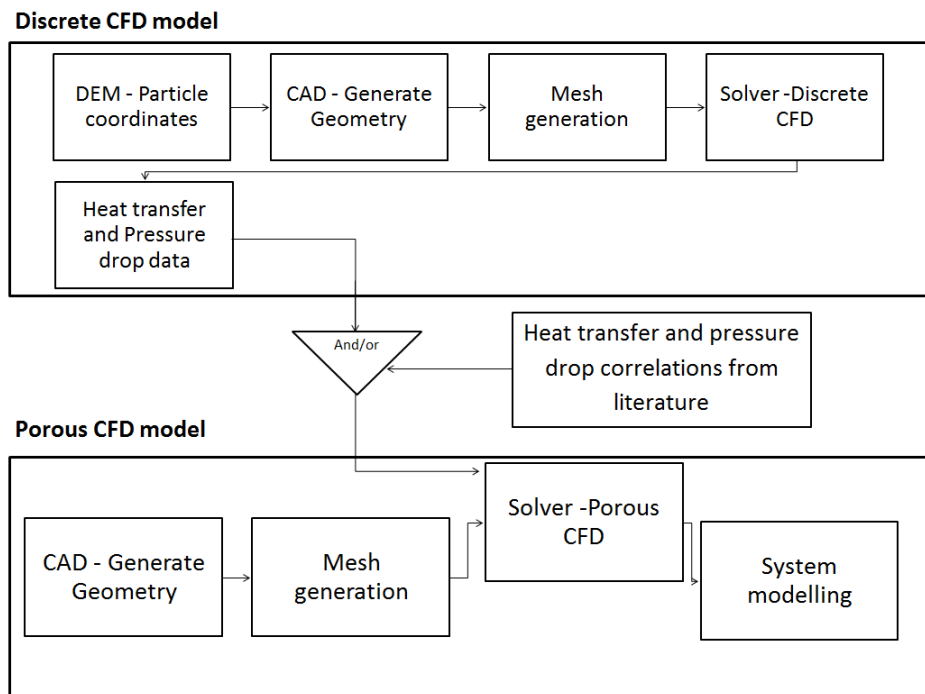


Figure 4.1: Numerical method process

The first step for the discrete CFD model was to create the packed bed geometry. The coordinates of the particles in the bed were generated by DEM. Once the coordinates are known, a CAD software package can be used to generate the geometry. A so-called "negative" of the packed bed geometry was created, which resulted in the bed's structure through which the fluid flowed. The next step was to divide the pore structure into small control volumes with a mesh generation software package to create the computational domain. This computational domain was then imported into a CFD solver, which solves the relevant transport

equations in order to predict the flow field through the bed and/or the heat transfer between the fluid and particle surface.

Pressure drop and heat transfer data from literature were used to setup the porous CFD model. The discrete CFD simulation flow and heat transfer data of the packed bed can also be used in the porous model. However, before the data is used in the porous CFD model the geometry first needs to be created. The geometry was created using a CAD software package. The geometry was then divided up into small control volumes again using a mesh generation software tool. A CFD solver imports the computational domain and solves the relevant transport equations to model a TES system.

## 4.1 Discrete CFD model

### 4.1.1 Generating a CAD model

The steps to generate the packed bed geometries are illustrated in Figure 4.2. The packed bed geometry was generated using DEM. A program written in Scilab-5.4.0 (Scilab Enterprises, 2012) determines which spheres are in contact with each other or if the distance between two spheres is below the minimum allowable distance. A program written in Microsoft Visual Basic (Microsoft Corporation, 2010) reads the coordinates of the spheres and their contact points and instructs Autodesk Inventor (Autodesk Inc., 2012) to create a particle at each of the given coordinates and apply the chosen contact treatment method. The program can either use the bridge or cap methods

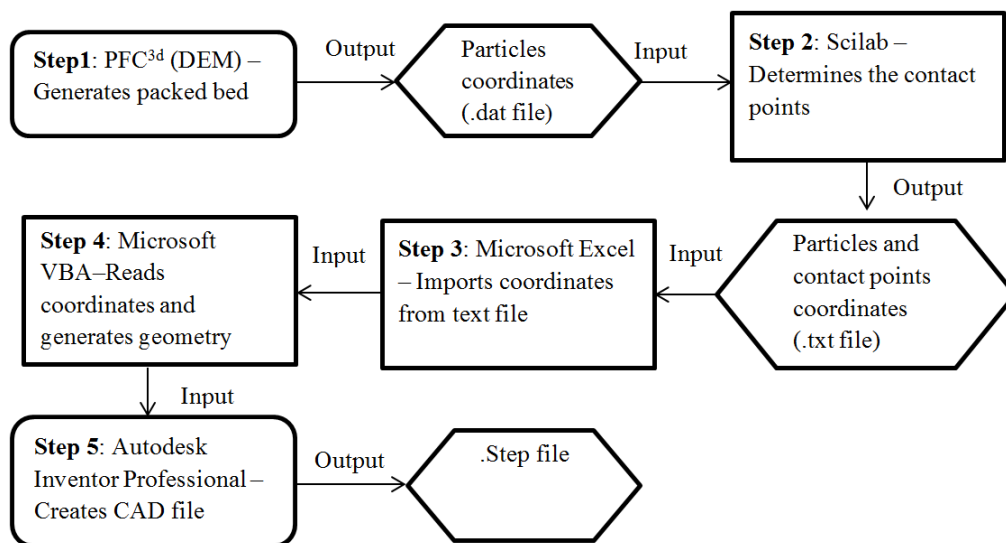


Figure 4.2: Geometry generation flow chart

### 4.1.2 Contact treatment

The contact treatment method selected to eliminate contact points and narrow gaps was the inter-particle bridge method. The selected diameter range of the bridge and the minimum allowable gap used in the simulations is shown in Table 4.1, where  $d_b$  is the diameter of the cylindrical bridge and  $H_{\text{sph}}$  is the distance between two particles surfaces.

Table 4.1: Size range for bridge method

Bridge diameter	$0.2 \leq d_b / d_p \leq 0.3$
Minimum allowable gap	$0.01 d_p \leq H_{\text{sph}} \leq 0.02 d_p$

### 4.1.3 Channelling

To minimize wall channelling the particles in contact with the wall were sectioned as shown in Figure 4.3. This process effectively roughens the wall and reduces the effect of wall channelling. This method is similar to the one used in the experimental works of Malling and Thodos (1967) and the numerical works of Soleymani *et al.* (2007) and Jafari *et al.* (2008). For beds containing spherical particles, the "outside" particles were sectioned at  $0.5r_p$  with  $r_p$  equal to the smallest sphere in the bed's radius. For irregular particles, a slightly different method was used, where the irregular particles were dropped into a ring of structurally packed spheres. The diameter of the spheres in the ring was roughly equal to the size of the irregular particles (base on equivalent spherical volume). The ring of structurally packed spheres was sectioned at  $0.67d_p$  (see figure 4.4).

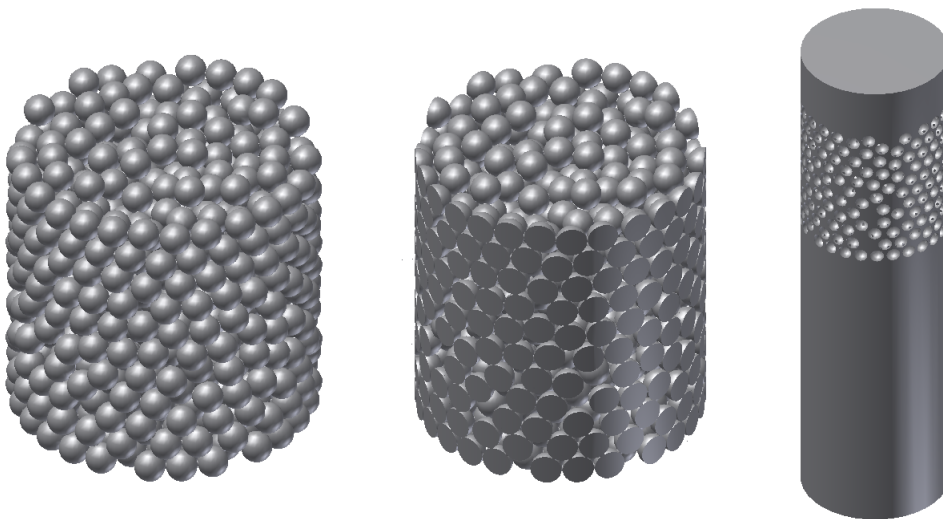


Figure 4.3: Spherical particles wall channelling modification

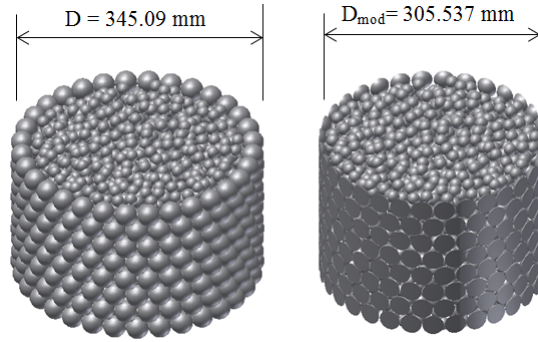


Figure 4.4: Irregular particles wall channelling modification

#### 4.1.4 Mesh generation

The volume mesh used to create the computational domain was generated from the surface mesh. The volume mesh consisted of a prism layer and the tetrahedral volume mesh region. The prism layer region was used in the near wall region of the particle surface and made up of two prism layers. A previous study reviewed by Theron (2011) suggests that two prism layers results in the best ratio between the number of cells and skewed volume cells. Eppinger *et al.* (2010) also used two prism layers around the wall surfaces with a total thickness of  $0.03d_p$ . Dixon *et al.* (2011) shows that two prism layers is sufficient enough and recommends that it should cover roughly 60% of the theoretical boundary layer (Equation 2.4.1). In this study a similar mesh generation strategy, suggested by Dixon *et al.* (2011), was followed as far as it was practically possible. The first layer thickness was estimated from the theoretical boundary layer, and the surface mesh was set as fine as practically possible to prevent the aspect ratio of the first prism layer from being too high. The parameters used in this study to generate the mesh are given in Table 4.2.

Table 4.2: Surface and volume mesh parameters

Surface mesh triangle edge size	$d_p/15 - d_p/25$
Surface growth rate	1.2
Number of prism layers	2
First layer thickness	$1 - 3 \times \delta_{BL}/10$
Total thickness	$\pm 6 \times \delta_{BL}/10$
Tetrahedral volume mesh growth rate	1.4

The prism layers and volume mesh around the contact region are shown in Figure 4.5 for three different surface mesh sizes ( $d_p/12$ ,  $d_p/15$  and  $d_p/20$ ) and a first prism layer height of  $3 \times \delta_{BL}/10$ . As the figure makes evident, as the surface mesh sizes decreases the volume mesh becomes finer. It was also noticed from

the figures that the aspect ratios of the prism layers decrease with decreased surface mesh sizes.

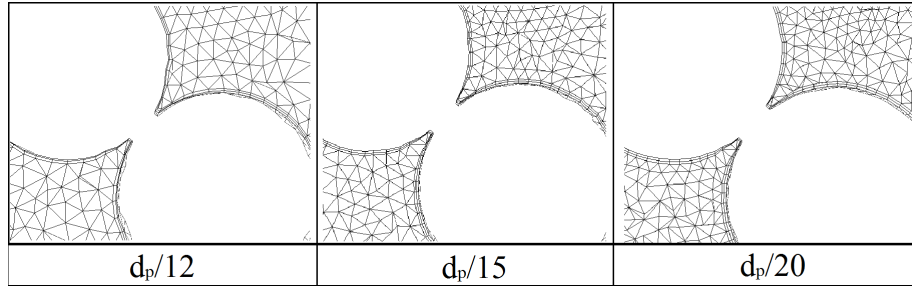


Figure 4.5: Fluid cells around contact region (first prism layer =  $3 \times \delta_{BL}/10$ )

Because of the complex geometry, it is difficult to achieve a very high quality mesh that is also economical. The quality measurement of the mesh is skewness and the maximum allowed skewness for the surface and volume mesh is 0.7 and 0.95 respective. This is acceptable mesh criterion.

#### 4.1.5 Turbulence modelling

The RANS turbulence models were used in this study. Following the work of Guardo *et al.* (2005) and Dixon *et al.* (2011), the Spalart-Allmaras one-equation model and the shear stress transport (SST)  $k - \omega$  two-equation model is recommended. The realizable  $k - \epsilon$  with the Enhanced Wall function is also investigated. The turbulence models are used for  $Re_p \geq 100$ , due to the uncertainty of modelling transitional flow in packed beds.

The realizable  $k - \epsilon$  performs well for flow containing strong streamline curvature, vortices and rotation, all of which is expected in packed beds. The Enhanced Wall Treatment (EWT) is a  $y^+$  insensitive wall treatment. All the solution variables from the viscous sublayer formulation  $u^+ = y^+$ , are automatically blended depending on  $y^+$ , to the corresponding logarithmic layer values  $u^+ = \frac{1}{\kappa} \ln(Ey^+)$ . The blending is calibrated to cover intermediate  $y^+$  values in the buffer layer  $1 \leq y^+ \leq 30$  (Fluent, 2011a). It is difficult to maintain a mesh with a constant  $y^+$  value in a packed bed, therefore a wall treatment which is  $y^+$  insensitive necessary.

The Spalart-Allmaras model is a one-equation turbulence model that has shown good results for boundary layers subjected to adverse pressure gradients, but it is not well calibrated for free shear flows (Fluent, 2011a). Guardo *et al.* (2005) reports that this model performed well for flow through packed beds. This was attributed to the coupling between the wall function and damping function for near wall treatment. Because this model only use one-equation it is a little more computationally economical which can be an advantage for large packed beds, requiring large mesh sizes.

The SST  $k-\omega$  model transforms the  $k-\epsilon$  model into a  $k-\omega$  model in the near wall region and uses the standard  $k-\epsilon$  model in the fully turbulent region far from the wall (Versteeg and Malalasekera, 2007). The model combines the ability of the standard  $k-\epsilon$  to model the free stream flow, with the ability of the  $k-\omega$  model to model turbulent flow in the near wall region and can be integrated to the wall.

#### 4.1.6 Boundaries and material properties

The discrete CFD model's boundaries are discussed in Appendix C. Air is used as the working fluid, see Appendix E.

## 4.2 Porous CFD model

### 4.2.1 CAD model

The different parts of the model are shown in Figure 4.6, namely the inlet plenum, outlet plenum and the porous media. The porous model can increase in complexity by including multiple inlets and outlets, an internal channel network or any other geometric design requirement that the TES system design specifies.

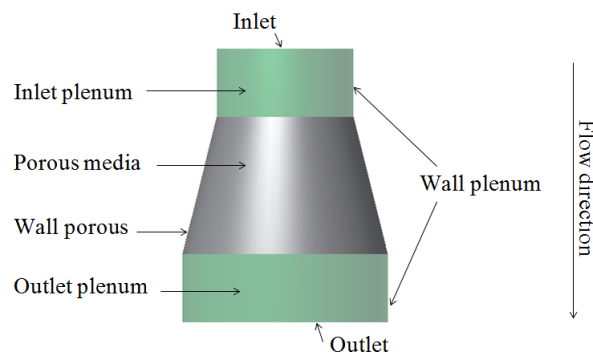


Figure 4.6: Porous media geometry and boundary

### 4.2.2 Mesh generation

The type of mesh used depends on the complexity of the model. With ANSYS Meshing 14.0 either a tetrahedral, hex, cutcell or hybrid mesh can be used. The hybrid consists of a tetrahedral and hex mesh. This meshing method can be used when the geometry of certain parts of the TES model are very complex and is best resolved with a tetrahedral mesh, as the parts that have simple geometric features use the more economical hex mesh. The hybrid method is illustrated in Figure 4.7.

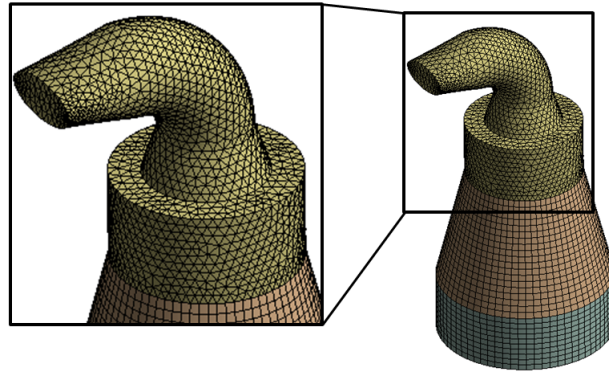


Figure 4.7: Hybrid mesh

### 4.2.3 Turbulence modelling

The turbulence transport equations were suppressed in the porous media zone. As mentioned in section 3.3.2, the effect of the actual porous media structure, modelled on the turbulence generation or dissipation rates was neglected. The effect of turbulence on the flow and heat transfer of the bed was captured in the pressure drop and heat transfer coefficient correlations, which were obtained from either discrete CFD models or experimental measurements. In the fluid zones of the model, the turbulence was modelled with the realizable  $k-\epsilon$  models, and the enhanced wall function was used to model the near wall flow. The  $k-\epsilon$  models performs well for confined flows. The fluid zones of the porous media model were most likely to model confined flow for inlet ducting and/or plenums. The realizable  $k-\epsilon$  model was selected because it addresses short comings of the previous  $k-\epsilon$  model. The realizable  $k-\epsilon$  model demonstrates better results for flow with strong stream line curvature, vortices and rotation (Fluent, 2011*a*).

### 4.2.4 Boundaries and material properties

The porous CFD model's boundaries are discussed in Appendix C. Air is used as the working fluid, see Appendix E. The material properties for the rock in the porous model are from Tables E.1 and E.2, unless otherwise specified. Other material properties such as metals and insulation for TES container walls and ducts are specified.

## 4.3 Conclusion

Methods were established in this section to create functional discrete and porous CFD models of packed beds. The accuracy and sensitivity of the various approximations and choice of items such as turbulence model, wall channelling modification and appropriate mesh size need to be revisited based on validation. The following chapters are dedicated to validating the models.

## 5. Discrete results and validation

This chapter discusses the discrete CFD model's results. The flow and heat transfer was simulated through two differently packed beds, namely spherical and irregular.

### 5.1 Discrete CFD model validation

A bed containing uniform spherical particles was used in this section to validate the methods used in this study and thus determine the pressure drop and heat transfer through packed beds. The effect of the wall channelling modification, turbulence model selection and mesh refinement study was done and validated against pressure drop and heat transfer correlations found in literature.

#### 5.1.1 Geometry

The uniform spherical packed bed geometry is shown in Figure 5.1; the bed contains 872 spheres. The dimensions of the bed before and after the modification are also shown in the figure. The wall channelling modification effectively represents a bed with a very large aspect ratio. The porosity of the bed before and after the wall channelling modification is given in Table 5.1. The table shows that the bed porosity agreed well with Zho and Yu (1995) correlations for a loose packing and also fairly well with Dixon (1988) correlation. These findings suggest that the packed bed geometry represents a loose packing.

#### 5.1.2 Computational domain

The boundaries for the flow and heat transfer simulation were set up as explained in section C.1.1. The simulation was done until the convergence of all residuals was below  $5 \times 10^{-4}$  and the pressure drop and temperature difference measured over the bed converged. The under-relaxation factors for the momentum, energy and turbulence equations, was changed from default to 0.05, 0.2 and 0.2 respectively. The under-relaxation factors for the momentum equations was increased to 0.1 during the simulations. The under-relaxation factors were kept fairly low to ensure convergence. This resulted in a slow convergence and between 10 000 and 15 000 iterations was necessary.

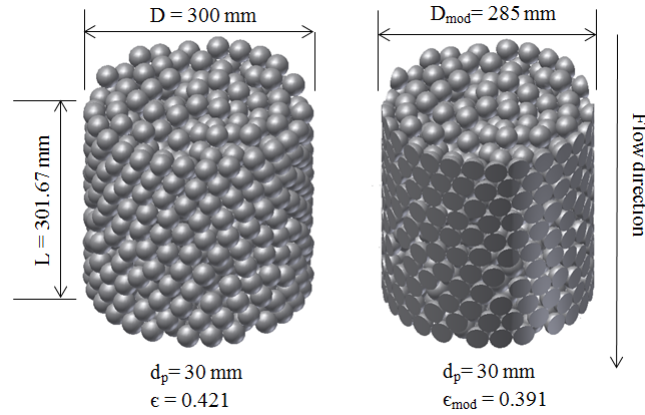


Figure 5.1: Sphere bed with and without channelling modification

Table 5.1: Sphere bed porosity

<b>Aspect ratio = 10</b>		Porosity []	Error [%]
Normal bed		0.421	–
Dixon (1988) (eq. 3.1.2)		0.409	2.9%
Zho and Yu (1995) - Loose packing (eq. 3.1.3)		0.419	0.45%
Zho and Yu (1995)- Dense packing (eq. 3.1.4)		0.379	11%
<b>Aspect ratio = ∞</b>		Porosity []	Error [%]
Modified bed		0.391	–
Dixon (1988) (eq. 3.1.2)		0.40	2.25%
Zho and Yu (1995) - Loose packing (eq. 3.1.3)		0.40	2.25%
Zho and Yu (1995)- Dense packing (eq. 3.1.4)		0.372	5.1%

The simulations was done on the University of Stellenbosch high-performance computing cluster. The cluster has 168 cores @2.83Ghz and 336 GB of RAM (Venter). The simulations used between 8 and 16 cores per simulation and took between 48 and 72 hours to run.

The locations where the pressure and temperatures were measured can be seen in Figure 5.2.

### 5.1.3 Turbulence model selection

The three different turbulence models compared in this section are the Spalart–Allmaras (S-A) turbulence model, the SST  $k - \omega$  turbulence model and the realizable  $k - \epsilon$  turbulence model with the enhanced wall treatment option enabled. These three turbulence models were compared, for flow and heat transfer simulations at  $Re_p = 1000$ . The mesh size that was used was  $d_p/15$ . The pressure drop results were compared against the Allen (2010) and Nuclear Safety Standards Commission (KTA) (1981) correlations, and the heat transfer results were compared against the Wakoa (1979) and Nuclear Safety Standards Commission

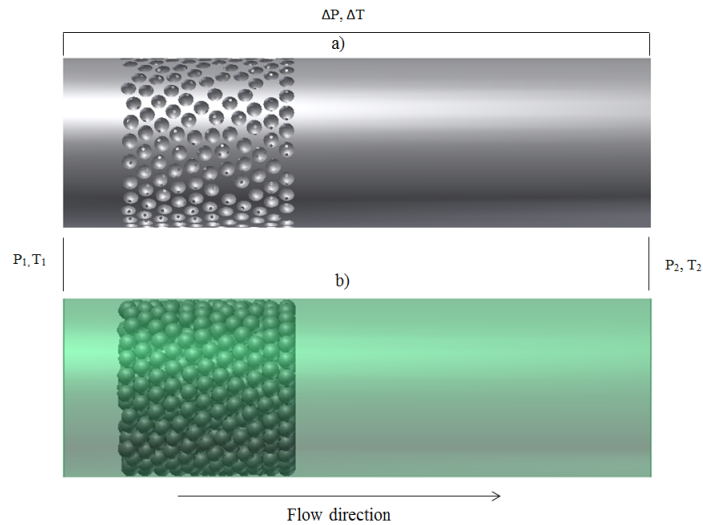


Figure 5.2: Computational domain with and without channelling modification

(KTA) (1983) correlations. The results are shown in Tables 5.2 and 5.3. The SST  $k - \omega$  model agrees the best with the pressure drop correlations followed closely by the S-A model and lastly by the realizable  $k - \epsilon$  model. The SST  $k - \omega$  model also agrees the best with heat transfer correlations. The S-A model gave the worst results of the three but the results are still in close agreement with the correlations. The results indicate that all three turbulence models agree well with the pressure drop and Nusselt number correlations. Although all three turbulence models were fairly in close agreement with each other, the SST  $k - \omega$  turbulence model was chosen to model turbulence. This model has shown good behaviour with adverse pressure gradients and separating flows (Versteeg and Malalasekera, 2007), which can be expected in flows through packed beds.

Table 5.2: Turbulence model comparison

<i>Pressure drop</i>			
Turbulence model	dP [Pa]	% err Allen	% err KTA
Correlation - Allen	51.03	-	-
Correlation - KTA	50.73	-	-
S-A	54.6	7.0%	7.63%
SST $k - \omega$	54.42	6.64%	7.27%
realizable $k - \epsilon$	56.67	11.05%	11.71%

#### 5.1.4 Wall channelling modification

The effect of the wall channelling modification on the pressure drop and heat transfer is presented in this section. Figure 5.3 shows the results from the pressure drop simulation in the form of the dimensionless friction factor versus the

Table 5.3: Turbulence model comparison

<i>Heat transfer</i>			
Turbulence model	Nu []	% err Wakoa	% err KTA
Correlation - Wakoa	63.9	-	-
Correlation - KTA	70.1	-	-
S-A	53.3	16.59%	23.99%
SST $k - \omega$	54.3	15.02%	22.54%
realizable $k - \epsilon$	53.9	15.57%	23.06%

Reynolds number ( $Re_2$ ), as defined by Allen *et al.* (2012). The simulations were done for  $1 \leq Re_p \leq 1000$ . The mesh size that was used was  $d_p/15$ . The results compare well with the Nuclear Safety Standards Commission (KTA) (1981) and Allen *et al.* (2012) correlations but start to deviate from the Ergun equation at  $Re_2$ , higher than approximately 100. The average deviation given in percentage is shown in Table 5.4.

Table 5.4: Wall channelling modification effect

<i>Pressure drop</i>			
Average deviation:	% Ergun	% Allen	% KTA
Without wall channelling modification	30.989%	4.85%	14.50%
With wall channelling modification	17.46%	7.36%	9.47%

At a low Reynolds number of about 1, the friction factor of the geometry without wall channelling modification is higher. This was expected because the surface area of the wall adds more viscous friction. At a higher Reynolds number of roughly 1000 the friction factor was lower for the geometry with the wall channelling modification, which was again expected due to the dominating inertial resistance and the relatively low viscous force at high Reynolds numbers. The channels provide a lower resistance path for the flow to pass through. The results show that the wall channelling modification made a small difference to the pressure drop results. In the laminar regime the wall channelling modification provides more accurate results, for the transitional regime the results were practically identical. In the turbulent regime the wall channelling modification is in closer agreement with the Nuclear Safety Standards Commission (KTA) (1981) correlation than the Allen *et al.* (2012) correlation, while the normal geometry agrees more closely with the Allen *et al.* (2012) correlation than the Nuclear Safety Standards Commission (KTA) (1981) correlation.

The heat transfer simulation results are shown in Figure 5.4 for the Nusselt versus the particle Reynolds number ( $Re_p$ ). The simulations are done for  $100 \leq Re_p \leq 4000$ . The heat transfer simulation was not done for  $Re_p = 1$ , due to the unlikelihood of a flow rate below  $Re_p = 100$  occurring in air-rock bed storage. The results clearly show that the wall channelling modification provides more

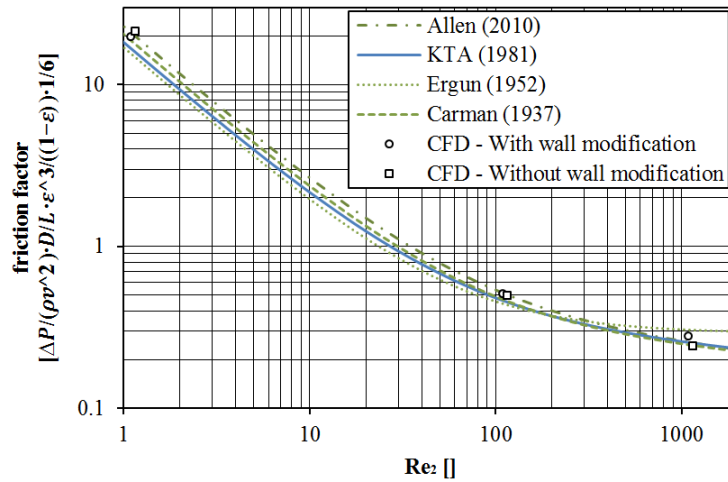


Figure 5.3: Wall channelling modification friction factor results

accurate results. The average deviation of the CFD results from the correlations is shown in Table 5.5

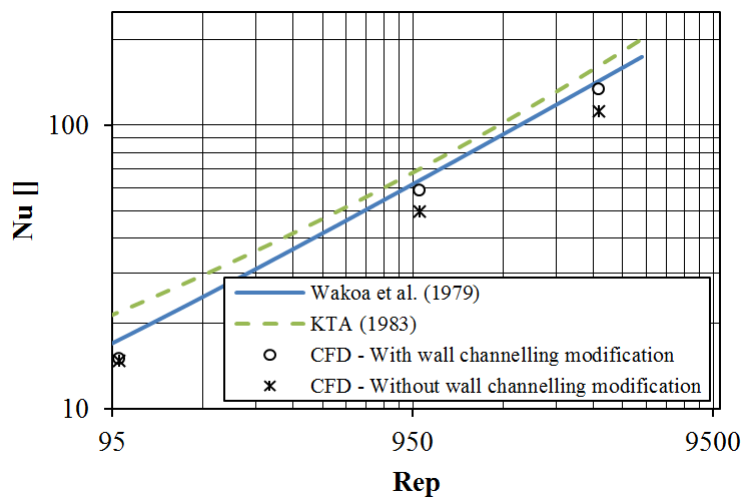


Figure 5.4: Wall channelling modification heat transfer results

Table 5.5: Wall channelling modification Nusselt number effect

<i>Heat transfer</i>		
Average deviation:	% Wakoa <i>et al.</i> (1979)	% KTA (1983)
Without wall channelling modification	20.3%	31.2%
With wall channelling modification	11.26%	22.3%

Figure 5.5 show the temperature profile precisely at the exit of the sphere beds with and without the wall channelling modification. The profile represents a sin-

gle line of measurements spanning over the cross section of the bed. From this figure it is seen that even at  $Re_p = 100$ , cold air still flows around the packed bed and that no cold air flows around the bed with the wall channelling modification. The difference between the beds' profile with and without the wall channelling modification becomes even greater with increasing Reynolds numbers. The maximum temperature difference for  $Re_p = 1000$  is 18.3 K and for  $Re_p = 4000$  is 47.5 K.

Figure 5.6 is a section through the packed bed that shows the temperature contours. At  $Re_p = 100$ , the difference between the bed with and without the wall channelling modification, is not significantly noticeable from the figure, but at higher  $Re_p$  the difference becomes a lot more obvious. At  $Re_p$  equal to 1000 and 4000 it is clear that in the bed without the wall channelling modification, a portion of the cold air was channeled around the packed bed through the wall channels resulting in impaired heat transfer. There was no sign of cold air escaping around the sides of the bed with the wall channelling modification, and the air appears to have flowed evenly through the packed bed.

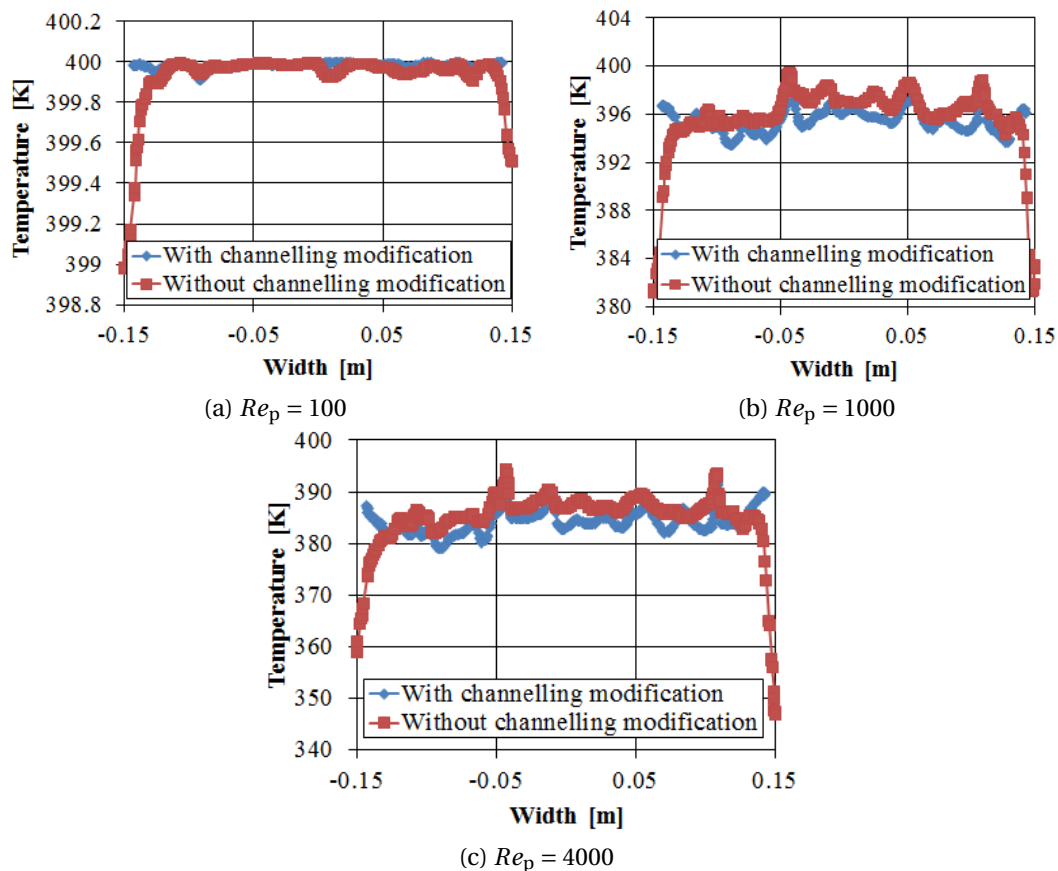


Figure 5.5: Outlet cross sectional temperature profile

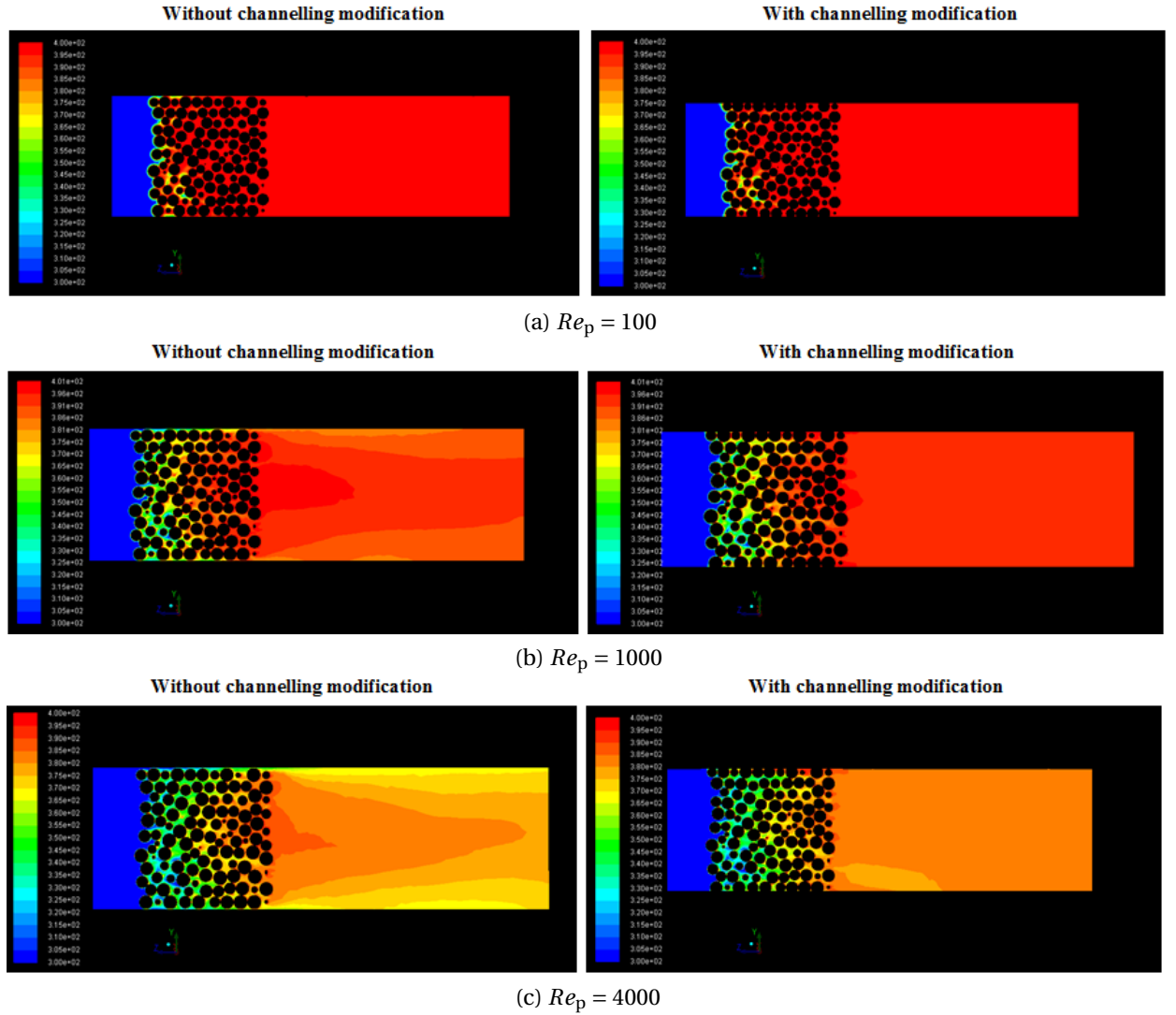


Figure 5.6: Temperature contours

### 5.1.5 Mesh refinement study

Three mesh sizes were tested. The three meshes were created with three different sized surface meshes of  $d_p/15$ ,  $d_p/20$  and  $d_p/25$ . The number of elements in each mesh and the results from the mesh sensitivity study are summarized in Table 5.6. A pressure and temperature result was computed for a theoretical mesh size of zero using Richardson extrapolation (NASA, 2008). Equation 5.1.1 was used

$$\lambda_{\infty} = \lambda_{\text{fine}} + \frac{\lambda_{\text{fine}} - \lambda_{\text{medium}}}{r_p - 1} \quad (5.1.1)$$

where,  $\lambda$ , was the parameter under investigation and  $r_p = N_{\text{fine}}/N_{\text{medium}}$  where  $N$  is the mesh size. The error was calculated from the following equation.

$$\text{error} = \left| \frac{\lambda_{\infty} - \lambda}{\lambda_{\infty}} \right| \quad (5.1.2)$$

Table 5.6: Mesh refinement

Mesh size	Number of cells	Pressure [ $Re_p = 1000$ ]		Outlet temperature [ $G = 0.7202 \text{ kg/s} \cdot \text{m}^2$ ]		
		Pressure [Pa]	Error	Temperature [K]	Nu[]	Error
$d_p/15$	7 666 611	54.42	5.47%	394.03	54.3	11.73%
$d_p/20$	13 493 530	55.89	3.75%	395.07	57.95	5.78%
$d_p/25$	21 948 827	56.83	2.13%	395.41	59.32	3.55%
$d_p/\infty$	$\infty$	58.07	–	395.95	61.5	–

The results indicate that the mesh size has a larger effect on heat transfer than the pressure drop. The mesh size in this study ranged between  $d_p/15$  and  $d_p/20$ .

Current computational power available to this study can solve meshes with sizes below  $d_p/25$  for a finite number of particles not exceeding much more than 2000 particles (depending on the mesh size). However, due to time constraints and the fact the mesh size between  $d_p/15$  and  $d_p/20$  gives adequate results. Mesh sizes in this study does not fall below  $d_p/20$  and the number of particles in a bed stayed below 2000 particles. This was to keep the mesh sizes within reasonable size limits at an acceptable level of accuracy.

## 5.2 Spherical particle packed bed results

The pressure drop and heat transfer results given in this section are done for the bed shown in Figure 5.1. The mesh size used in the simulations was  $d_p/20$ . The pressure drop simulations ranged between  $1 \leq Re_p \leq 32006$  and the heat transfer simulations between  $49.86 \leq Re_p \leq 27932.3$

In Figure 5.7 the pressure drop data is plotted for the friction factor as defined by Allen *et al.* (2012) versus  $Re_2$ . The CFD results agree well with the Ergun equation for Reynolds numbers below roughly 500 and start to deviate for higher Reynolds numbers. The findings are similar to what Allen *et al.* (2012) observed with their study's experimental measurements. The CFD results show good agreement with the Allen *et al.* (2012), Nuclear Safety Standards Commission (KTA) (1981) and Carman (1937) equations with average deviation of 9.42%, 10.34 and 9.90% respectively. The maximum deviations from the correlations are 16.21%, 18.54% and 15.31% respectively.

Between  $Re_2$  of 2000 and 3000 a discontinuity can be seen in the CFD results, which can be attributed to the fact that a new mesh with a smaller prism layer

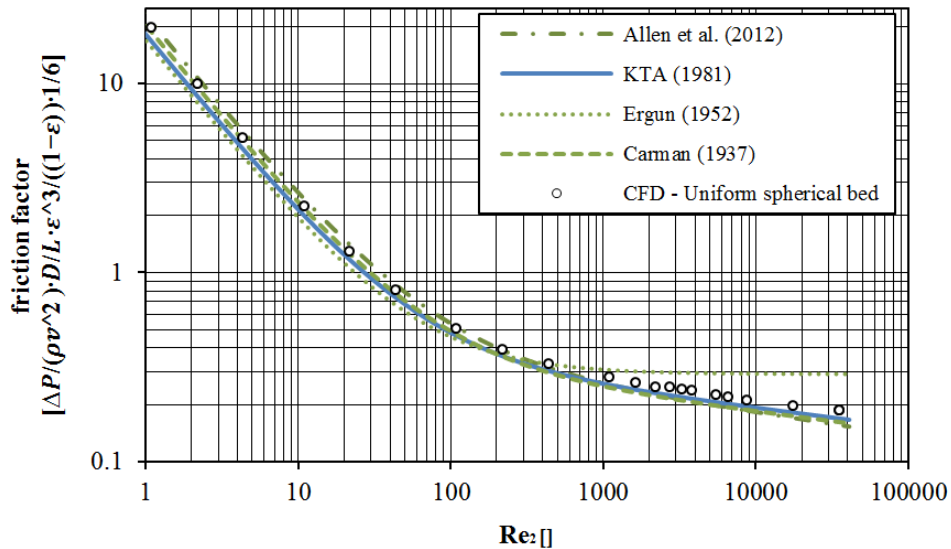


Figure 5.7: Spherical particle bed pressure drop results

was used for simulations above Reynolds numbers of 2000. The new mesh was used to keep the average  $y^+$  value below 2. In total, three meshes were used to obtain the results shown in the figure. The first mesh was used for  $1 \leq Re_p \leq 2000$ , the second mesh was used for  $2000 < Re_p \leq 8000$  and the third mesh was used for  $8000 \leq Re_p \leq 32006$ .

In Figure 5.8 the Nusselt number of the packed bed is plotted against the particle Reynolds number. The data was compared to the Wakao *et al.* (1979) and Nuclear Safety Standards Commission (KTA) (1983) correlations, which are specifically for spherical particles. The data agrees with the Wakao *et al.* (1979) and Nuclear Safety Standards Commission (KTA) (1983) correlations. At low Reynolds numbers below 1000 the predicted Nusselt number is more in agreement with the Wakao *et al.* (1979) correlation. At higher Reynolds numbers the CFD predicted Nusselt number compares better to the Nuclear Safety Standards Commission (KTA) (1983) correlation. The average deviation of the CFD results to the Wakao *et al.* (1979) correlation is 13.36% with the maximum deviation at  $Re_p=49.9$  of 25.8% for the range in which the correlation is valid ( $15 \leq Re_p \leq 8500$ ). The average deviation from the Nuclear Safety Standards Commission (KTA) (1983) correlation is 21.83% with a maximum deviation of 31.27% at  $Re_p=99.73$  for the range in which the correlation is valid ( $100 \leq Re_p \leq 100000$ ).

Three meshes were also used to obtain the results shown in Figure 5.8, to keep the average  $y^+$  value below 2. The first mesh was used for  $1 \leq Re_p \leq 2000$ , the second mesh were used for  $2000 < Re_p \leq 8000$  and the third mesh was used for  $8000 \leq Re_p \leq 27932.3$ . As the  $Re_p$  increase the prism layers size was decreased. A discontinuity can be seen at around  $Re_p$  equal to 2000, where the CFD results shows an under predicted result. The first mesh with the largest prism layer size is used and this indicates that the prism layer is not fine enough.

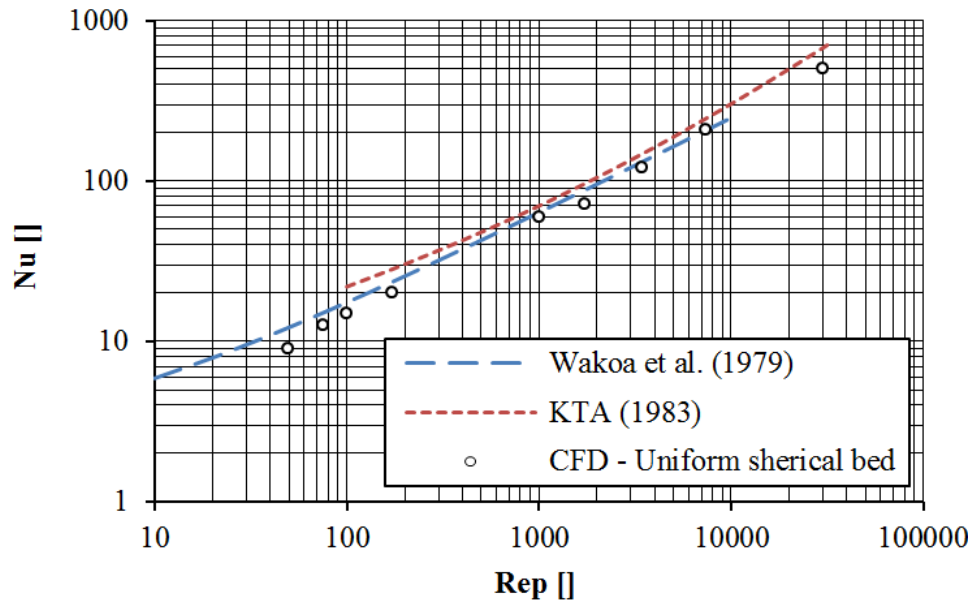


Figure 5.8: Spherical particle bed heat transfer results

### 5.3 Irregular particles packed bed results

This section presents the pressure drop data and heat transfer data from the irregular particle packed beds CFD simulations. These beds are described in detail in Appendix A. Table 5.7 gives a summary of the beds. Beds 1 through 4 refers to the 1) non-uniform spherical bed, 2) PES (Pyramid Elongated Spherical) bed, 3) pyramid bed and 4) elongated bed.

The particle size range given in the table was based on the equivalent spherical specific surface area of each type of particle in a given bed. The  $d_{p_{Sv}}$  denotes the average particle size of the bed based on the equivalent spherical specific surface area, and  $d_{p_v}$  indicates the average particle size based on the equivalent spherical volume. The sphericity of the elongated and pyramid particles was 0.8267 and 0.7564 respectively.

Table 5.7: Packed beds

	Particle size range [mm]	$d_{p_{Sv}}$ [mm]	$d_{p_v}$ [mm]	# of particles []	L [mm]	D [mm]	Porosity []
#1	15;20;30	26.57		1894	303.28	292.5	0.391
#2	22.7;24.8;30	25.929	30	751	279	305.537	0.443
#3	21.18	21.18	28	750	222.73	305.537	0.434
#4	23.147	23.147	28	750	230.95	305.537	0.439

### 5.3.1 Results

The pressure drop and heat transfer results for the irregular packed bed simulations are shown in Figures 5.9 and 5.10 respectively. The pressure drop results were done for  $Re_p$  of 1, 100 and 1000. The heat transfer simulations were done for  $Re_p$  of 83.81, 840.6, 1685 and 3378.

The beds containing the non-uniform spherical particles and elongated particles showed the highest friction factor in the laminar, transition and turbulent flow regimes of all the packed beds. The PES bed containing a mixture of spherical, elongated and pyramid particles showed a slightly higher friction factor but was close to the spherical beds friction factor, especially in the transition and turbulent flow regime. The bed containing the pyramid particles shows the lowest friction factor of all the packed beds. The higher friction factor of the non-

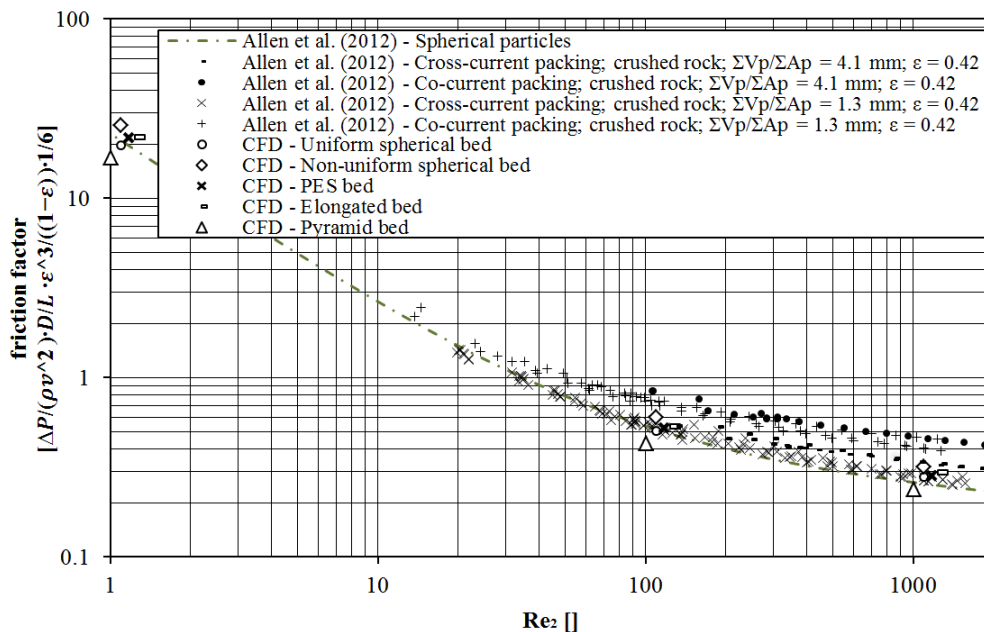


Figure 5.9: Irregular particle bed pressure drop results

uniform spherical bed is most likely due to the mixture of small and large particles causing a more tortuous flow through the bed and increasing the mean flow path length. The smaller particles fill the gap between the larger spheres causing the air-flow to flow around the smaller sphere where it could previously just have flown straight through that particular pore.

The similarity between the spherical particle bed and irregular particle bed is most likely due to the fact that the irregular particles were comprised of a clump of spheres. Although the shape of the irregular particles was different to that of a sphere, the particles were still well rounded off, not containing any sharp edges or blunt surfaces typically found on rock particles. In a rock bed the blunt particle surfaces and sharp edges can possibly cause separation and eddies to form

which results in higher form drag. Allen *et al.* (2012) demonstrates that the friction factor for flow through a co-current packed bed of rock particles is roughly 50% higher than for flow through a cross-current packed bed of rock particles. The study notes that the rocks in the bed tend to align with the largest surface area of the particles facing normal to the flow direction for co-current packing. The study proposes that the variation is due to a larger form drag from the co-current packing. The flow through the irregular particle bed in this study were all co-current packing, and the friction factor results clearly were not of similar magnitude. The results, however, from the non-uniform sphere, PES, and elongated beds showed fairly similar results to the cross-flow packing experimental measurements from Allen *et al.* (2012), when visually compared to the results. This would suggest that using the irregular particles fails to reproduce form drag due to variations in particle orientation, but it did seem to capture the more tortuous flow conditions found in rock beds. The packed bed containing the pyramid particles showed the lowest pressure drop of all the beds tested. This could possibly be due to the particular shape of the particle that may have created low resistance path ways through the bed.

The heat transfer results for the irregular packed bed are shown Figure 5.10. The results show closer agreement with the heat transfer correlations found in literature for beds containing rocks than for the correlation for beds containing spheres. There was a larger difference between spherical and irregular shape particles at  $Re_p$  below a 1000. At  $Re_p$  larger than a 1000 the Nusselt numbers, were fairly similar to each other.

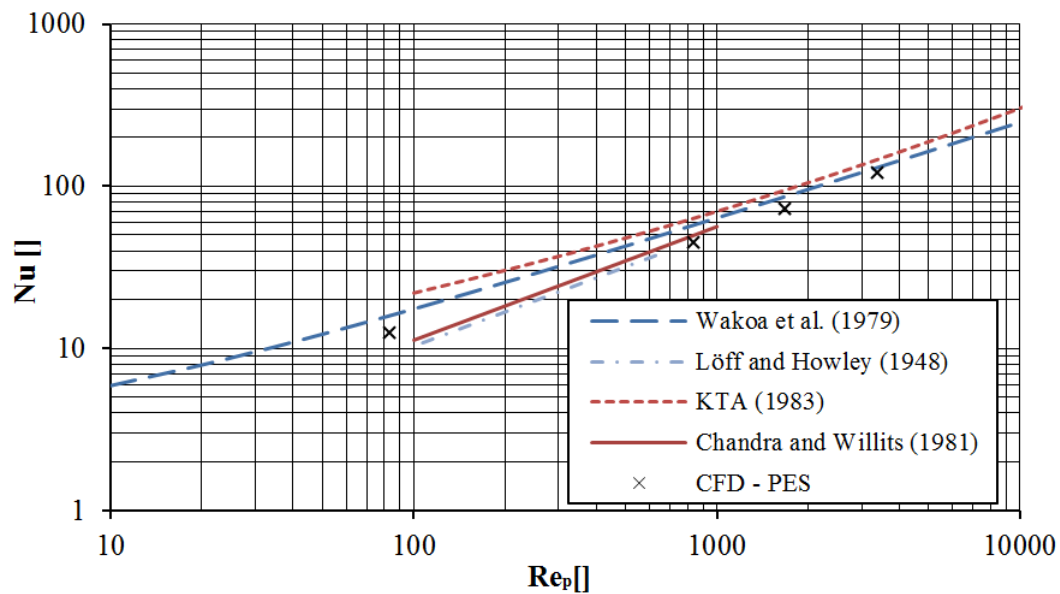


Figure 5.10: Irregular particle bed heat transfer results

## 5.4 Conclusion

The selected turbulence model, mesh strategy and wall modification were validated for beds containing spherical particles. The same method was assumed to be valid for the irregular particles. The results shows that the discrete CFD model simulations gave accurate results for the pressure drop and heat transfer through packed beds containing spheres. These results agreed with the experimental measurements taken by Allen *et al.* (2012).

The particles used in this study to approximate rock particle shapes gave fairly similar results to the spherical particle bed simulations. The results, however, suggest that the irregular particles represent the tortuous nature of rock beds. This study concludes that the particles used in this study can not be used as a universal representation of rock particle shapes in any configuration including different combinations of particle shapes and/or sizes. The heat transfer results obtained for the PES bed, however, agree with results found in literature.

## 6. Porous results and validation

The results from the porous CFD simulations are discussed in this section. The results were validated against two sets of experimental measurements done by Allen (2010) and Allen (2012). The first set of experimental measurements was used to validate the porous CFD model and test the sensitivity of the porous model parameters. The second set of experimental measurements was used to validate the porous CFD model with a more complex air-rock bed system.

### 6.1 Porous CFD model of shale rock bed experiment

The experimental setup is shown in Figure 6.1. Information regarding the experiment and the material properties of the shale is given in Table 6.1.

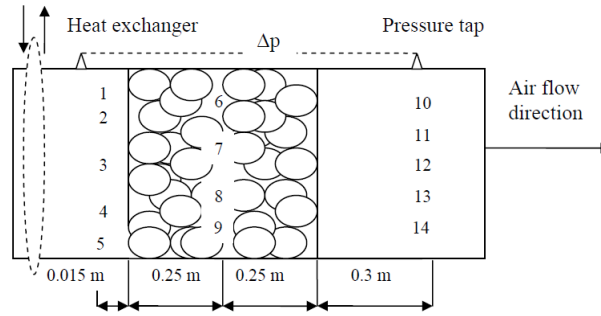
Table 6.1: Shale rock bed experiment information (Allen, 2010)

Ambient temperature [ $^{\circ}\text{C}$ ]	$\pm 25$
Charging Inlet temperature [ $^{\circ}\text{C}$ ]	$\pm 70$
$G$ [ $\text{kg}/\text{m}^2\text{s}$ ]	0.297, 0.467, 0.842
Shale density [ $\text{kg}/\text{m}^3$ ]	2720
$c_s$ [ $\text{J}/\text{kgK}$ ]	820 (@ 45 $^{\circ}$ C)
$\varepsilon$ []	$0.381 \pm 0.008$
$d_p$ [m]	0.0426

For a more detailed description of the experimental apparatus, measurement equipment and experimental uncertainties the reader should refer to Allen (2010).

#### 6.1.1 Porous CFD model setup

The porous CFD model is shown in Figure 6.2. The inlet and outlet boundaries were positioned more than 3 and 10 particle diameter before and after the bed respectively to eliminate boundary effects. They were modelled as a "mass-flow-inlet" and "pressure-outlet" respectively. All the wall boundaries were modelled with the "no-slip" boundary condition enabled, and the thermal boundary condition was set to a constant "heat flux" of zero modelling perfect insulation.



(a) Thermocouple positions

Figure 6.1: Experimental setup (Allen, 2010)

Mawire *et al.* (2009) note that in their simulations, the heat loss to the environment only became significant above 413 K. The maximum temperature modelled in the current simulations is 343 K. This served as the justification for this condition. The porous zone was modelled with the "physical velocity" option enabled. The Wakoa *et al.* (1979) correlation was used in the porous model. The fluid conductivity,  $k_f$ , was equal to that of air as given in Appendix E, and  $k_s$  was set to  $2 \text{ W/m}^2\text{K}$ . Results found in literature showed that the axial conduction has a very small effect on the temperature profile predictions, especially at relatively high flow rates (Hänchen *et al.*, 2010). The remaining rock properties were set as given in Table 6.1. The temperatures were taken at the exact position as used in the experiment.

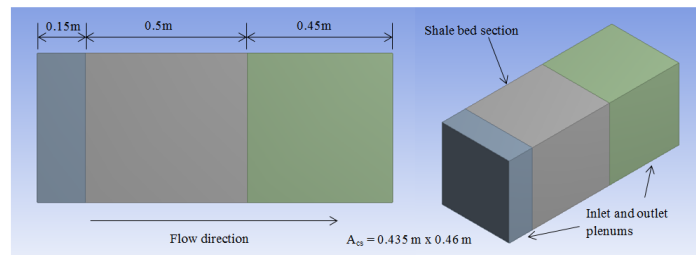


Figure 6.2: Porous CFD model of the shale bed

A structured grid was used to create the computational domain as seen in Figure 6.3. Three different mesh sizes were used to determine the porous model sensitivity to mesh size, namely coarse, medium and fine mesh with sizes of  $2d_p$ ,  $d_p$  and  $0.5d_p$  respectively as shown in Figures 6.3a, 6.3b and 6.3c. The Mesh sizes for the coarse, medium and fine meshes were 687, 3751 and 20 382 respectively.

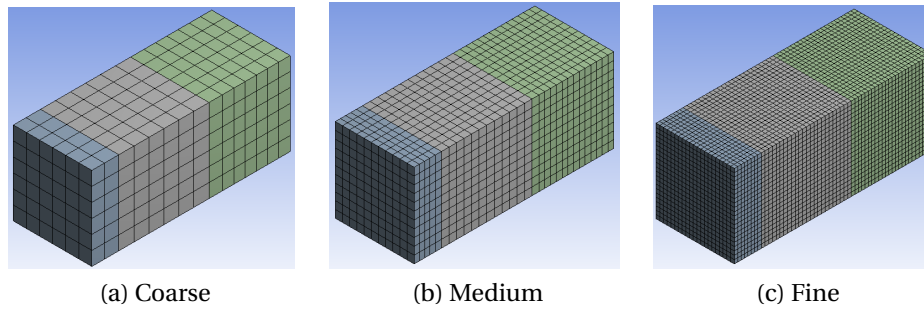


Figure 6.3: Shale bed model mesh

### 6.1.2 Porous CFD model results

The results from the porous model for the three different charging mass flow fluxes are shown in Figures 6.4a, 6.4b and 6.4c. The air temperature results from the experiment and CFD model were compared. The medium mesh was used for these simulations. The results matched well with the experimental results for all three mass flow fluxes.

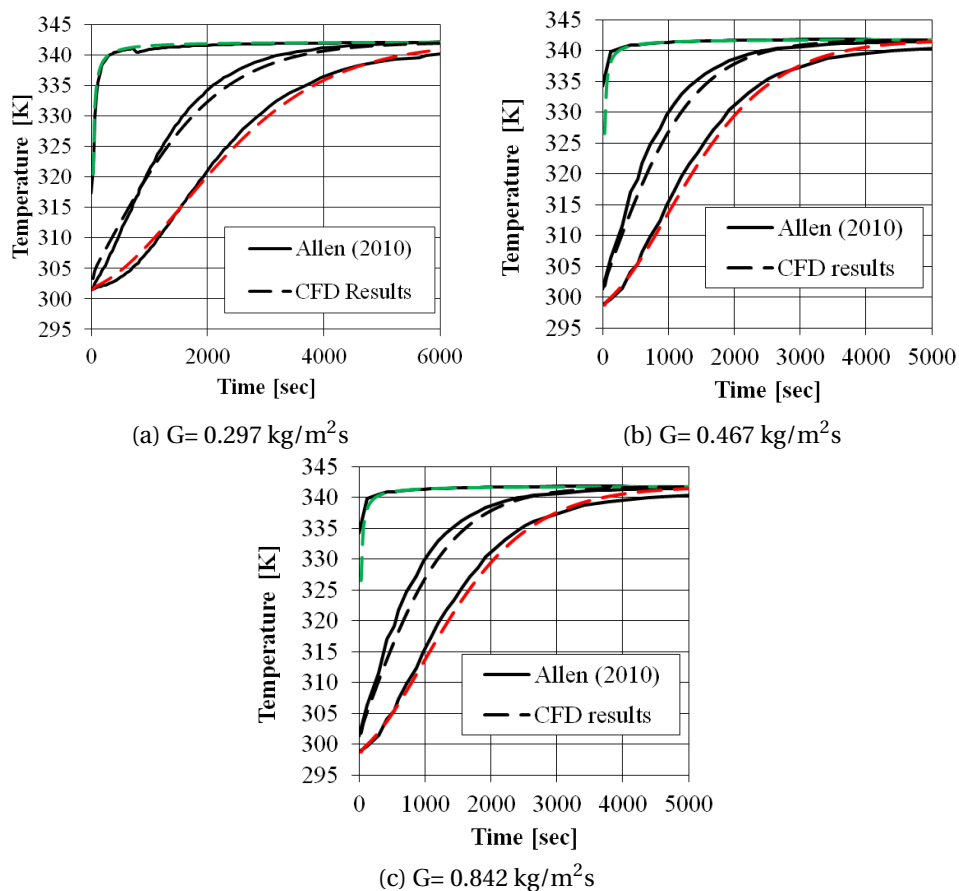


Figure 6.4: CFD porous model vs. experimental results

Figure 6.5 shows the mesh sensitivity results and indicates that the porous model was not very sensitive to the mesh. There was a small difference at the mid-section temperature profile. The coarse mesh predicted a slightly slower temperature rise in the mid-section. The medium and fine meshes predicted a similar temperature rise in the mid section. At the outlet, no difference could be seen between the different mesh sizes. The results indicated that the medium mesh was adequately fine enough. The inlet temperature was not compared because it was similar for all four meshes.

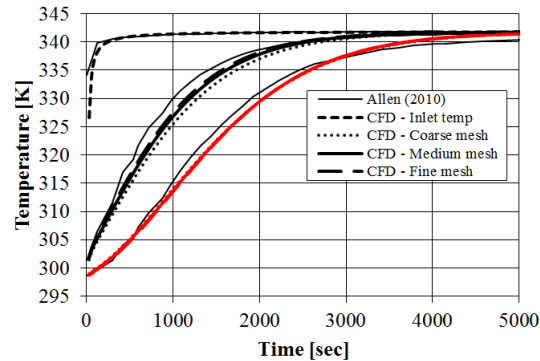


Figure 6.5: Porous CFD model mesh sensitivity ( $G = 0.467 \text{ kg/m}^2\text{s}$ )

In Figure 6.6 the effect of the heat capacity ( $c_s$ ) of the rock particles is shown using the medium mesh. The heat capacity was varied between 410 and 1640 J/kgK. When  $c_s$  equals 820 J/kgK, the result compares very well with the experimental results because it is equal to the  $c_s$  value that Allen (2010) experimentally determined for shale. By reducing the heat capacity to 410 J/kgK the thermal wave moved quicker through the bed as indicated by the steeper gradient of the results. The opposite was true when the  $c_s$  increased to 1640 J/kgK; the thermal wave moves slower as seen by the lower gradient of the results. As Hänchen *et al.* (2010) mention, and can again be seen here, the heat capacity is one of the most important material properties in an air-rock bed storage system.

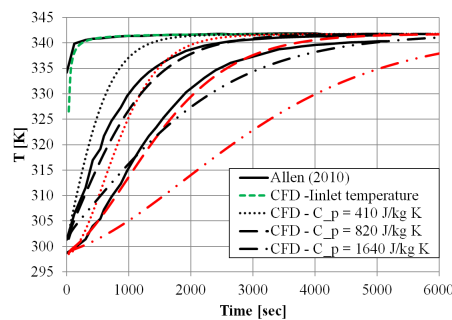


Figure 6.6: Porous CFD model  $c_s$  sensitivity ( $G = 0.467 \text{ kg/m}^2\text{s}$ )

Figure 6.7 shows the porous CFD model's sensitivity to the time step size. No difference between the two sets of CFD results can be seen, indicating that a time step of 30 seconds is adequate. However, Allen (2010) mentions that for simulations involving repeated charging and discharging, a smaller time step of 1 second is necessary for cycles when a previous cycle's results are used as the next cycle's input.

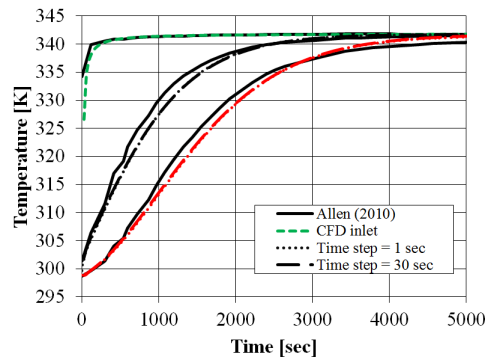


Figure 6.7: Porous CFD model time step sensitivity ( $G = 0.467 \text{ kg/m}^2\text{s}$ )

## 6.2 Porous CFD model of the Sauna

The University of Stellenbosch has recently commissioned an air-rock bed storage test facility referred to as the Sauna. The purpose of this system is to help the researchers understand the various performance parameters of an air-rock bed TES system. The Sauna rock bed test section is described in Appendix K and illustrated in Figure K.1. Photographs of the system are also shown in Appendix K.

### 6.2.1 Experiment

Thermal experiments using the Sauna have been conducted with dolerite obtained from a quarry near De Aar in the Northern Cape of South Africa (Allen, 2012). Information from the experiment is given in Table 6.2. The average density and average particle size (based on an equivalent spherical volume) of the rock is determined from 52 samples. The average porosity of the bed is calculated by weighing the rocks in the test section and uses the average rock density. Presently no information regarding the heat capacity of this specific rock set is available. The heat capacity is assumed to be equal to that of dolerite given in Table E.1 as determined by Allen (2010).

Table 6.2: Sauna experimental information

Charging/Discharging ambient temperature [ $^{\circ}\text{C}$ ]	$\pm 25/\pm 20$
Charging/Discharging Inlet temperature [ $^{\circ}\text{C}$ ]	$\pm 250/\pm 20$
Charging/Discharging mass flow rate [kg/s]	0.2485/0.3049
Dolerite density [kg/m <sup>3</sup> ]	2819.41
$c_p$ [J/kgK]	839 (@ 45 $^{\circ}\text{C}$ )
$\varepsilon$ []	0.45853
$d_p$ [m]	0.04432

### 6.2.2 Computational domain

The geometry and computational domain is shown in Figure 6.8. A hybrid mesh was used to create the computational domain. The rock bed section used a structured mesh and the more geometrically complicated top and bottom plenums used an unstructured mesh. The size of the mesh for the rock bed section was 0.04 m.

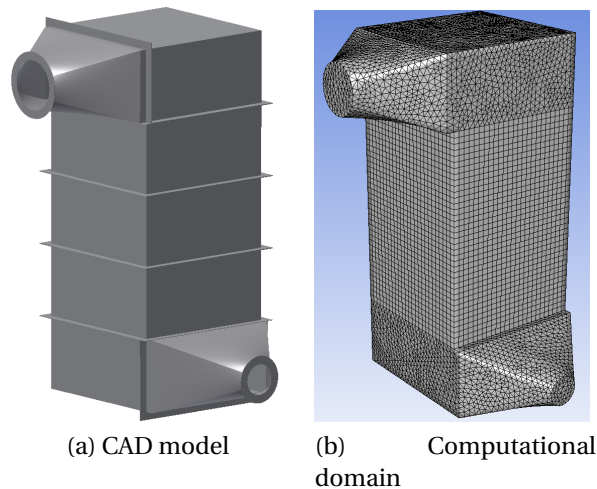


Figure 6.8: Sauna computational model

The inlet and outlet boundaries were set to "mass-flow-inlet" and "pressure-outlet" respectively. The top and bottom plenum walls were modelled with the "non-slip" boundary condition enabled and the thermal condition were set to constant "heat flux", with a value of  $0 \text{ W/m}^2$ , modelling perfect insulation. The heat loss through the plenums was not of importance because the top and bottom plenum thermocouple of the experiment was situated very close to the inlet and outlet of the rock bed.

The only heat loss which this study considered was of the rock bed section. The walls of the rock bed section were modelled with the "non-slip" boundary condition enabled, and the "convection" thermal condition was enabled to model natural convection effects. The wind condition was not measured during

the experiment; therefore an accurate prediction of the outside convection heat transfer coefficient was not possible. A heat transfer coefficient of  $10 \text{ W/m}^2\text{K}$  was chosen to account for natural convection on the outside surface of the Sauna. The thin wall model was used to model the insulation of the bed. The thin wall model eliminated the need to model the insulation of the bed and replaced it with a 1-D model, thus reducing the mesh size. However, this option limited the insulation to only using a constant temperature independent conductivity. An average conductivity of the material was used at the mean temperature of  $137.5^\circ\text{C}$ . The thermal resistance of all three materials was used to determine an effective conductivity, see Appendix K. The effective conductivity of the rock bed sections wall was determined to be  $0.0519 \text{ W/mK}$ .

The air properties given in Appendix E were used. The rock properties were set to the values given in Table 6.2. The conductivity of the rock particles was taken to be  $2 \text{ W/mK}$ , and the heat transfer correlation from Chandra and Willits (1981) was used. To account for the pressure loss, the Singh *et al.* (2006) correlation was used and the sphericity of the particles was taken as 0.54.

### 6.2.3 Sauna CFD results

The charging and discharging simulation results were compared to the experimental measurements in Figures 6.9 and 6.10, where the CFD results of both the solid and fluid phase temperatures are shown. The thermocouple only measured the air temperature and not the solid particle temperature.

The CFD results compare reasonably well with the experimental results for the charging cycle. The air temperature of the top layer compared excellently with the experimental results. The mid and bottom rock section showed the poorest comparison with the experimental results but still compared fairly well. At sections two and three, the predicted CFD fluid temperature increased faster.

The CFD results for the discharge cycle also compared reasonably well with the experimental results. Rock section three, which was the closest section to the inlet, agreed most favourably with the experimental measurements. Rock section one showed the least agreement with experimental measurements but still agreed reasonably well.

For both the charging and discharging simulations, the deviations from the experimental measurements were the largest at the rock bed sections closest to the bed outlet. For the charging simulation, rock bed section 3 was the closest to the outlet and for the discharging simulation, rock bed section 1 was closest to the outlet. This deviation could possibly be because the model assumed constant porosity. Zavattoni *et al.* (2011) state that the predicted temperature from their porous CFD model agrees better with experimental measurements for a quadratic porosity variation. Their results show similar characteristics when modelling the bed with a constant porosity.

Figure 6.11 shows the pressure drop experimental measurements and CFD predicted pressure drop versus time. Two sets of CFD simulation data are pre-

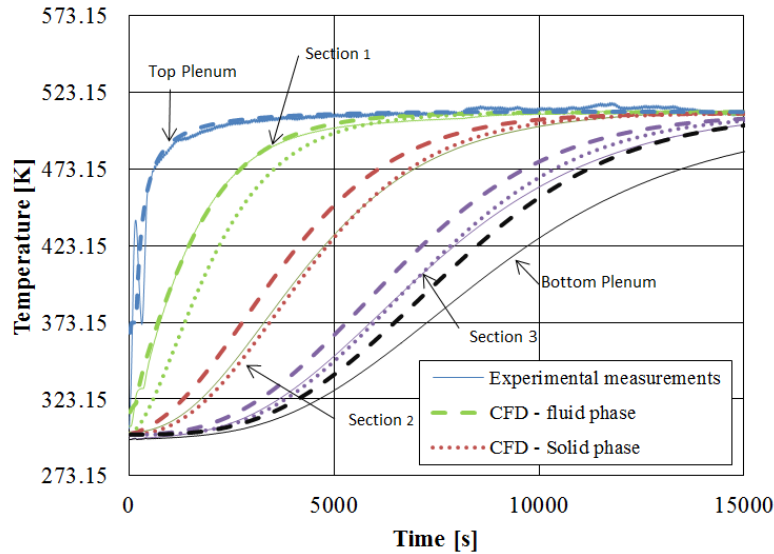


Figure 6.9: Sauna charging results

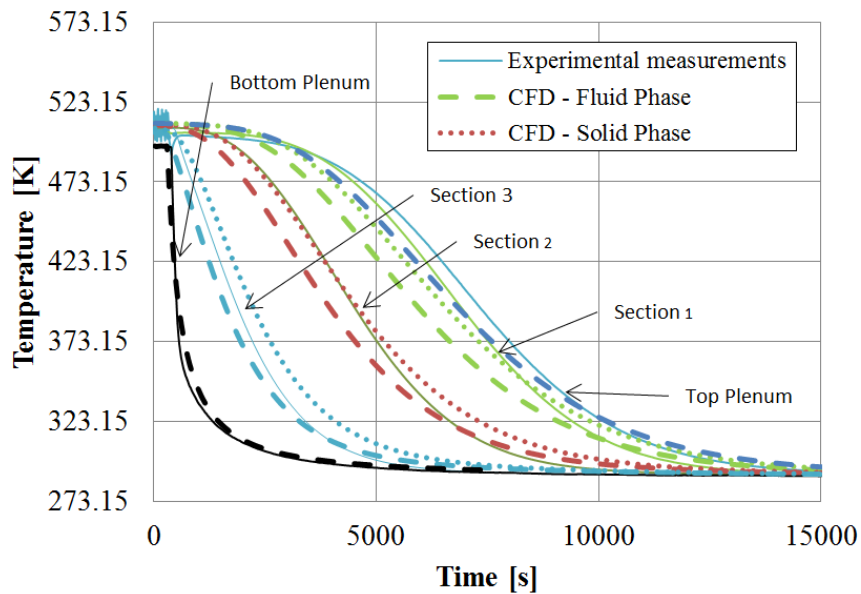


Figure 6.10: Sauna discharging results

sented to illustrate the effect of correct particle size characterization. One simulation used the equivalent spherical volume method to determine the particle sizes and the other used the equivalent cube volume method as described in Allen (2010). The equivalent cube volume method results in a particle size of 0.0357 m compared to the 0.0443 m determined by the former method. The simulations which used the equivalent cube volume method compared significantly better with the experimental measurements of the pressure drop. The average deviation between the equivalent cube volume method results and the experi-

mental measurements was roughly 21.3%. The under prediction can be due to a couple of factors. One possibility is the assumption of constant axial porosity which Zavattoni *et al.* (2011) also observe to under predict the pressure drop in their study. Another factor could be the presence of smaller particles distributed within the bed. The definition of the particle size clearly has a large effect on the

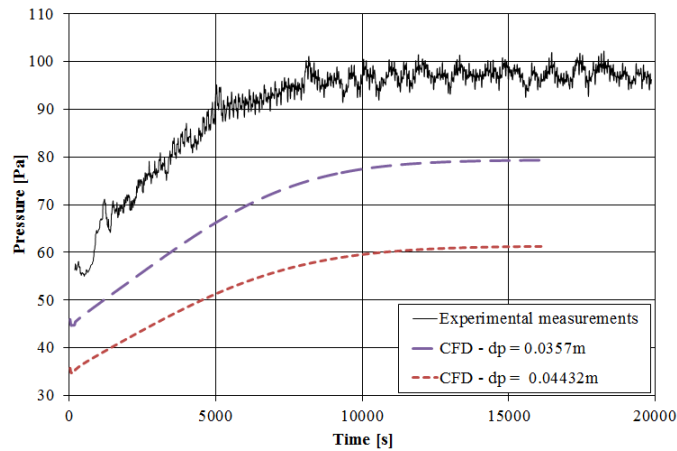


Figure 6.11: Sauna charging pressure drop results

pressure drop results. Figure 6.12 compares the thermal behaviour of the two different definitions of particle size. It is seen that the effect on the thermal performance is much smaller compared to the effect on the pressure drop.

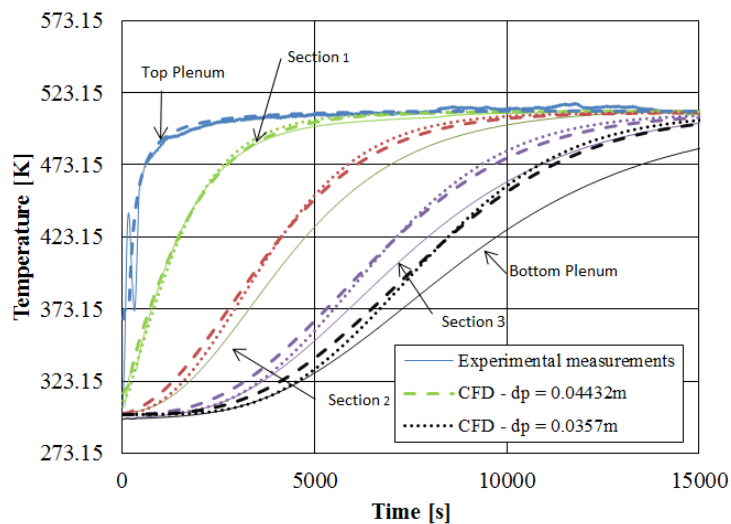


Figure 6.12: Sauna sensitivity to particles size

### **6.3 Conclusion**

The porous CFD model was able to predict the thermal behaviour of an air-rock bed fairly accurately. The heat capacity of the rock particles had a great effect on the thermal performance of the bed. The particle size had a very small to negligible effect on the thermal behaviour, but had a large effect on the pressure drop. The pressure drop results demonstrated the importance of defining rock particle sizes correctly as well as the need for a correlation that can accurately describe the pressure drop through a packed bed.

## 7. Application

This chapter examines the application of porous CFD modelling for a rock TES system design. The outcome of this work is to be able to simulate rock bed TES systems. This chapter illustrates the potential of CFD as a design tool. The simulation of a design concept referred to the Cone rock bed TES system is to determine the concepts feasibility.

### 7.1 Cone rock bed thermal energy storage system

Proposed by Gauché (2012), Figure 7.1 illustrates the geometry of the Cone rock bed and the basic concept.

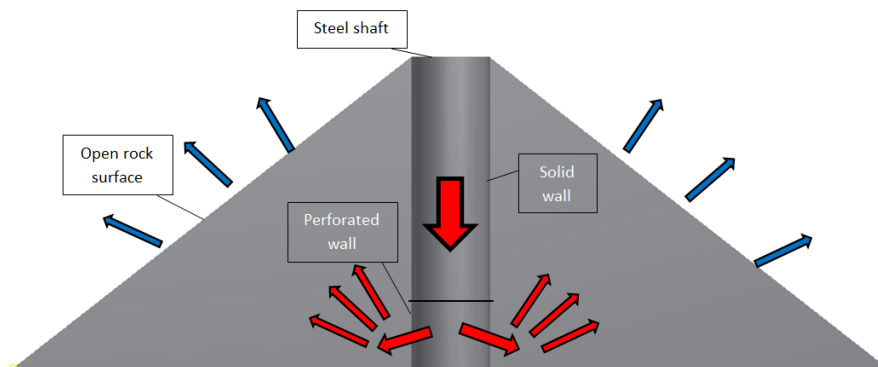


Figure 7.1: Cone rock bed storage

The system structure of the Cone rock bed TES system consists out of a very large pile of rocks with a large steel or concrete shaft penetrating the pile from top to bottom. The rock pile is sized large enough so that the rocks are self-insulating thereby protecting the system against the environment. Hot air is pumped downward through the central shaft at temperatures exceeding 800 K when charging. The lower portion of the shaft's wall is perforated to allow the hot air to escape the shaft, flow through the rock pile and rise to the rock surface of the bed. The process is simply reversed when the bed is discharged.

The proposed storage concept is intended to address economic issues as well as design issues such as the ratcheting effect and high pressure drops. The flow

area of the bed increases as the flow moves through the centre of the bed to the outside surface, resulting in low flow rates, and therefore low pressure drop. The largest pressure drop is expected to occur in the rock bed region close to the perforated portion of the shaft where initial high flow velocities may occur. To manage the pressure drop, two geometric parameters of the bed can be altered to decrease the inlet velocity at the center of the bed; these are the height of the perforated portion of the shaft and the shaft's radius. The absence of containing walls means that the ratcheting effect is eliminated.

The construction of this type of system could possibly be as simple as dumping a pile of rocks around a central shaft and allowing them to settle naturally or with minimum work input. The natural angle of repose of a rock pile is found to be between 37 and 40 degrees and was chosen to be 38 degrees for this investigation (Nel, 2013).

The size of the TES system investigated was required to supply 30 hours' worth of thermal energy for a 100 MW<sub>e</sub> steam power cycle. The parameters of the Cone rock bed under investigation was determined and given in Appendix H. The details of the setup of the porous CFD model for the Cone rock bed TES system is also found in Appendix H.

## 7.2 Results

The simulation was done for one charge cycle and one discharge cycle. The charge cycle was for 8 hours and the discharge cycle was for 30 hours. The temperature contours at the end of the charge and discharge cycles of a single plane through the bed can be seen in Figure 7.2. Figure 7.2a shows that the high temperature region remained well below the outer surface. In Figure 7.2b it is shown that at the end of the 30 hour discharge cycle, almost all of the thermal energy was extracted from the bed. In actual operation, the TES system will stop discharging when the outlet temperature falls below a certain set temperature or will reduce the flow rate to conserve the available energy. Several charge/discharge cycles would be needed before the system reaches steady state and is able to supply 30 hours of full load storage.

Figure 7.3 shows how the TES systems discharge temperature varied with time. The temperature dropped below 800 K at around 19 hours of discharging.

Figure 7.4 shows the charging and discharging pressure drop across the bed versus time. The largest pressure drop occurred in the immediate vicinity of the packed bed inlet at the perforated shaft section. During charging the pressure rise was fairly steep versus time, up until 2 hours. Between 2 and 8 hours the pressure rise was very gradual. This change in pressure rise is because after 2 hours the bed region close to the perforated shaft, where most of the pressure drop occurred due to the high velocity, had reached the inlet temperature. As a result, the fluid flow through that region was not expanding anymore due to temperature rise. The discharge graph shows similar results; once the temperature of the

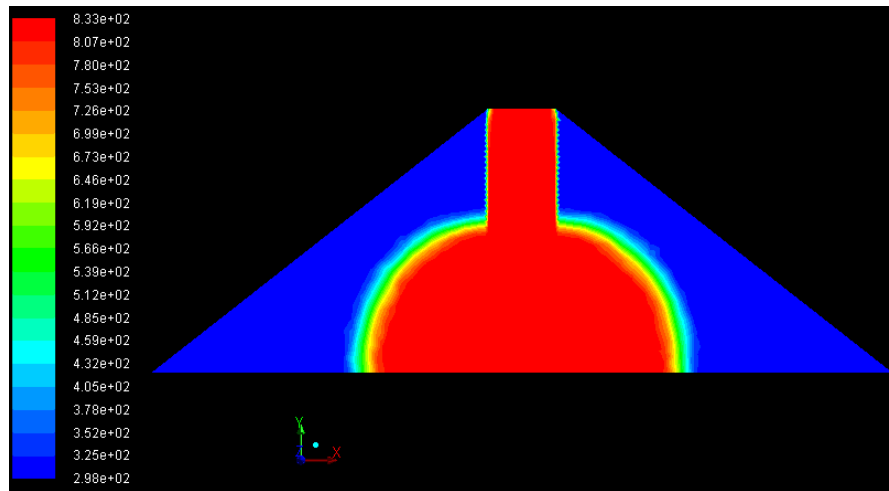
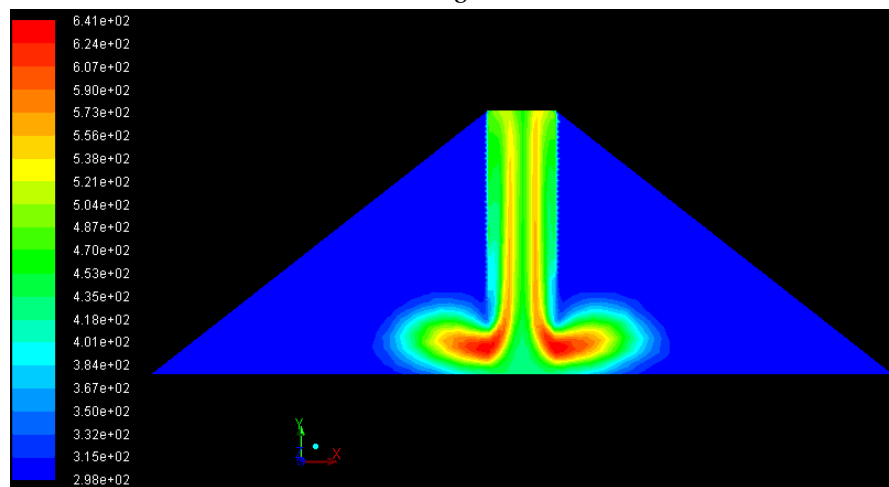
(a) Charge  $t = 8$  h(b) Discharge  $t = 30$  h

Figure 7.2: Charge/Discharge temperature contours

region close to the perforated shaft starts to decrease, the pressure versus time gradient starts to increase.

The pressure drop, during charging and discharge, is however too high and the parasitic pumping power that would be required would be too high for use of the particular bed presented, in CSP plants. The portion of perforated shaft which was set to 20% of the total shaft height shows to be too small. Figure 7.5 show that the pressure drop is much higher in the region nearest to the perforated shaft. The highest pressure drop gradient can be seen in Figure 7.5a, to occur roughly in a 20 m radius from the bed's center. To lower the pressure drop several parameters can be altered. The designer can increase the length of the perforated portion of the shaft and/or increase the shafts diameter. The size of the particles used in the bed can be increased or only the size of the particles in the near region of the perforated portion of the shaft, where the largest pressure

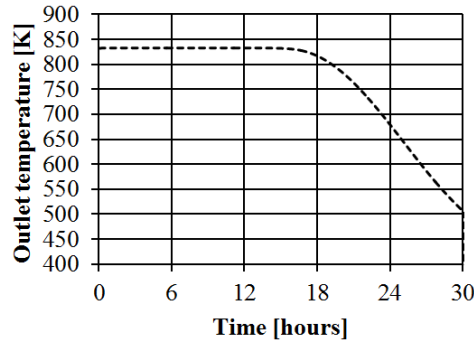
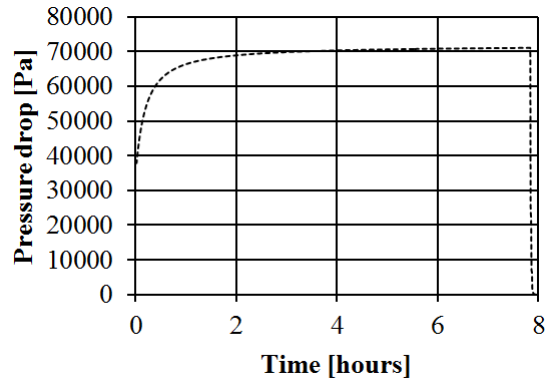
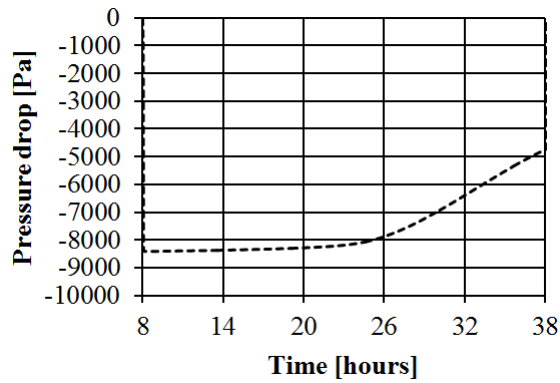


Figure 7.3: Discharging temperature vs. time



(a) Charge

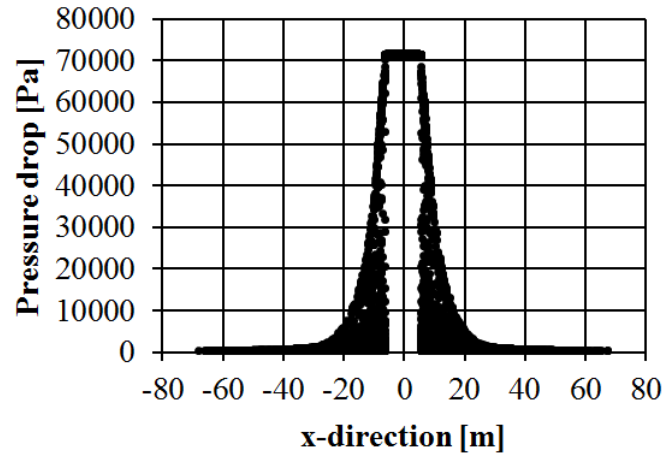


(b) Discharge

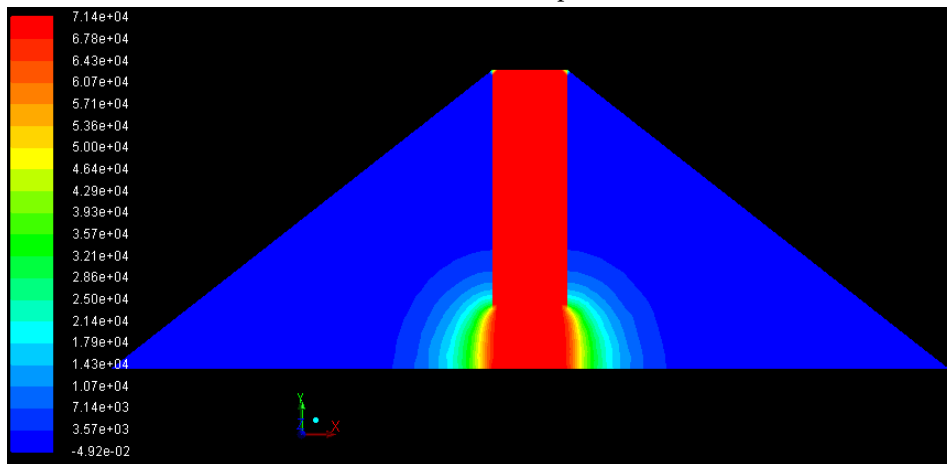
Figure 7.4: Pressure drop vs. Time

drop gradients exist, can be increased.

An optimal design point would be a system where the pressure drop is lowest, the thermal energy is extracted in the most effective way and the physical size of the storage system is minimal to reduce the total foot print of the storage.



(a) Cross section plot



(b) pressure contours

Figure 7.5: Pressure drop

### 7.3 Conclusion

The results show that the Cone rock bed concept has promising potential to be an effective and inexpensive air-rock bed storage system concept. The thermal wave moves through the bed in an acceptable manner, containing all the thermal energy supplied to the bed during charging.

The simulation performed, served as a high level validation of the concept in terms of thermal and pressure drop behaviour. Further simulation are required on this concept to complete the design in order to ensure that the size of the bed and shaft's dimensions are optimal for several charge/discharge cycles.

The system modelling capabilities of the porous CFD model was demonstrated with the Cone rock bed concept. The potential of CFD to be used as an optimization tool was shown with the simulation provided in this section. The performance parameters can easily be investigated to discover the optimal combination.

## 8. Conclusions

To date there has been no clear breakthrough for an air-rock bed thermal energy storage system for CSP. This study's objective was to investigate numerical methods which could be used to simulate various rock bed TES systems with the purpose of using the numerical models for system design and optimization. The proposition was that numerical methods can practically and accurately play an important role in the development and implementation of an air-rock bed TES system. The current computational power available makes it possible to simulate a large variety of TES systems with complex design features. These simulations can help the designer understand the behaviour of a particular design. The designer is empowered to test the theoretical design at a fraction of the cost and time of an equivalent pilot plant.

### 8.1 Conclusion from work done

Currently there is not a large amount of literature available regarding the pressure drop through a rock bed, and well-known correlation for spherical particles is not suitable for predicting the pressure drop over a rock bed. Experimental measurements found in Allen *et al.* (2012) show that it is not simple to generate a general pressure drop correlation for rock bed. The arbitrary shape of the particle and erratic packing behaviour may be the reason for this. Further research is needed to attempt to characterize the pressure drop behaviour of rock beds based on the rock type and/or the rock crushing method.

Numerical methods such as CFD can be used to accurately model the pressure drop through packed beds, as shown by previous studies such as Guardo *et al.* (2005) and Eppinger *et al.* (2010). Nearly all the literature found by this study concerning CFD and packed beds was for spherical particles only. This study found no clear cut method to model packed beds containing rock particles. In the field of bulk granular material however, the numerical method DEM has been proven by studies like Nel (2013) and Horn (2012) to accurately model packed beds containing rock particles. In light of this, DEM was used by this study to create the geometry, used to produce the computational domain of the rock beds. The simplified rock particles of Horn (2012) was used in this study instead of the more accurate though much more geometrically complex particles of Nel (2013), that are difficult to mesh with a reasonable mesh size. Two types of

CFD models were investigated in this study namely a discrete CFD model used to determine pressure drop and heat transfer data through packed beds and a porous CFD model used for system design and analysis.

Since the majority of the literature found concerning discrete CFD simulation through packed beds contained spherical particles, this study also used packed beds with spherical particles to determine the method of modelling flow and heat transfer through packed beds. The method established for the spherical beds was assumed to be valid for the beds containing irregular particles. Accurate results were obtained by the discrete CFD simulations for the pressure drop and heat transfer of a packed bed containing uniform spherical particles. The CFD results for spherical particles compared well to the pressure drop heat transfer correlations found in literature.

This study found that the CFD results of the non-uniform spherical, PES and elongated irregular packed beds agreed the best with the experimental measurements of Allen *et al.* (2012) for the cross-current packing crushed rock bed. The results, however, deviated considerably from the co-current packing results. Because all the CFD simulation done was for co-current packing, the results suggested that the particles used in the irregular beds fail to produce form drag. This was attributed to the fact that the simplified clump rock particles do not contain any blunt surfaces or sharp edges; therefore the orientation had little effect. The heat transfer results of the PES irregular packed bed showed agreement with correlations found in literature. The discrete CFD model shows that it poses the potential to accurately predict the pressure drop and heat transfer results of a packed bed of rocks. If the results from the current discrete CFD model of irregularly packed beds were to be used in the porous CFD model to model an air-rock bed TES, the pressure drop would most likely be under predicted. However the thermal behaviour should be captured fairly accurately.

Correlations from literature for pressure drop and heat transfer through packed beds were used in the porous CFD models. The porous CFD model of FLUENT showed fair agreement with the experimental measurement in terms of the temperature profile. It was found that the CFD model under predicted the pressure drop but showed that it can reproduce the pressure drop characteristic of a rock bed for charging and discharging. The most important parameters for heat transfer and pressure drop were found to be the heat capacity of the rocks and size of the particles respectively.

The potential for the porous CFD model was discussed in the applications chapter where it was used to prove the efficacy of an air-rock bed TES system design concept, referred to as the Cone rock bed. The design concept proposed by Gauché (2012), consists of a large pile of rocks with a central shaft that is perforated in the lower portion. The simulations for this system showed that the particular design parameters chosen for the Cone rock bed concept resulted in a relatively high pressure drop. The results shows the potential value of porous CFD model as a design tool. The simulation was able to identify important system parameters to optimize this TES system. Further simulations can now be

done to optimize the system.

The conclusion highlights that there are several difficulties for modelling packed bed in CFD, particularly discrete CFD models of packed beds containing crushed rock. However, initial evaluation shows that a combination of discrete CFD modelling and experimental results can be used successfully to define, refine and validate the thermal and pressure drop behaviour in a porous CFD model of an air-rock bed TES.

## 8.2 Recommendations for future work

This section presents recommendations of what future work should be done to improve the numerical methods. In general there remains much research to be done for modelling rock beds with discrete CFD models.

Accurate rock particle shape representation should be further investigated to provide better flow results. The current clump logic method creates a particle with many surface discontinuities. A method to smooth the surface of the clump particles is required.

Meshing strategies should be further investigated. Packed beds tend to have relatively large mesh sizes due to the the large number of particles usually required to model realistic beds.

The classification of typical rock particles should also be further investigated. The work of Nel (2013) and Horn (2012) provide a starting point to classify common rock particle shapes. More information regarding typical sphericity, specific surface area and so forth of different types of rock shapes must be made available to be able to select the proper numerical rock shape and distribution. This information will enable the designer to create accurate pressure drop and heat transfer correlations.

The effect of particle-to-particle and void-to-void radiation should be included in the discrete packed bed model. Investigating the effect of radiation within a packed bed will improve our understanding of the heat transfer process within the packed bed.

More work is needed to determine the porous CFD model's sensitivity to mesh density and time step size, specifically when simulating several charge and discharge cycles. The effect of axial porosity variation must also be further studied and included in the porous model.

A detailed study using the porous CFD model should be conducted to verify the Cone rock bed TES concept and to create an optimal design. To create an accurate model of this concept, a detailed mesh independence study should be conducted.

Further integration of CFD with DEM should be investigated in order to model the mechanical behaviour of the rock bed as the TES system is being charged. This should give us valuable insight into the thermal-mechanical behaviour of the rock particles during the charging and discharging process.

# **Appendices**

# A. Irregular packed bed geometry

## A.1 Non-uniform sized sphere bed

The non-uniform spherical particle is shown in Figure A.1. The bed is made out of three different size spherical particles with diameters of 15 mm, 20 mm and 30 mm. The bed contains 1894 particles in total, with 637, 633 and 624, 15 mm, 20 mm and 30 mm particles respectively. The bridge method is used to treat the contact points in the bed. The bridge method is used to eliminate the contact points. The bridge diameter is equal to 20% based on the average particles size of the bed ( $d_{p_{sv}}$ ). The porosity and bed parameters are shown in the figure. Tables A.1 and A.2 gives the details of the packed bed and its mesh's.

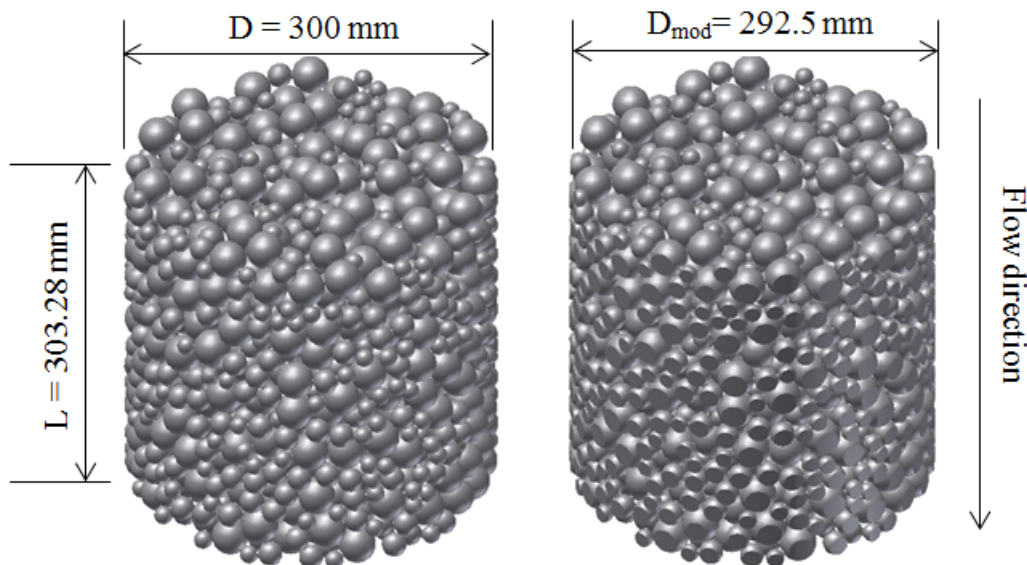


Figure A.1: Non-uniform sized sphere bed with and without channelling modification

Table A.1: Non-uniform sized sphere bed parameters

Number of particles	[]	1894
Bed height	[mm]	303.28
Bed diameter	[mm]	292.5
Bed porosity	[]	0.406
$\sum A_p / \sum V_p$	[1/mm]	0.22341
$d_{p_{sv}}$	[mm]	26.857
$D/d_{p_{sv}}$	[]	10.89
$H/d_{p_{sv}}$	[]	11.29

Table A.2: Non-uniform sized sphere bed mesh

Mesh size	[]	16 355 154
surf mesh size	[mm]	1.5
growth rate	[]	1.4
First prism layer height	[mm]	0.28
Prism layer growth rate	[]	1
Number of prism layers	[]	2

## A.2 PES particle bed

The PES particle bed is shown in Figure A.2. The bed contains the pyramid, elongated and spherical particles (see Section 3.1.7.1). The particles distribution is 21.9%, 37% and 41% for the spherical, pyramid and elongated particle respectively, similar to that used by Horn (2012). The particle size distribution for each particle is kept constant. The size of the pyramid particle based on equivalent spherical volume and the specific surface area of a sphere is 30 mm and 22.7 mm respectively. The size of the elongated particle diameter based on the equivalent spherical volume and the specific surface area of a sphere is 30 mm and 24.8 mm respectively. The size of the spherical particle based on equivalent spherical volume and the specific surface area of a sphere is 30 mm and 30 mm respectively. The PES particles are dropped into a ring of spherical particles that is packed in a structured order. The ring of spheres consist of 320 spherical particles with a diameter of 30.8 mm and is there to eliminate the wall effect. Two thirds of the particles are cut away as shown in Figure A.2. The porosity of the bed is very close to the porosity experimentally determined by Horn (2012), which is 0.459. The bridge method is used to eliminate the contact points. The size of the bridge diameter is 25% of the average particles size of the bed ( $d_{p_{sv}}$ ). Tables A.3 and A.4 gives the details of the packed bed and its mesh's.

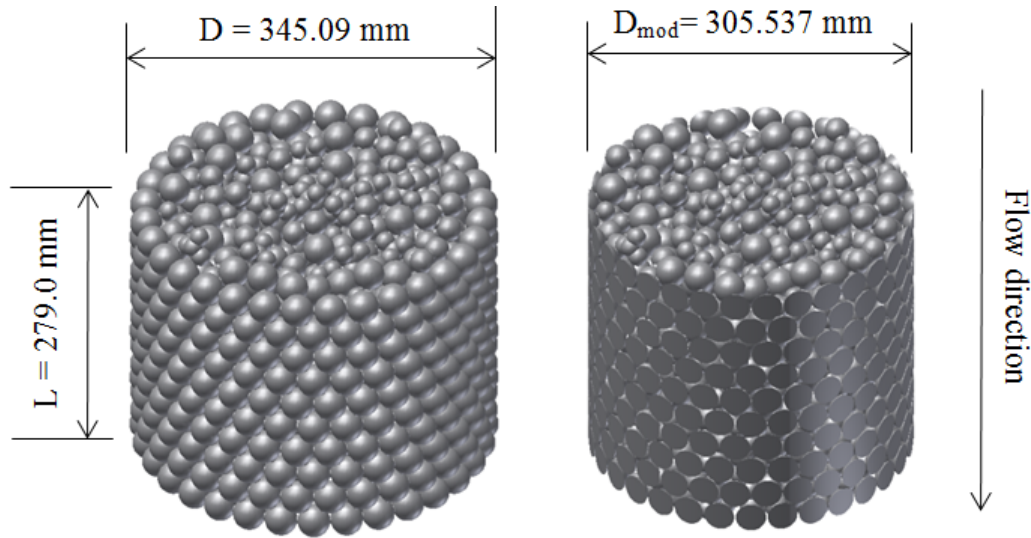


Figure A.2: PES bed with and without channelling modification

Table A.3: PES bed parameters

Number of particles	[]	751
Bed height	[mm]	279.0
Bed diameter	[mm]	305.537
Bed porosity	[]	0.442613
$\sum A_p / \sum V_p$	[1/mm]	0.23140
$d_{p_{sv}}$	[mm]	25.93
$D/d_{p_{sv}}$	[]	11.78
$H/d_{p_{sv}}$	[]	10.76

Table A.4: PES bed mesh

Mesh size	[]	12 218 942
surf mesh size	[mm]	1.75
growth rate	[]	1.4
First prism layer height	[mm]	0.22
Prism layer growth rate	[]	1
Number of prism layers	[]	2

### A.3 Elongated particle bed

The Elongated particles are dropped into a ring of spherical particles that is packed in a structured order. The ring of spheres consist of 320 spherical particles with a diameter of 30.8 mm and is there to eliminate the wall effect. Two thirds of the particles are cut away as shown in Figure A.3. The size of the elongated particle diameter based on the equivalent spherical volume and the specific surface area

of a sphere is 30 mm and 24.8 mm respectively. The bridge method is used to eliminate the contact points. The size of the bridge diameter is 25% of the average particles size of the bed ( $d_{p_{sv}}$ ). Tables A.5 and A.6 gives the details of the packed bed and its mesh's.

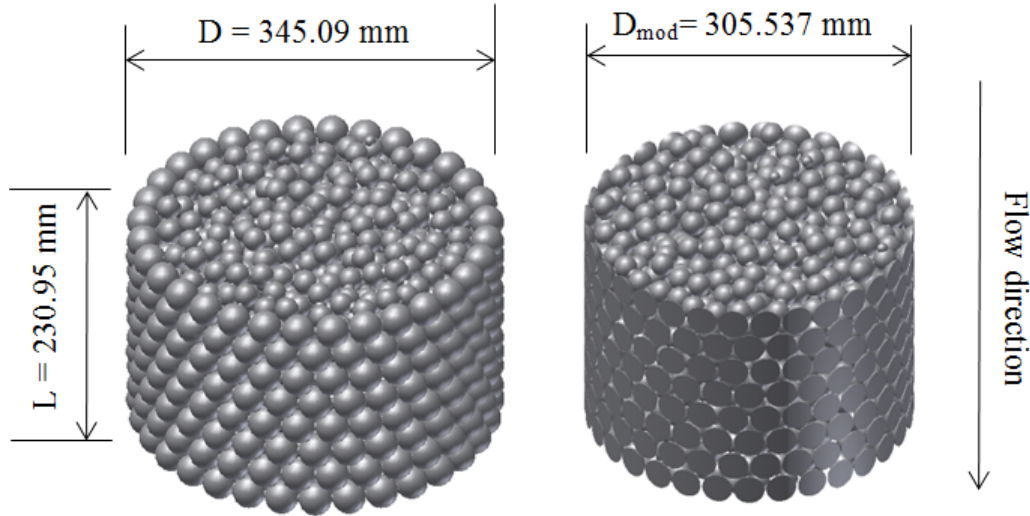


Figure A.3: Elongated particle bed with and without channelling modification

Table A.5: Elongated bed parameters

Number of particles	[]	750
Bed height	[mm]	230.95
Bed diameter	[mm]	305.537
Bed porosity	[]	0.439
$\sum A_p / \sum V_p$	[1/mm]	0.24116
$d_{p_{sv}}$	[mm]	24.88
$D / d_{p_{sv}}$	[]	12.28
$H / d_{p_{sv}}$	[]	9.28

Table A.6: Elongated mesh

Mesh size	[]	13 500 047
surf mesh size	[mm]	1.54
growth rate	[]	1.4
First prism layer height	[mm]	0.25
Prism layer growth rate	[]	1
Number of prism layers	[]	2

## A.4 Pyramid particle bed

The pyramid particles are dropped into a ring of spherical particles that is packed in a structured order. The ring of spheres consist of 320 spherical particles with a diameter of 30.8 mm and is there to eliminate the wall effect. Two thirds of the particles are cut away as shown in Figure A.4. The size of the pyramid particle based on equivalent spherical volume and the specific surface area of a sphere is 30 mm and 22.7 mm respectively. The bridge method is used to eliminate the contact points. The size of the bridge diameter is 25% of the average particles size of the bed ( $d_{p_{sv}}$ ). Tables A.7 and A.8 gives the details of the packed bed and its mesh's.

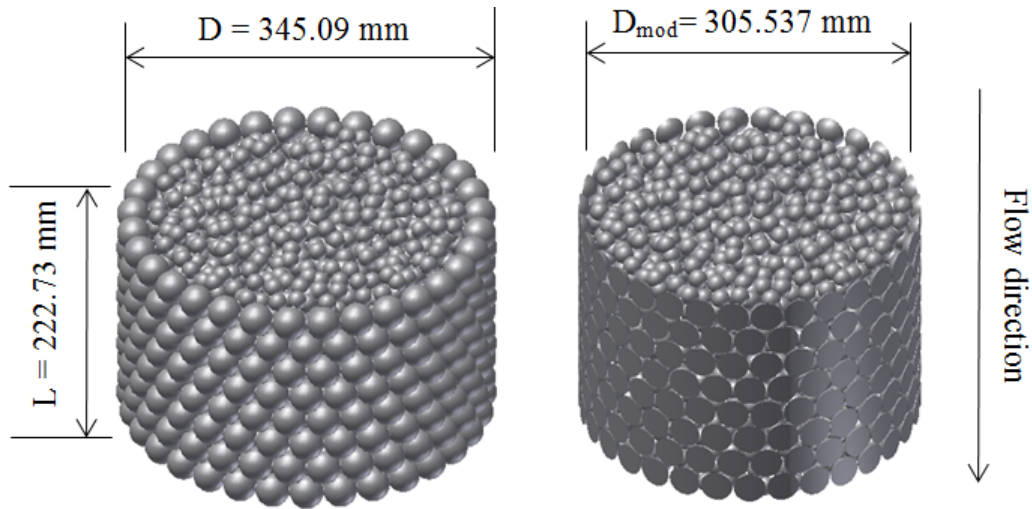


Figure A.4: Pyramid particle bed with and without channelling modification

Table A.7: Pyramid bed parameters

Number of particles	[]	750
Bed height	[mm]	222.73
Bed diameter	[mm]	305.537
Bed porosity	[]	0.434
$\Sigma A_p / \Sigma V_p$	[1/mm]	0.27024
$d_{p_{sv}}$	[mm]	22.20
$D/d_{p_{sv}}$	[]	13.76
$H/d_{p_{sv}}$	[]	10.03

Table A.8: Pyramid mesh

Mesh size	[]	16 058 995
surf mesh size	[mm]	1.475
growth rate	[]	1.4
First prism layer height	[mm]	0.22
Prism layer growth rate	[]	1
Number of prism layers	[]	2

## B. Computational fluid dynamics

### B.1 RANS turbulence models

The RANS models solve the time-average Navier-stokes equations, and all turbulence length scales are modelled. Reynolds decomposition is used to decompose all the flow variables into their mean,  $\bar{\mathbf{u}}$ , and fluctuating components,  $u'$ , and integrate over a large interval of time when compared to the small scale fluctuations (Dixon *et al.*, 2011). The time-average continuity and Navier-stokes equations are given in Equations B.1.1 and B.1.2 (Versteeg and Malalasekera, 2007).

$$\frac{\partial \bar{\rho}}{\partial t} + \text{div}(\rho \bar{\mathbf{u}}) = 0 \quad (\text{B.1.1})$$

$$\frac{\partial(\rho \bar{u})}{\partial t} + \text{div}(\rho \bar{u} \bar{\mathbf{u}}) = -\frac{\partial \bar{P}}{\partial x} + \text{div}(\mu \text{grad } \bar{u}) + \left[ -\frac{\partial(\overline{\rho u'^2})}{\partial x} - \frac{\partial(\overline{\rho u'v'})}{\partial y} - \frac{\partial(\overline{\rho u'w'})}{\partial z} \right] + S_{m_x} \quad (\text{B.1.2a})$$

$$\frac{\partial(\rho \bar{v})}{\partial t} + \text{div}(\rho \bar{v} \bar{\mathbf{u}}) = -\frac{\partial \bar{P}}{\partial x} + \text{div}(\mu \text{grad } \bar{v}) + \left[ -\frac{\partial(\overline{\rho u'v'})}{\partial x} - \frac{\partial(\overline{\rho v'^2})}{\partial y} - \frac{\partial(\overline{\rho v'w'})}{\partial z} \right] + S_{m_y} \quad (\text{B.1.2b})$$

$$\frac{\partial(\rho \bar{w})}{\partial t} + \text{div}(\rho \bar{w} \bar{\mathbf{u}}) = -\frac{\partial \bar{P}}{\partial x} + \text{div}(\mu \text{grad } \bar{w}) + \left[ -\frac{\partial(\overline{\rho u'w'})}{\partial x} - \frac{\partial(\overline{\rho v'w'})}{\partial y} - \frac{\partial(\overline{\rho w'^2})}{\partial z} \right] + S_{m_z} \quad (\text{B.1.2c})$$

The third, fourth and fifth terms on the right hand side of equations B.1.2a, B.1.2b and B.1.2c are the Reynolds stresses. The effects of the turbulence are represented by the Reynolds stresses. For an arbitrary scalar (e.g. temperature) transport equations similar to additional turbulent transport terms are added. The time average transport equation for the arbitrary scalar,  $\gamma$ , is given in Equation B.1.13 (Versteeg and Malalasekera, 2007).

$$\frac{\partial(\rho \bar{\gamma})}{\partial t} + \text{div}(\rho \bar{\gamma} \bar{\mathbf{u}}) = \tau_\gamma \text{div}(\text{grad } \bar{\gamma}) + \left[ -\frac{\partial(\overline{\rho u'\gamma'})}{\partial x} - \frac{\partial(\overline{\rho v'\gamma'})}{\partial y} - \frac{\partial(\overline{\rho w'\gamma'})}{\partial z} \right] + S_\gamma \quad (\text{B.1.3})$$

RANS turbulence models are based on the assumption that there is a similarity between the work done by the viscous stresses and Reynolds stresses on the mean flow. Experimental evidence found in literature showed that in isothermal incompressible flows turbulence decays unless there is shear in the flow. The Boussinesq hypothesis proposes that Reynolds stresses might be proportional to the mean rates of deformation. Using the suffix notation to simplify the Reynolds stresses notation, the Boussinesq hypothesis is given in Equation B.1.4 (Versteeg and Malalasekera, 2007)

$$-\rho \overline{u'_i u'_j} = \mu_t \left( \frac{\partial \bar{u}_i}{\partial x_j} + \frac{\partial \bar{u}_j}{\partial x_i} \right) - \frac{2}{3} \rho k \delta_{ij} \quad (\text{B.1.4})$$

where  $\bar{u}_i$  and  $\bar{u}_j$  represent the fluid mean velocity components  $u$ ,  $v$  and  $w$ . The subscripts  $i$  and  $j$  represent the Cartesian coordinate index. The turbulent viscosity is represented by  $\mu_t$ , the turbulent kinetic energy is represented by  $k = \frac{1}{2}(\overline{u'^2} + \overline{v'^2} + \overline{w'^2})$  and  $\delta_{ij}$  is the Kronecker delta. This assumption assumes that the turbulence is isotropic for the normal Reynolds stress, which has been shown to be inaccurate.

The turbulent transport of arbitrary scalar properties can be modelled similarly. The turbulent transport of a scalar is assumed to be proportional to the gradient of the mean value of the transported quantity as given below again in suffix notation (Versteeg and Malalasekera, 2007)

$$-\rho \overline{u'_i \gamma'} = \tau_t \frac{\partial \bar{\gamma}}{\partial x_i} \quad (\text{B.1.5})$$

where  $\tau_t$  represents the turbulent diffusivity. The Reynolds analogy assumption assumes that the transport of momentum and heat or mass is due to the same mechanism, and therefore it is expected that the value of  $\tau_t$  is quite close to that of  $\mu_t$ . The turbulent Prandtl/Schmidt number is given in Equation B.1.6 and is assumed to be unity for most CFD procedures (Versteeg and Malalasekera, 2007).

$$\sigma_t = \frac{\mu_t}{\tau_t} \quad (\text{B.1.6})$$

### B.1.1 $k - \epsilon$ turbulence model

The  $k - \epsilon$  turbulence model is the most widely used and validated turbulence model. It is classified as a two equation turbulence model due to the fact that it solves two equations namely the turbulent kinetic energy ( $k$ ) and rate of viscous dissipation ( $\epsilon$ ) transport equations. The  $k$  and  $\epsilon$  are used to define the velocity ( $\vartheta = \sqrt{k}$ ) and length scale ( $\ell = k^{3/2}/\epsilon$ ) of the large-scale turbulence which is

required to compute the turbulent viscosity. The relationship between the turbulent viscosity and  $k$  and  $\epsilon$  is shown in Equation B.1.7 (Versteeg and Malalasekera, 2007)

$$\mu_t = \rho C_\mu \frac{k^2}{\epsilon} \quad (\text{B.1.7})$$

where  $C_\mu$  is a dimensionless constant. The transport equations for  $k$  and  $\epsilon$  for the standard  $k - \epsilon$  turbulence model are given below in Equations B.1.8 and B.1.9.

$$\frac{\partial(\rho k)}{\partial t} + \text{div}(\rho k \bar{\mathbf{u}}) = \text{div}\left(\frac{\mu_t}{\sigma_k} \text{grad } k\right) + 2\mu_t \overline{s_{ij}} \cdot \overline{s_{ij}} - \rho \epsilon \quad (\text{B.1.8})$$

$$\frac{\partial(\rho \epsilon)}{\partial t} + \text{div}(\rho \epsilon \bar{\mathbf{u}}) = \text{div}\left(\frac{\mu_t}{\sigma_\epsilon} \text{grad } \epsilon\right) + C_{1\epsilon} \frac{\epsilon}{k} 2\mu_t \overline{s_{ij}} \cdot \overline{s_{ij}} - C_{2\epsilon} \rho \frac{\epsilon^2}{k} \quad (\text{B.1.9})$$

The five constants  $C_\mu$ ,  $\sigma_k$ ,  $\sigma_\epsilon$ ,  $C_{1\epsilon}$  and  $C_{2\epsilon}$  are set to 0.09, 1.00, 1.30, 1.44 and 1.92 respectively. The constants are determined from extensive data fitting for a wide range of flows (Versteeg and Malalasekera, 2007).

The standard  $k - \epsilon$  turbulence models perform well in confined flows where the Reynolds stresses are the most important, achieving success in calculating a wide range of thin shear layer and recirculation flows without the need for adjusting the model constants from case to case. Poorer performance is reported for unconfined flows. Poor agreement is reported for flows with weak shear layers such as far wakes and mixing layers. The spreading rate of axisymmetric jet in stagnant surroundings is greatly over predicted. Poor performance is reported for flows with large extra strains, rotating flows and where the flow is driven by anisotropy of the normal Reynolds stresses, such as a fully developed flow inside a non-circular duct (Versteeg and Malalasekera, 2007).

The RNG  $k - \epsilon$  turbulence model is more responsive to the effect of rapid strains and streamline curvature. The RNG  $k - \epsilon$  model is derived from the instantaneous Navier-stokes equation using a mathematical technique called the re-normalised group method. The model is similar to the standard  $k - \epsilon$  model, but it has different constants and additional terms and functions in the turbulent kinetic energy and turbulent dissipation transport equations. The turbulent viscosity is defined identically to the Standard  $k - \epsilon$  model (Fluent, 2011a).

The realizable  $k - \epsilon$  turbulence model was developed to overcome the deficiencies of the previous  $k - \epsilon$  turbulence models. The realizable  $k - \epsilon$  turbulence model contains a different formulation for the turbulent viscosity involving  $C_\mu$  which is no longer a constant but a variable and has modified the  $\epsilon$ -equation. The model gives better results for flows containing strong streamline curvature, vortices and rotation. The modified  $\epsilon$ -equation addresses the issue known as the round jet anomaly where the spreading rate of the axisymmetric jet is poorly predicted (Fluent, 2011a).

For high Reynolds numbers the model avoids the need to integrate the model right to the wall by introducing a wall function. The wall function makes use of

the universal behaviour of near wall flows and the log-law is satisfied as long as the mean velocity at a point  $y_p$ , where  $y$  is the co-ordinate normal to the wall, is within  $30 < y_p^+ < 500$ . The wall function relates the local wall shear to the mean velocity, turbulence kinetic energy and the rate of dissipation. In the case of heat transfer the model uses a wall function based on the universal near wall temperature distribution valid at high Reynolds numbers. In low Reynolds number flows the log-law is not valid and the  $k$ - and  $\epsilon$ -equations need to be integrated to the wall. The introduction of a non-linear wall-dampening function and modifications to the model, enables it to model low Reynolds number flows, but the equations that needs to be solved are numerically stiff and this may lead to poor convergence. The wall-dampening function ensures that the viscous stresses take over from the Reynolds stresses at low Reynolds numbers and in the viscous sub-layer adjacent to solid walls (Versteeg and Malalasekera, 2007).

The two layer model improves the treatment of near-wall flows for turbulent flows at low Reynolds numbers by dividing the boundary layer into two regions namely the fully turbulent and viscous region. In the fully turbulent region the standard  $k - \epsilon$  equations are used and the turbulent viscosity is solved as usual. In the viscous region only the  $k$ -equation is solved and a length scale is specified to evaluate the rate of dissipation (Versteeg and Malalasekera, 2007).

### B.1.2 Spalart-Allmaras model

The Spalart-Allmaras (S-A) model solves a transport equation for the kinematic turbulent viscosity parameter and specifies the length scale by using an algebraic formula. The relationship between the turbulent viscosity and kinematic eddy viscosity is given in Equation B.1.10

$$\mu_t = \rho \tilde{\nu} f_{v1} \quad (\text{B.1.10})$$

where  $f_{v1} = f_{v1}(\frac{\tilde{\nu}}{\nu})$  is the wall-damping function.  $f_{v1}$  tends toward unity for high Reynolds number flow and in so doing the  $\tilde{\nu}$ , kinematic turbulent viscosity parameter is just equal to the kinematic turbulent viscosity,  $\nu_t$ . At solid walls the wall damping function,  $f_{v1}$ , approaches zero. The Reynolds stresses are computed as given in Equation B.1.11 (Versteeg and Malalasekera, 2007).

$$-\rho \overline{u'_i u'_j} = \mu_t \left( \frac{\partial \overline{u}_i}{\partial x_j} + \frac{\partial \overline{u}_j}{\partial x_i} \right) = \rho \tilde{\nu} \left( \frac{\partial \overline{u}_i}{\partial x_j} + \frac{\partial \overline{u}_j}{\partial x_i} \right) \quad (\text{B.1.11})$$

The kinematic turbulent viscosity parameter transport equation is given in Equation B.1.12.

$$\begin{aligned} \frac{\partial(\rho \tilde{\nu})}{\partial t} + \text{div}(\rho \tilde{\nu} \mathbf{\bar{u}}) = \frac{1}{\sigma_\nu} \text{div} \left[ (\mu + \rho \tilde{\nu}) \text{grad}(\tilde{\nu}) + C_{b2} \rho \frac{\partial \tilde{\nu}}{\partial x_k} \frac{\partial \tilde{\nu}}{\partial x_k} \right] + \\ C_{b2} \rho \tilde{\nu} \left( \sqrt{2 \overline{\Omega_{ij} \cdot \Omega_{ij}}} + \frac{\tilde{\nu}}{\kappa y^2} f_{v2} \right) - C_{w1} \rho \left( \frac{\tilde{\nu}}{\kappa y} \right)^2 f_w \end{aligned} \quad (\text{B.1.12})$$

$$\frac{\partial(\rho\bar{\gamma})}{\partial t} + \text{div}(\rho\bar{\gamma}\bar{\mathbf{u}}) = \tau_\gamma \text{div}(\text{grad}\bar{\gamma}) + \left[ -\frac{\partial(\rho u'\gamma')}{\partial x} - \frac{\partial(\rho v'\gamma')}{\partial y} - \frac{\partial(\rho w'\gamma')}{\partial z} \right] + S_\gamma \quad (\text{B.1.13})$$

where  $\Omega_{ij}$  is the mean vorticity tensor, and the functions  $f_{v2} = f_{v2}(\frac{\tilde{v}}{y})$  and  $f_w = f_w(\frac{\tilde{v}}{\Omega\kappa^2 y^2})$  are further wall dampening functions. The length scale used is  $\kappa y$ , where  $y$  is the distance to the wall and  $\kappa$  is the von Karman's constant. The values for the constants  $\sigma_v$ ,  $\kappa$ ,  $C_{b1}$  and  $C_{b2}$  are equal to 2/3, 0.4187, 0.1355 and 0.622 respectively with  $C_{w1} = C_{b1} + \kappa^2 \left( \frac{1+C_{b1}}{\sigma_v} \right)$ .

The Spalart-Allmaras model is a relatively simple one-equation turbulence model that has shown good results for boundary layers subjected to adverse pressure gradients, but it is not well calibrated for free shear flows (Fluent, 2011a). The model has been fine tuned for external aerodynamic flows and has gained popularity among the turbomachinery community due to its suitability to aerofoil applications. The model struggles to define the length scale in complex geometries and is generally unsuitable for internal flows. It also lacks sensitivity to transport processes in rapidly changing flows (Versteeg and Malalasekera, 2007).

In the ANSYS FLUENT, the S-A model has been extended with a  $y^+$  insensitive wall treatment called the Enhanced Wall Treatment (EWT). All the solution variables from the viscous sublayer formulation  $u^+ = y^+$ , are automatically blended depending on  $y^+$ , to the corresponding logarithmic layer values  $u^+ = \frac{1}{\kappa} \ln(Ey^+)$ . The blending is calibrated to cover intermediate  $y^+$  values in the buffer layer  $1 \leq y^+ \leq 30$  (Fluent, 2011a).

### B.1.3 $k - \omega$ and SST $k - \omega$ model

The  $k - \omega$  turbulence model is classified as a two equation turbulence model. The two transport equations are the turbulent kinetics energy( $k$ ) and turbulence frequency ( $\omega$ ) equations. The turbulence frequency is defined as  $\omega = \frac{\epsilon}{k}$ . The velocity scale and length scale is defined as ( $\vartheta = \sqrt{k}$ ) and ( $\ell = \sqrt{k}/\omega$ ) respectively. The eddy viscosity is given in Equation B.1.14 .

$$\mu_t = \rho \frac{k}{\omega} \quad (\text{B.1.14})$$

The transport equation is given in Equations B.1.15 and B.1.16.

$$\frac{\partial(\rho k)}{\partial t} + \text{div}(\rho k \bar{\mathbf{u}}) = \text{div} \left[ \left( \mu + \frac{\mu_t}{\sigma_k} \right) \text{grad} k \right] + \left( 2\mu_t \overline{s_{ij}} \cdot \overline{s_{ij}} - \frac{2}{3} \rho k \frac{\partial \overline{u_i}}{\partial x_j} \delta_{ij} \right) - \beta^* \rho k \omega \quad (\text{B.1.15})$$

$$\frac{\partial(\rho \omega)}{\partial t} + \text{div}(\rho \omega \bar{\mathbf{u}}) = \text{div} \left[ \left( \mu + \frac{\mu_t}{\sigma_\omega} \right) \text{grad} \omega \right] + \gamma_1 \left( 2\rho \overline{s_{ij}} \cdot \overline{s_{ij}} - \frac{2}{3} \rho \omega \frac{\partial \overline{u_i}}{\partial x_j} \delta_{ij} \right) - \beta_1 \rho \omega^2 \quad (\text{B.1.16})$$

The values of the model constants  $\sigma_k$ ,  $\sigma_\omega$ ,  $\gamma_1$ ,  $\beta_1$  and  $\beta^*$  are 2.0, 2.0, 0.553, 0.075 and 0.09.

A key feature of this turbulence model is that there is no need for a wall damping function in low Reynolds number applications because it can be integrated to the wall. The turbulence kinetic energy at the wall is set to zero and the frequency  $\omega$  approaches infinity at the wall. The model is problematic for external aerodynamic and aerospace applications involving a free stream boundary, because  $\omega \rightarrow 0$  at the free stream boundary. From Equation B.1.14 it is seen that this would result in an indeterminate or infinite value for  $\mu_t$ . Therefore a small non-zero value for  $\omega$  must be specified and the result of the model unfortunately has shown to depend on this assumed free stream value (Versteeg and Malalasekera, 2007).

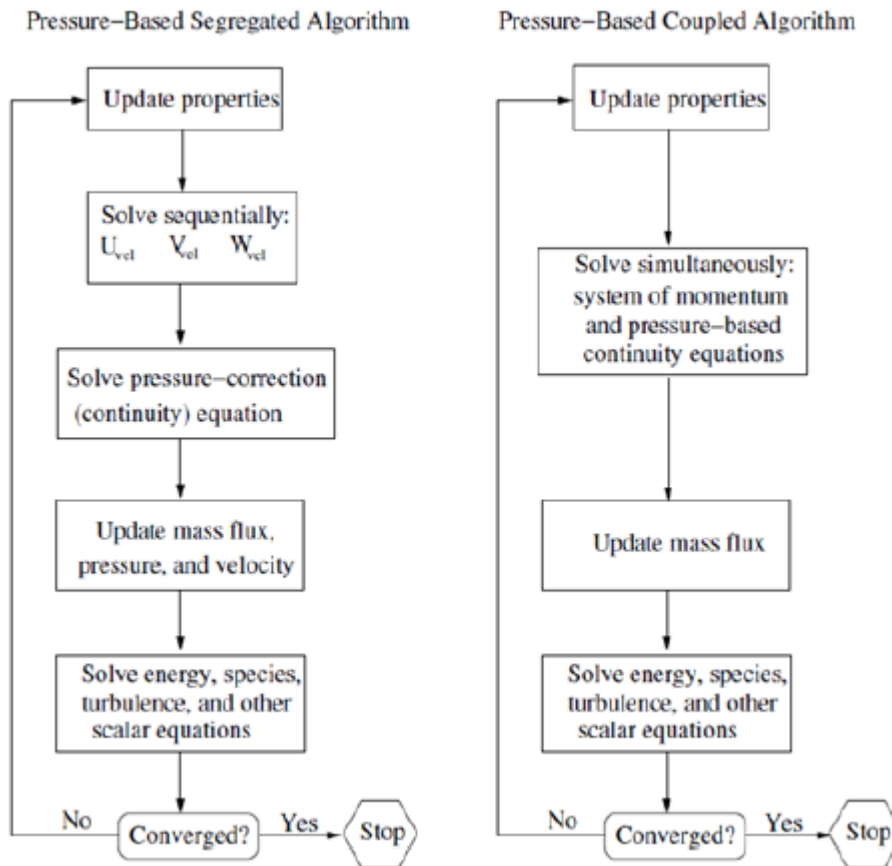
The SST  $k - \omega$  model is a hybrid model that transforms the  $k - \epsilon$  model into a  $k - \omega$  model in the near wall region and uses the standard  $k - \epsilon$  model in the fully turbulent region far from the wall. The  $k - \epsilon$  model is less sensitive to assumed values in the free stream and is therefore used for the region far from the wall. However it has poor performance near the wall for flows with adverse pressure gradients. Therefore the  $k - \omega$  model is used in the near wall regions. Equation B.1.15 for  $k$  remains the same but the  $\epsilon$ -equation is transformed into a  $\omega$ -equation by substituting  $\epsilon = \omega k$  (Versteeg and Malalasekera, 2007). The transformed  $\epsilon$ -equation is given in Equation B.1.17

$$\frac{\partial(\rho\omega)}{\partial t} + \text{div}(\rho\omega \bar{\mathbf{u}}) = \text{div} \left[ \left( \mu + \frac{\mu_t}{\sigma_{\omega,1}} \right) \text{grad } \omega \right] + \gamma_2 \left( 2\rho \overline{s_{ij}} \cdot \overline{s_{ij}} - \frac{2}{3} \rho \omega \frac{\partial \overline{u_i}}{\partial x_j} \delta_{ij} \right) - \beta_2 \rho \omega^2 + 2 \frac{\rho}{\sigma_{\omega,2} \omega} \frac{\partial k}{\partial x_k} \frac{\partial \omega}{\partial x_k} \quad (\text{B.1.17})$$

Comparison of Equations B.1.16 and B.1.17 show an additional source term. The SST models constants  $\sigma_k$ ,  $\sigma_{\omega,1}$ ,  $\sigma_{\omega,2}$ ,  $\gamma_2$ ,  $\beta_2$  and  $\beta^*$  are 1.0, 2.0, 1.17, 0.44, 0.083 and 0.09 (Versteeg and Malalasekera, 2007).

## B.2 Pressure-based solvers

Figure B.1 graphically shows the segregated and coupled pressure-based algorithms.

Figure B.1: Pressure-based solver (Fluent, 2011*a*)

## C. Boundary conditions

### C.1 Discrete CFD model's boundaries

#### C.1.1 Boundaries

To minimize the influence of the inlet and outlet boundaries, the inlet and outlet boundaries were extended by 3 particle diameters and 2 container diameters respectively. This is shown in Figure C.1.

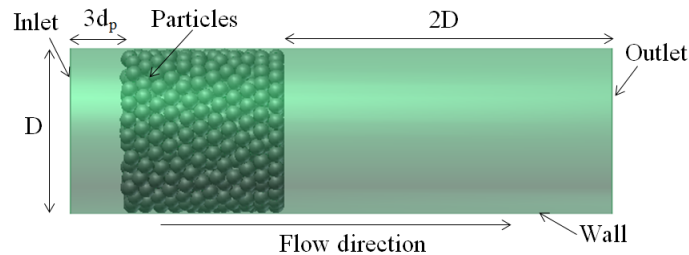


Figure C.1: Flow domain boundaries

The boundaries are an inlet, an outlet, a wall and a particle, and each are described below.

The inlet boundary was specified as a constant velocity-inlet. The inlet velocity value was derived from the required particle Reynolds number,  $Re_p$ . The inlet turbulent intensity,  $I$ , was determined from Equation C.1.1, found in Dixon *et al.* (2013), to specify the initial turbulence when the flow regime is turbulent. The inlet temperature was set to 300 K for all simulations.

$$I = 0.16Re_p^{\frac{1}{8}} \quad (\text{C.1.1})$$

The outlet was specified as a pressure-outlet with a gauge pressure of 0 Pa and a temperature of 300 K. The wall was modelled as a non-slip boundary with a constant heat flux of  $0 \text{ W/m}^2$ . The particle was modelled as a non slip wall boundary. The temperature of the particle was set to 400 K for the heat transfer simulation and 300 K for the pressure drop simulations.

## C.2 Porous CFD model's boundaries

### C.2.1 Zones and boundaries

The computational domain was divided into fluid and porous zones. The fluid zone consisted of the inlet and outlet plenum, and the porous zone was made up of the porous media. The normal momentum, continuity and energy equations were solved in the fluid zone. In the porous zone, the modified momentum and energy equations for porous media were solved with the continuity equation. The thermal non-equilibrium option was enabled for the porous zone which uses a dual cell approach. A UDF was used to determine the viscous and inertial resistance coefficients for the momentum sink term. The UDF also determined the solid-to-fluid volumetric heat transfer coefficient that describes the heat transfer between the porous solid and fluid region. Examples of the UDF used are shown in Appendix J.

The inlet boundary was defined as an inlet-mass-flow boundary. A UDF was used to specify a varying inlet mass flow or inlet temperature profile with time for a transient solution. The inlet-mass-flow boundary can also be used as an outlet by specifying the normals outward. The outlet boundary was set as a pressure-outlet with the reverse flow temperature set to 300 K and the gauge pressure set to 0 Pa. The porous wall was modelled as a non-slip boundary. In the thermal modelling of the wall the thin-wall assumption and the convection option was enabled. The thickness of this thin wall was set by the user and the convection coefficient was set to  $10 \text{ W/m}^2\text{K}$  to model natural convection losses. The fluid wall was modelled as an adiabatic non-slip boundary.

## D. Reynolds number definition

### D.1 Reynolds number

The Reynolds number is defined as the ratio between the inertial and the viscous forces of the fluid and is expressed as shown in Equation D.1.1,

$$Re = \frac{\rho_f U d}{\mu} \quad (\text{D.1.1})$$

where  $\rho_f$  is the fluid density,  $U$  is the average fluid velocity,  $d$  is the characteristic length and  $\mu$  is the fluids viscosity. It is used as an indicator to show when the flow becomes turbulent, where the inertial forces dominates. For circular pipes the flow is laminar for  $Re \leq 2300$  and turbulent for  $Re \geq 4000$  (Cengel and Cimbala, 2006). The exact  $Re$  values where the flow becomes turbulent differs from case to case depending on the geometry and flow conditions (surface roughness, surface temperature, type of fluid and other disturbances).

Eisfeld and Schnitzlein (2001) defines the flow regime in packed beds by the particle Reynolds number

$$Re_p = \frac{\rho_f U_0 d_p}{\mu} \quad (\text{D.1.2})$$

where  $U_0$  is the superficial velocity and  $d_p$  is the particle diameter. The flow is laminar at  $Re_p < 10$ , transitional at  $10 \leq Re_p \leq 300$  and turbulent at  $Re_p > 300$ .

Holdich (2002) presents a different definition for the Reynolds number of a packed bed. The fluid velocity term and the characteristic linear dimension of the Reynolds number are modified. The velocity term is defined by the interstitial velocity which is related to the superficial velocity. The characteristic linear dimension is related to the volume open to the fluid flow divided by the wetted surface area

$$u = \frac{U_0}{\varepsilon} \quad (\text{D.1.3})$$

$$d = \frac{A_{cs} L \varepsilon}{A_{cs} L (1 - \varepsilon) S_v} = \frac{\varepsilon}{(1 - \varepsilon) S_v} \quad (\text{D.1.4})$$

where  $S_v$  is the specific area of the particles.

Substituting Equation D.1.3 and D.1.4 into Equation D.1.1 results in

$$Re_1 = \frac{\rho U_0}{(1 - \varepsilon) S_V \mu} \quad (D.1.5)$$

According to this Reynolds number definition the turbulent regime occurs at  $Re_1 \geq 2$  (Holdich, 2002). This definition of the Reynolds number ( $Re_1$ ) will be referred to in this study as the Carman Reynolds number.

Allen *et al.* (2012) defines the Reynolds number for a packed bed by assuming duct flow which accounts for skin friction and form drag in the friction factor. To illustrate the assumption the author considers a structured packing which is divided into repeatable control volumes. The characteristic length is defined by the hydraulic diameter of the duct as shown below in Equation D.1.6

$$d_h = \frac{4A_{cs}P_l}{\sum A_p} = \frac{4\varepsilon \sum V_p}{(1 - \varepsilon) \sum A_p} \quad (D.1.6)$$

where

$$A_{cs} = V_V / P_l \quad (D.1.7)$$

and

$$V_V = \varepsilon \sum V_p / (1 - \varepsilon) \quad (D.1.8)$$

$A_{cs}$  is average fluid cross sectional area,  $P_l$  is the pitch of the structured packing in the flow direction and  $V_V$  is the void volume. The velocity is related to the superficial velocity.

$$u_{duct} = \frac{U_0}{\varepsilon} \quad (D.1.9)$$

where  $u_{duct}$  is the flow speed through the duct. Substituting Equation D.1.6 and D.1.9 in to Equation D.1.1 results in

$$Re_2 = \frac{4\rho_f U_0 \sum V_d}{(1 - \varepsilon) \mu \sum A_d} \quad (D.1.10)$$

This definition of the Reynolds number ( $Re_2$ ) will be referred to in this study as the Allen Reynolds number.

The Reynolds number given in Equation D.1.11 is referred to by Allen *et al.* (2012) as the Ergun Reynolds number ( $Re_{Erg}$ ).

$$Re_{Erg} = \frac{\rho_f U_0 d_d}{(1 - \varepsilon) \mu} \quad (D.1.11)$$

## E. Material properties

The rock properties discussed in Section 2.3 is presented in Tables E.1 and E.2. The Equation used for the air properties is also given in this appendix.

### E.1 Rock properties

Table E.1: South African rock properties

Literature	Rock type	General Region	$k_s \left[ \frac{W}{mK} \right]$	$\rho_s \left[ \frac{kg}{m^3} \right]$	$c_s \left[ \frac{J}{kgK} \right]$	$\rho_s c_s \left[ \frac{MJ}{m^3K} \right]$
Allen (2010):	Shale	Southern Namibia		2750	820(±64)	2.3
	Granite	Calvina, Northern cape		2893	845(±40)	2.5
	Dolerite	Kenhart, Northern cape		2657	839(±41)	2.2
Jones (2003):	Karoo Dolerite		1.99(±0.13)	2960(±80)		
	Pre-Karoo-diabase		3.97(±0.78)	2900(±80)	840(±30)	2.4
	Shale	Witwatersrand supergroup	4.77(±1.20)	2790(±60)	880(±20)	2.5
	Conglomerate	Witwatersrand supergroup	6.86(±0.75)	2730(±60)	830(±50)	2.3
	Quartzite	Witwatersrand supergroup	6.35(±0.78)	2690(±40)	810(±40)	2.2
	Quartzite	Ventersdorp formation	7.59	2740	840	2.3
	Lava	Ventersdorp supergroup	3.46(±0.56)	2850(±40)	880(±40)	2.5

Table E.2: Rock properties experimentally measured by Zanganeh *et al.* (2012)

Rock type	$k_{S@298K}$	$k_{S@348K}$	$k_{S@396K}$	$k_{S@446K}$	$\rho_s \left[ \frac{kg}{m^3} \right]$	$c_s \left[ \frac{J}{kgK} \right]$	$\rho_s c_s \left[ \frac{MJ}{m^3K} \right]$
Quartzite	5.39(0.07)	4.05(0.17)	3.76(0.13)	3.37(0.11)	2618(1.68)	623(12)	1.6
Calcareous sandstone	4.36(0.15)	3.26(0.24)	3.16(0.18)	2.98(0.09)	2661(1.71)	652(32)	1.7
Helvetic siliceous limestone	3.6(0.21)	3.32(0.24)	2.83(0.16)	2.72(0.15)	2776(2.95)	669(15)	1.9
Limestone	2.82(0.06)	2.41(0.07)	2.20(0.05)	2.05(0.03)	2697(1.66)	683(15)	1.8
Gabbro	2.05(0.08)	1.99(0.09)	2.18(0.06)	2.05(0.04)	2911(2.69)	643(24)	1.9

### E.2 Air properties

#### E.2.1 Ideal gas law

$$\rho_f = \frac{P}{RT} \quad (E.2.1)$$

Where  $R$  is the gas constant for air equal to  $0.287 \text{ J/kgK}$  (Cengel and Cimbala, 2006).

### E.2.2 Viscosity

The power law is show in Equation E.2.2.

$$\mu = \mu_{ref} \left( \frac{T}{T_{ref}} \right)^n \quad (\text{E.2.2})$$

where  $\mu_{ref}$ ,  $T_{ref}$  and  $n$  are equal  $1.716 \times 10^{-05} \text{ kg/m} \cdot \text{s}$ ,  $273.11 \text{ K}$  and  $0.666$  respectively (Fluent, 2011*a*).

### E.2.3 Conductivity

$$k_f = -2.109516 \times 10^{-08} T^2 + 8.618455 \times 10^{-05} T + 1.7260978 \times 10^{-03} \quad (\text{E.2.3})$$

Correlated from data found in Cengel (2006) for the temperature range  $273 \text{ K} \leq T \leq 873 \text{ K}$ .

### E.2.4 Heat capacity

$$c_{p_f} = -6.531632 \times 10^{-07} T^3 + 1.317068 \times 10^{-03} T^2 - 6.289793 \times 10^{-01} T + 1.094543 \times 10^{03} \quad (\text{E.2.4})$$

Correlated from data found in Cengel (2006) for the temperature range  $273 \text{ K} \leq T \leq 873 \text{ K}$ .

## F. Solar map

### F.1 DNI solar map of South Africa

In Figure F.1 the Direct Normal Irradiance (DNI) solar map of South Africa is shown. The map shows that the western and central parts of South Africa has the most solar resources.

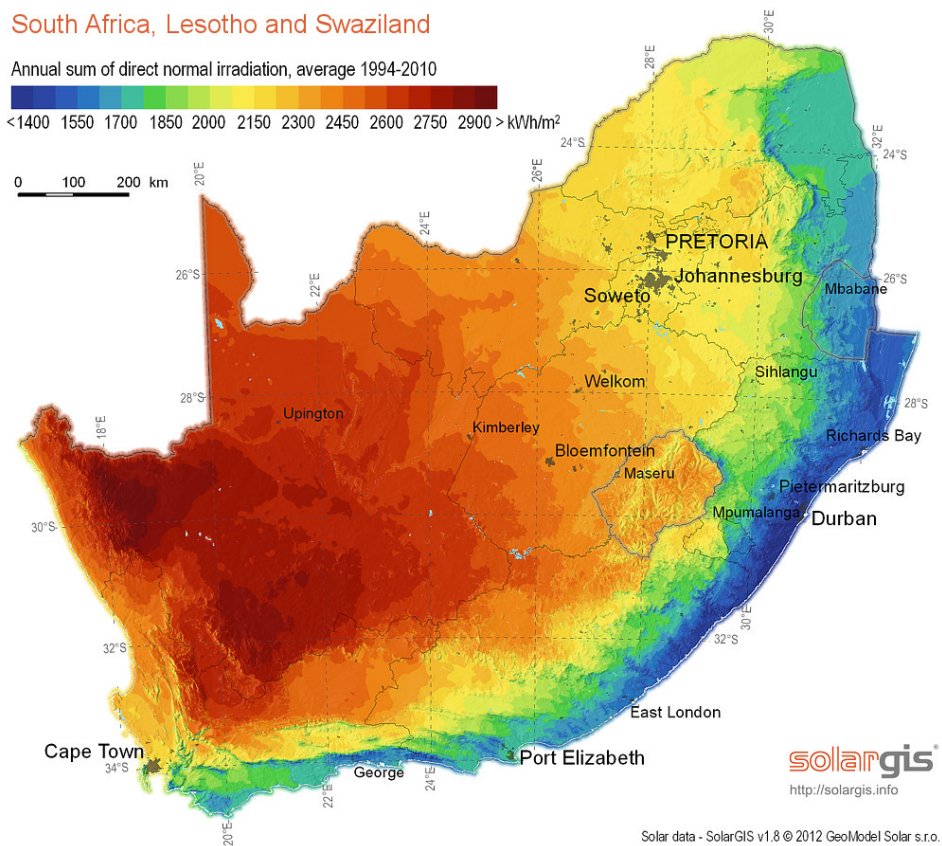


Figure F.1: DNI solar map of South Africa (GeoSUN AFRICA, 2012)

# G. Contact treatment method

## G.1 Determining which spheres are in contact

This section will explain how the contact points are determined in this study. The commercial DEM code generates the packed bed and exports the co-ordinates of each sphere to a data file in the following format.

Ball ID	Sphere Radius	X-coordinate	Y-coordinate	Z-coordinate
1.13169000000e+005	4.72470987400e-003	1.08983488608e-001	1.58125348437e-002	1.89461609243e-001
1.13170000000e+005	4.72470987400e-003	1.12089766446e-001	6.75688619471e-003	1.88449439110e-001
1.13171000000e+005	4.72470987400e-003	1.15253670761e-001	1.42883013510e-003	1.81081959833e-001
1.13172000000e+005	4.72470987400e-003	1.16621810427e-001	2.94958458062e-003	1.71674849622e-001
1.13173000000e+005	4.72470987400e-003	1.15392795522e-001	1.04281730252e-002	1.65738650496e-001
1.13174000000e+005	4.72470987400e-003	1.12286517683e-001	1.94838216745e-002	1.66750820629e-001
1.13175000000e+005	4.72470987400e-003	1.09122613369e-001	2.48118777337e-002	1.74118299906e-001

Figure G.1: DEM data file format example

A function written in Scilab determines the contact points and outputs a text file within a certain format that indicates which spheres are in contact. The format is produced in such a way so that the function written in Visual Basic can easily know when it must create a sphere and when it must apply a contact treatment method (cap or bridge). The following equation that can determine the distance between two points in a three dimensional space is used to determine the contact points between two spheres.

$$d_{xyz} = \sqrt{(X_1 - X_2)^2 + (Y_1 - Y_2)^2 + (Z_1 - Z_2)^2} \quad (\text{G.1.1})$$

If  $d_{xyz} - (R_1 + R_2) = 0$  we know that the spheres are in contact. However a certain tolerance is allowed because it was found that the spheres can interfere with each other giving a very small negative value. Also to eliminate small gaps, a minimum allowed distance is also specified. The Scilab code is shown in Listing J.2

Listing G.1: Scilab contact treatment function

```
function main()
//=====Inputs (file names)=====
A = read_csv('packed_bed_rxyz_DEM_coordinates.txt','\t')// reads data in matrix
fct = mopen('packed_bed_rxyz_CT_coordinates.txt','w')// opens contact file
[nr,nc] = size(A)// Determines the number of rows and columns in the array
limit = nr // search size
GAP = 0.0006 // [m] the minimum allowed gap between spheres
//=====
const = 0 // variable that counts contact points
```

```

sizem = nr
//=====
// Two loops – The first loop takes the first sphere and the second
// loop check every other sphere to determine if it is in contact
//=====
for i = 1:sizem
    r1 = strtod(A(i,1))
    x1 = strtod(A(i,2))
    y1 = strtod(A(i,3))
    z1 = strtod(A(i,4))

    upper = i + limit
    if upper >= sizem then
        upper = sizem
    end
    //Writes sphere coordinates to file
    fprintf(fct, '%s \t%s \t%s \t%s \t%s \t%s \t%s \n',
    A(i,1),A(i,2),A(i,3),A(i,4), '0', '0', '0', '0')
    for k = i+1: upper
        r2 = strtod(A(k,1))
        x2 = strtod(A(k,2))
        y2 = strtod(A(k,3))
        z2 = strtod(A(k,4))
        if r1>r2 then
            r=r1
        else
            r=r2
        end
        // Calculates the distance between two spheres
        d = sqrt((x1-x2).^2 + (y1-y2).^2 + (z1 - z2).^2)-(r1+r2)
        if (d >= -1*(0.008*r)) & (d<= (GAP)) then // Tolerance

            //Valid only for spheres
            conct = conct + 1 // Counts number of contact points
            Avg = conct/i // Works out avg number of contact points per particles

            //Writes which spheres are in contact to file
            fprintf(fct, '%s \t%s \t%s \t%s \t%s \t%s \t%s \t%s \n',
            A(i,1),A(i,2),A(i,3),A(i,4),A(k,1),A(k,2),A(k,3),A(k,4))
        end
    end
end
end
fclose(fct)
endfunction

```

The output file from the Scilab function is read into Microsoft excel where the function written in VBA can access the data. An example of the output data format is shown in Figure G.2. As seen in the figure, there are two sets of particle

	A	B	C	D	E	F	G	H
1	R1	X1	Y1	Z1	R2	X2	Y2	Z2
2	0.011069	-0.04121	0.002948	0.219881	0	0	0	0
3	0.011069	-0.04121	0.002948	0.219881	0.011069	-0.02593	0.018602	0.216478
4	0.011069	-0.04121	0.002948	0.219881	0.011069	-0.02811	-0.01377	0.213463
5	0.011069	-0.04121	0.002948	0.219881	0.011069	-0.044	0.017809	0.203712
6	0.011069	-0.04121	0.002948	0.219881	0.011069	-0.04135	-0.0036	0.198734
7	0.011069	0.07837	0.010253	0.219457	0	0	0	0
8	0.011069	0.07837	0.010253	0.219457	0.011069	0.06041	0.02205	0.214135
9	0.011069	0.07837	0.010253	0.219457	0.011069	0.064853	0.002259	0.203854
10	0.011069	0.07837	0.010253	0.219457	0.011069	0.0866	-0.00173	0.20275

Figure G.2: Contact treatment file format example

coordinates next to each other. The function written in VBA knows that when the second set of coordinates (R2, X2, Y2 and Z2) are all zero, it must just create a sphere with radius R1 at the coordinates X1, Y1 and Z1. For the case where the second set of coordinates is non-zero, the function will create either a bridge that stretches between two spheres in contact or cap the spheres. The code written in VBA is not presented here because of space restrictions but is available on request to the author. A screen shot of the program interface however is shown in Figure G.3

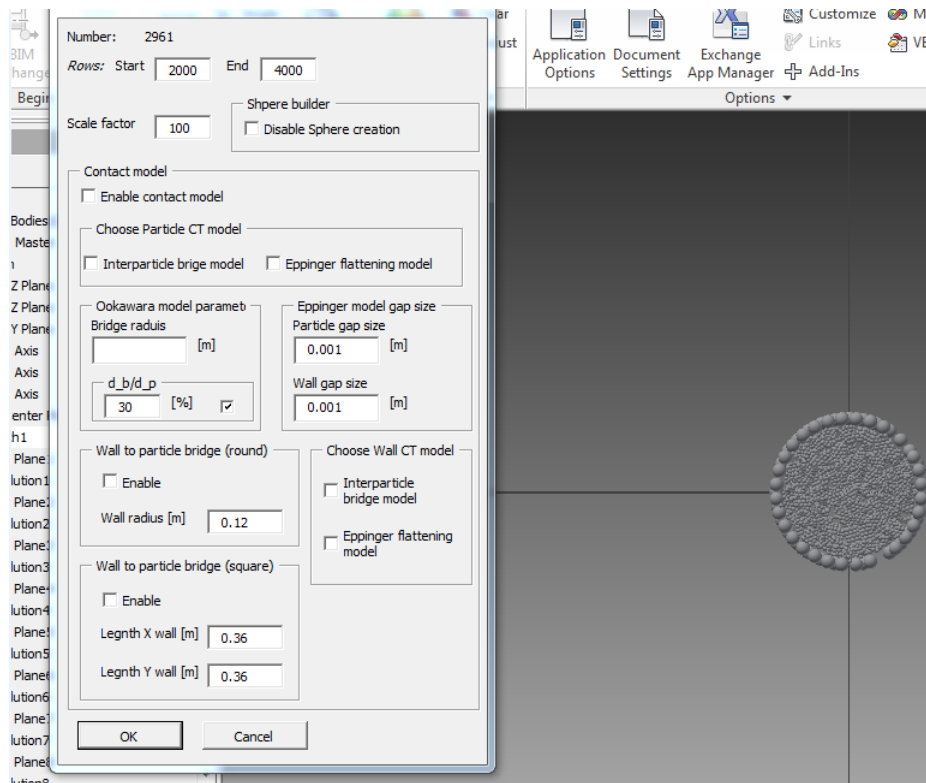


Figure G.3: VBA interface

# H. Cone rock bed TES

## H.1 Cone rock bed TES parameters

The size of the TES system investigated was required to supply 30 hours' worth of thermal energy for a 100 MW<sub>e</sub> steam power cycle. The thermal to electric efficiency ( $\eta_{th}$ ) for the steam power cycle will be assumed to be 30%. Therefore the storage system needed to supply 333 MW<sub>th</sub>. The air temperature was supplied from the rock bed at 560°C, the ambient temperature was assumed to be 25°C. The required mass flow rate was 606 kg/s.

The thermal energy that the bed was required to store was  $36 \times 10^3$  GJ. The global porosity of the bed was assumed to be 0.44. The rock type used was dolerite with a density of 2819 kg/m<sup>3</sup>, a heat capacity of 839 J/kgK and a conductivity of 2 W/mK. The rock properties are assumed to be constant and not dependent on temperature. The volume heat capacity of the rock was 2.365 MJ/m<sup>3</sup>K and the apparent volume heat capacity of the rock bed taking the porosity into account was 1.32 MJ/m<sup>3</sup>K. The minimum required volume needed to store the required energy was 50804 m<sup>3</sup>.

To minimize the losses from the bed, it was essential that the outlet air temperature not exceed 1°C above the ambient temperature. A simple geometry analysis given in Section H.2, estimated that only a certain percentage of the bed would be utilised, and this was dependent on the length of the solid wall section of the inlet shaft. For this investigation we will choose that the height of the perforated shaft is 20% of the total height of the bed. This results in an estimated volume efficiency of 48.52%. This means that the minimum required bed volume became 104707.34 m<sup>3</sup>. The minimum volume required was multiplied by a safety factor of 2.4 in order to ensure 1) that the outlet temperature remained below the minimum of 1 K above ambient temperature and 2) that the active region in the bed was protected against the environment by a sufficiently large layer of rocks. This safety factor was a guess and the simulations were performed to determine its validity. The storage dimensions are given in Table H.1.

The Cone rock bed is intended to be implemented in the SUNSPOT cycle and therefore will be charged during the day by the exhaust gas from the gas turbine power cycle. For the purpose of this investigation, it was assumed that a gas turbine with similar characteristics to those at the Ankerlig power station would be used. The exhaust gas information for the Ankerlig turbine is given in Table H.2

Table H.1: Pyramid TES dimensions

Y (bed height) [m]	48.14
R (bottom radius) [m]	67.72
r (top radius) [m]	6.1
Rock pile angle [deg]	38
Volume [m <sup>3</sup> ]	248231

(Eskom, 2013). It was also assumed that the turbine would charge the rock bed at full load for 8 hours. This assumption is valid due to the auxiliary fuel supply that can add energy in the case of bad weather periods or insufficient solar energy. To charge the bed with enough energy, a mass flow rate of 2272 kg/s was required (1250 MW<sub>th</sub>). Assuming that the Ankerlig turbine can be linearly scaled up, this means that the gas turbine produces 650 MW<sub>e</sub>.

Table H.2: Ankerlig gas turbine exhaust data (Eskom, 2013)

Power	150 MW <sub>e</sub>
Exhaust gas temperature	560°C
Mass flow rate	520 kg/s

The particle size for the rock bed is an important parameter to choose for optimal bed performance. The particle size influences the thermal performance of the bed as well as the pumping power required. Small particles result in larger pressure drops but better thermal stratification. Allen (2010) notes that smaller particles allow for shorter packing lengths due to the enhanced thermal stratification, and therefore the pumping power may be comparable with beds containing larger particles but with better extraction of useful energy. Furthermore, the study mentions that the ratio of useful energy over pumping power is smallest for small particles and increases with particle size. Hänchen *et al.* (2010) note that although smaller particles result in much higher pumping power, the overall efficiency reaches its maximum for the smallest particles due to the more efficient energy extraction. The particle size that is used in this study model was 0.05m.

The flow rate also plays a role in thermal stratification and pumping power. According to Hänchen *et al.* (2010), a flow rate of 0.08 kg/m<sup>2</sup>s results in the best overall efficiency. As mentioned Allen (2010) recommends a flow rate below 0.2 kg/m<sup>2</sup>s.

## H.2 Simple Cone rock bed storage system geometry analysis

Figure H.1 shows a simple two dimensional representation of the Cone TES system. The length of the solid wall section of the inlet shaft is represented by  $h$  and the total height of the storage system is given by  $Y$ . The length of the perforated

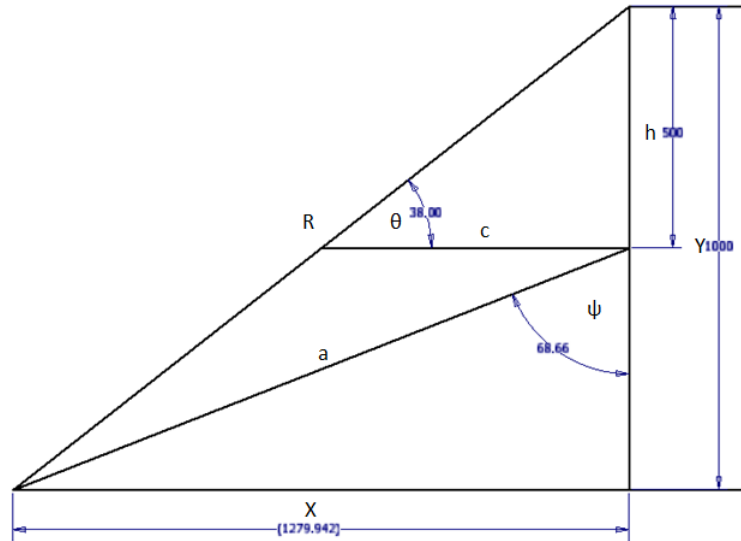


Figure H.1: Pyramid geometry analysis (Autodesk Inc., 2012)

portion of the shaft is equal to  $Y - h$ . The flow path length from the top point of the perforated section of the shaft to the Cone's outer surface is represented by  $a$ .  $\theta$  is the angle repose and  $\Psi$  is the variable angle of the flow path. The length of the flow path,  $a$ , can be calculated by

$$a = \frac{c \sin(180 - \theta)}{\sin(\theta + \Psi - 90)} \text{ for } \Psi_{\min} \leq \Psi \leq 180^\circ \quad (\text{H.2.1})$$

where

$$c = \frac{h}{\tan \theta} \quad (\text{H.2.2})$$

and the minimum value of  $\Psi$  is equal to

$$\Psi_{\min} = \arcsin\left(\frac{X}{\sqrt{X^2 + (Y - h)^2}}\right) \quad (\text{H.2.3})$$

Figure H.2 shows the ratio of the flow path length over  $h$  versus  $\Psi$  for four different values of  $h$ . It is seen that as the  $h/Y$  increases the maximum value of  $a/h$  decreases. From all four graphs it is seen that  $a/h = 1$  at  $104^\circ$  and  $180^\circ$  and the minimum flow path length is equal to  $0.788h$  at  $142^\circ$ . It is expected that the largest portion of the flow will exit the bed in the region of  $104^\circ \leq \Psi \leq 180^\circ$  with the maximum flow rate at  $\Psi = 142^\circ$ .

For the purpose of sizing the storage we will assume that all of the flow will only exit in the region of the  $104^\circ \leq \Psi \leq 180^\circ$ . This assumption surely underestimate the region through which the fluid flows and will be seen as a conservative assumption. Figure H.3 shows the so called 'Active region' and 'Dead region' of

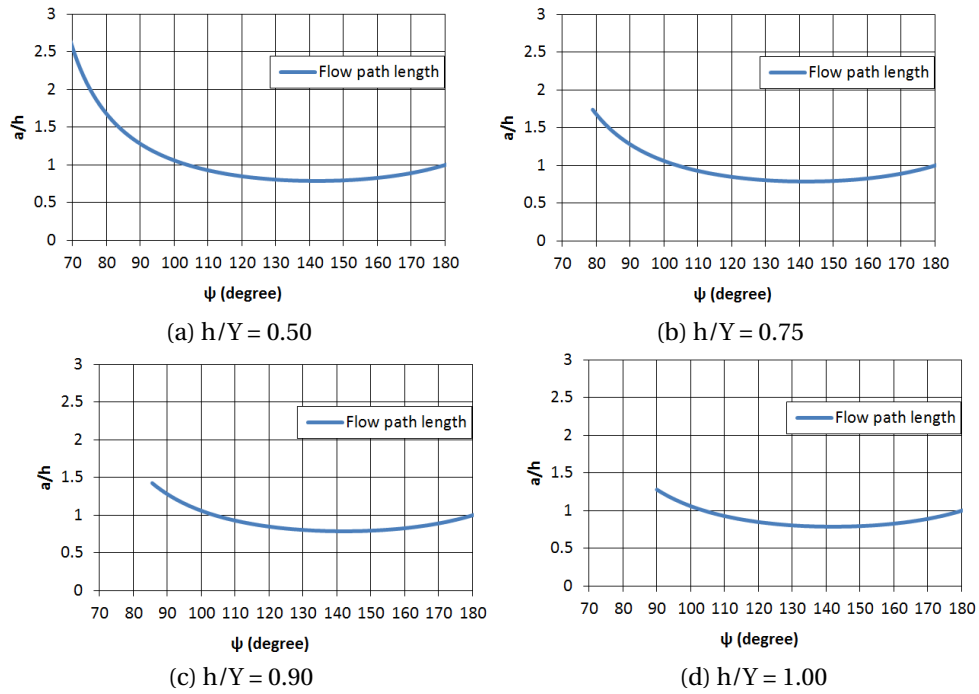


Figure H.2: Pyramid flow path length

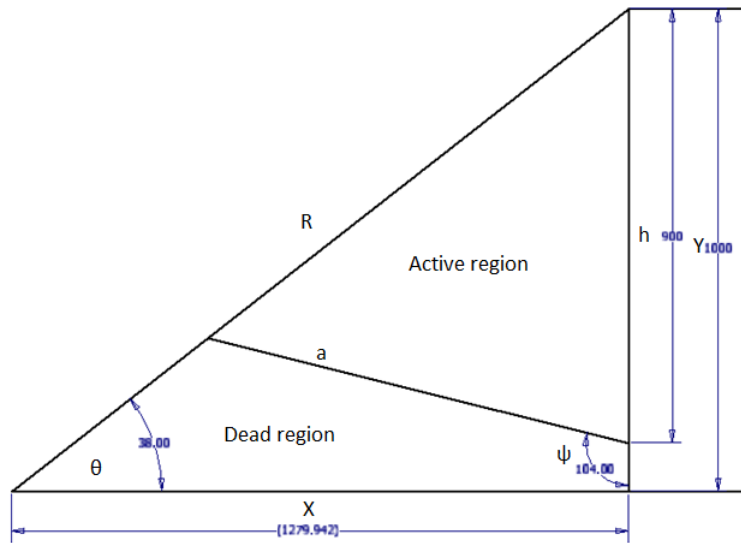


Figure H.3: Pyramid geometry active region Autodesk Inc. (2012)

the TES, based on the previously mentioned assumption. The storage volume efficiency ( $\eta_{Vol}$ ) is defined as the active region over the total available storage volume and, assuming that the bed is symmetrical is calculated by

$$\eta_{Vol} = \frac{h^2 \sin(\theta) \cos(\theta)}{0.5XY} \tag{H.2.4}$$

Figure H.4 shows how the TES volume efficiency increases with increasing  $h/Y$ . The maximum that can reach efficiency is equal to 75.8% for  $\theta = 38^\circ$ . The TES

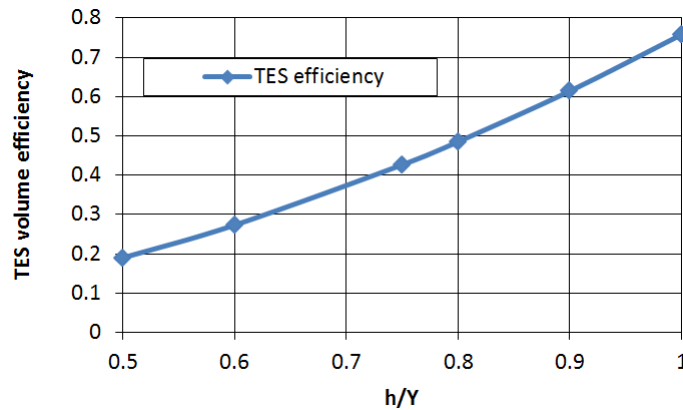


Figure H.4: Pyramid TES efficiency

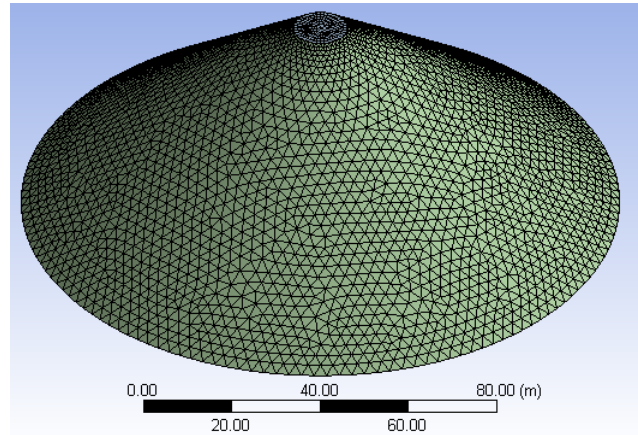
volume efficiency given in Figure H.4 is used as an initial Cone storage size estimating tool. It was assumed here that the flow will choose the path of least resistance to flow from the center of the bed to the outside, which is the shortest path. This assumption may not be valid, because the increasing flow area size must also be taken into account.

### H.3 CFD model setup

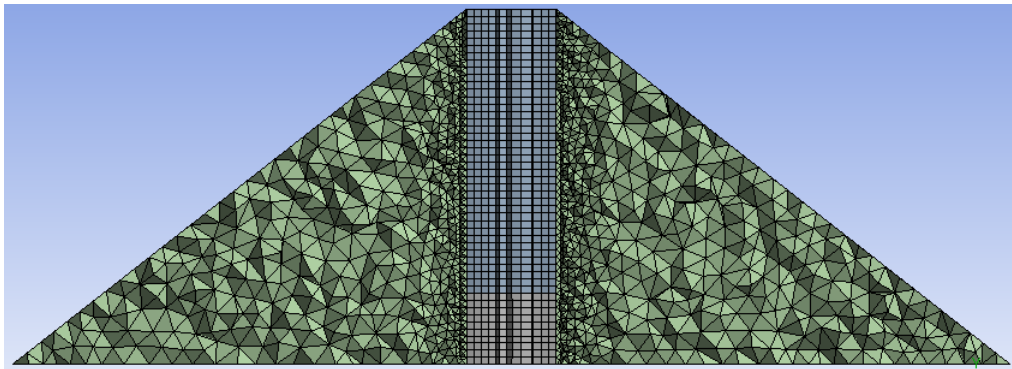
The mesh for the Cone rock bed porous model is shown in Figure H.5. A hybrid mesh was used to create the computational domain. The central shaft used a structured mesh and the rock bed section used an unstructured tetrahedral mesh. The mesh size used was relatively coarse to minimize computational cost. A large pressure drop gradient and velocity gradient was expected in the region closely surrounding the perforated section of the pipe, therefore the mesh at the interface between the perforated pipe section and rock bed was finer. Because the flow area of the rock bed increases as the fluid flows to the outer surface, a large pressure gradient was not expected in the bulk of the rock bed. Prism layers on the wall of the central shaft were excluded to keep the mesh size to a minimum. The friction resulting from the shafts surface was considered to be negligible compared to the pressure drop through the rock bed, and therefore it was not necessary to model it accurately. The size of the mesh is 170 208 elements.

In the shaft region the realizable  $k - \epsilon$  turbulence model with the enhanced wall function was used. Turbulence was not modelled within the packed bed. The boundary condition of the surface of the rock bed was set as a "pressure-outlet" during the charging cycle and as a "pressure-inlet" during the discharge cycle. The "pressure-outlet" and "pressure-inlet" boundary was set at 0 Pa gauge

pressure and 298 K. The shaft inlet boundary condition was set as a "mass-flow-inlet" during charging and discharging cycles. During the discharging cycle the flow direction was set to "outward-normal-boundary". The heat transfer correlation of Chandra and Willits (1981) was used, and the friction factor correlation of Singh *et al.* (2006) was used in the porous model.



(a) Mesh



(b) Mesh cross section

Figure H.5: Cone rock bed mesh

# I. Sample calculations

## I.1 Pressure drop

To calculate the friction factor ( $f$ ) as given in Equation 3.2.19, the input data given in Table I.2 was used.

Table I.1: Pressure drop calculation input data

$\Delta P_{CFD}$	692.0 Pa
$\epsilon$	0.3907
L	0.301671 m
$U_0$	2.1 m/s
$\sum A_p$	2.46552192 m <sup>2</sup>
$\sum V_p$	0.01232761 m <sup>3</sup>
$\rho_f$	1.1768 kg/m <sup>3</sup>
$\mu_f$	$1.8532 \times 10^{-5}$ kg/ms

The Specific surface area  $S_v = \sum A_p / \sum V_p = 200 \text{ m}^{-1}$  and the equivalent particle diameter based on,  $S_v$ , is  $d_{p_{Sv}} = 6/S_v = 0.03 \text{ m}$ . The particle Reynolds number is  $Re_p = U_0 \rho_f d_{p_{Sv}} / \mu_f = 4000.75$  and Allen's Reynolds Number is  $Re_2 = 4U_0 \rho_f \sum A_p / \mu_f (1 - \epsilon) \sum V_p = 4377.36$ . Noting that  $Re_2 = 4 \cdot Re_1 = (2/3) \cdot Re_{Erg} = (2/3) \cdot Re_p / (1 - \epsilon)$ . The friction factor for the CFD results is calculated by

$$f_{CFD} = \frac{\Delta P_{CFD}}{L} \frac{\epsilon^3}{(1 - \epsilon) \rho U_0^2} \frac{\sum V_p}{\sum A_p} = 0.2163 \quad (\text{I.1.1})$$

The friction factor as given in Equation 3.2.20 is equal to

$$f = f_{Allen} = \frac{22.4}{Re_2} + \frac{0.546}{Re_2^{0.12}} = 0.2014 \quad (\text{I.1.2})$$

The friction factor as given in Equation 3.2.13 is equal to

$$f = f_{Carman} = \frac{5}{Re_1} + \frac{0.4}{Re_1^{0.1}} = \frac{5}{(Re_2/4)} + \frac{0.4}{(Re_2/4)^{0.1}} = 0.2032 \quad (\text{I.1.3})$$

The friction factor as given in Equation 3.2.24 is equal to

$$f = f_{\text{KTA}}/12 = \left( \frac{320}{\frac{Re_p}{1-\epsilon}} + \frac{6}{\frac{Re_p}{1-\epsilon}^{0.1}} \right) / 12 = \frac{26.67}{[(3/2) \cdot Re_2]} + \frac{0.5}{[(3/2) \cdot Re_2]^{0.1}} = 0.2117 \quad (\text{I.1.4})$$

The Ergun friction factor is equal to

$$f = f_{\text{Erg}}/6 = \left( \frac{150}{Re_{\text{Erg}}} + 1.175 \right) / 6 = \frac{25}{[(3/2) \cdot Re_2]} + 0.2917 = 0.2938 \quad (\text{I.1.5})$$

## I.2 Heat transfer

To calculate the Nusselt number ( $Nu$ ) for flow through a packed bed with a constant particles surface temperature, the input data given in Table I.2 was used.

Table I.2: Heat transfer calculation input data

$T_{\text{in}}$	300 K
$T_{\text{ps}}$	400 K
$T_{\text{out}}$	395.41 K
$\epsilon$	0.3907
L	0.301671 m
G	0.72022 kg/m <sup>2</sup> s
$\sum A_p$	2.46552192 m <sup>2</sup>
$\sum V_p$	0.01232761 m <sup>3</sup>

The Specific surface area  $S_v = \sum A_p / \sum V_p = 200 \text{ m}^{-1}$  and the equivalent particle diameter based on,  $S_v$ , is  $d_{p_{sv}} = 6/S_v = 0.03 \text{ m}$ . The specific surface area of the bed,  $a_{sf} = S_v(1 - \epsilon) = 121.82 \text{ m}^{-1}$ .

The average air properties in the packed bed section are:  $\mu_f = 2.155 \times 10^{-5} \text{ kg/ms}$ ;  $\rho_f = 1.009 \text{ kg/m}^3$ ;  $k_f = 0.0309 \text{ W/mK}$ ;  $c_p = 1009.26 \text{ J/kgK}$ ;  $Pr = \mu_f c_p / k_f = 0.708$ . The particle Reynolds number,  $Re_p = U_0 \rho_f d_{p_{sv}} / \mu_f = G d_{p_{sv}} / \mu_f = 999.425$ .

Wakoa *et al.* (1979) calculate the heat transfer coefficient for a steady state packed bed with constant particle surface temperature by solving the steady state energy balance equation (Equation I.2.1) of flow through a packed bed.

$$u \frac{dT_f}{dx} + \frac{ha_{sf}}{\epsilon c_f \rho_f} (T_f - T_{ps}) = \alpha_{ax} \frac{d^2 T_f}{dx^2} \quad (\text{I.2.1})$$

The axial thermal dispersion through a packed bed is defined as

$$\alpha_{ax} = \frac{k_{\text{eff}}}{\epsilon c_f} \rho_f + 0.5 d_p u \quad (\text{I.2.2})$$

The Danckwerts boundary conditions are used and are shown below (Wakoa *et al.*, 1979)

$$u(T_f - T_0) = \alpha_{ax} \frac{dT_f}{dx} \text{ at } x = 0 \quad (\text{I.2.3})$$

$$\frac{dT_f}{dx} = 0 \text{ at } x = L \quad (\text{I.2.4})$$

(Wakoa *et al.*, 1979) solves for Equation I.2.1 and the solution is presented below

$$\frac{T_{ps} - T_{out}}{T_{ps} - T_{in}} = \frac{4Ae^{\left[\frac{uL}{2\alpha_{ax}}\right]}}{(1+A)^2 e^{\left[A\frac{uL}{2\alpha_{ax}}\right]} - (1-A)^2 e^{\left[A\frac{uL}{2\alpha_{ax}}\right]}} \quad (\text{I.2.5})$$

where

$$A = \sqrt{1 + \frac{4a_{sf}h\alpha_{ax}}{\varepsilon u^2 c_f \rho_f}} \quad (\text{I.2.6})$$

When the axial thermal dispersion is neglected, Equation I.2.5 reduces to

$$\frac{T_{ps} - T_{out}}{T_{ps} - T_{in}} = EXP \left[ -\frac{a_{sf}hL}{\varepsilon u c_f \rho_f} \right] \quad (\text{I.2.7})$$

Equation I.2.7 can be rewritten as

$$h = \frac{Gc_f}{a_{sf}L} \ln \left[ \frac{T_{ps} - T_{in}}{T_{ps} - T_{out}} \right] \quad (\text{I.2.8})$$

The heat transfer coefficient and Nusselt number from the CFD results were calculated by,

$$h_{CFD} = \frac{Gc_f}{a_{sf}L} \ln \left[ \frac{T_{ps} - T_{in}}{T_{ps} - T_{out}} \right] = 60.95 \text{ W/m}^2\text{K} \quad (\text{I.2.9})$$

$$Nu_{CFD} = \frac{d_{psv} h_{CFD}}{k_f} = 59.32 \quad (\text{I.2.10})$$

The Nusselt number correlation as given in Wakoa *et al.* (1979) is equal to

$$Nu = 2 + 1.1Pr^{1/3}Re_p^{0.6} = 65.89 \quad (\text{I.2.11})$$

The Nusselt number correlation as given in Nuclear Safety Standards Commission (KTA) (1983) is equal to

$$Nu = 1.27 \frac{Pr^{1/3}}{\varepsilon^{1.18}} Re_p^{0.36} + 0.33 \frac{Pr^{1/2}}{\varepsilon^{1.07}} Re_p^{0.86} = 70.05 \quad (\text{I.2.12})$$

The Nusselt number correlation as given in L of and Hawley (1948) is equal to

$$h = h_v/a_{fs} = 5.35 \frac{G}{d_{p_{sv}}}^{0.7} = 49.49 \text{ W/m}^2\text{K} \quad (\text{I.2.13})$$

$$Nu = \frac{hd_{p_{sv}}}{k_f} = 53.50 \quad (\text{I.2.14})$$

The Nusselt number correlation as given in Chandra and Willits (1981) is equal to

$$Nu = Nu_v/6(1 - \varepsilon) = \frac{1.45}{6(1 - \varepsilon)} \frac{Gd_{p_{sv}}^{0.7}}{\mu_f} = 50.03 \quad (\text{I.2.15})$$

## J. Porous media

### J.1 Pressure source term UDF

The following will demonstrate how the coefficients  $\frac{1}{\alpha}$  and  $C_2$  (see Equation 3.3.6) are determined from the Ergun and Carman type equations. The porous media momentum source term is shown again here for convenience.

$$S_{M_i} = - \left( \frac{\mu}{\alpha} u_i + C_2 \frac{1}{2} \rho |u| u_i \right) \quad (J.1.1)$$

It is clear that the source term is a Forchheimer type equation with  $n$  equal to 2 which is similar to the Ergun equation. It can be easily shown that if we substitute Equations 3.2.7 and 3.2.8 into Equation 3.2.6 and compare it with Equation 3.3.6 that  $\frac{1}{\alpha}$  and  $C_2$  are equal to

$$\frac{1}{\alpha} = \frac{K_1(1-\epsilon)^2}{d_p^2 \epsilon^3} \quad (J.1.2)$$

$$C_2 = \frac{K_2(1-\epsilon)}{d_p \epsilon^3} \quad (J.1.3)$$

If we compare a Carman type equation (Eq. 3.2.14) to 3.3.6 it can be shown that  $\frac{1}{\alpha}$  and  $C_2$  are equal to

$$\frac{1}{\alpha} = \frac{5S_v^2(1-\epsilon)^2}{\epsilon^3} \quad (J.1.4)$$

$$C_2 = \frac{0.4S_v^{1.1}(1-\epsilon)^{1.1}}{\epsilon^3} \cdot \left( \frac{\mu}{\rho U_0} \right)^{0.1} \quad (J.1.5)$$

we can write  $\frac{1}{\alpha}$  and  $C_2$  in a more general term.

$$\frac{1}{\alpha} = \frac{K_3 S_v^2 (1-\epsilon)^2}{\epsilon^3} \quad (J.1.6)$$

$$C_2 = \frac{K_4 S_v (1-\epsilon)}{\epsilon^3} \cdot \left( \frac{S_v (1-\epsilon) \mu}{\rho U_0} \right)^{2-n} \quad (J.1.7)$$

Listing J.1: UDF example for viscous resistance coefficients

```

/* Viscous Resistance Profile UDF in a Porous Zone that utilizes F_PROFILE*/
#include "udf.h"
DEFINE_PROFILE(vis_res , t , i)
{
    real x[ND_ND], a, porosity, dp;
    real K3;
    cell_t c;

    begin_c_loop(c, t) /*to loop over each cell in the zone*/
    {
        K3 = 5
        dp = 0.05; /*particle size based on*/
        porosity = 0.4; /*The packed bed porosity*/

        C_CENTROID(x, c, t);

        a = (22.4/4.0)*(pow((1.0 - porosity), 2.0)/pow(porosity, 3.0))*(36.0/pow(dp, 2.0));

        F_PROFILE(c, t, i) = a;
    }
end_c_loop(c, t)
}

```

Listing J.2: UDF example for Inertial resistance coefficients

```

/* Inertial Resistance Profile UDF in a Porous Zone that utilizes F_PROFILE*/
DEFINE_PROFILE(inertial_res_x , t , i)
{
    real x[ND_ND], a, mu, R, U, porosity, re, dp;
    real K4, n, z;
    cell_t c;

    begin_c_loop(c, t) /*to loop over each cell in the zone*/
    {
        K4 = 0.4
        n = 1.9
        dp = 0.05; /*particle size based on*/
        porosity = 0.4; /*The packed bed porosity*/

        R = C_R(c, t); /* fluid density*/
        U = pow((C_U(c, t)*C_U(c, t)), 0.5); /*x-velocity absolute*/
        mu = C_MU_L(c, t); /* fluid viscosity

        C_CENTROID(x, c, t);

        re = ((1.0*U*R)/(mu*(1-porosity)))*(dp/6.0); /*Reynolds number Re1*/
        z = 2-n;
        if (re == 0.0 ) /*to ensure no zero division*/
            a = 0.0;
        else
        {
            /*C2*/
            a = (0.4/0.5)*(1.0/pow(re, z))*
                (pow((1.0 - porosity), 1.0)/pow(porosity, 3.0))*(6/pow(dp, 1.0));
        }
        F_PROFILE(c, t, i) = a;
    }
end_c_loop(c, t)
}

```

## K. Sauna test facility

The experimental rock bed test facility at the University of Stellenbosch referred to as the Sauna is briefly described here. The basic components of the Sauna are the blower, diesel burner and rock bed test section. Photographs of the system are shown in Figures K.3 to K.6. The rock bed test section is illustrated in Figure K.1.

### K.1 Sauna

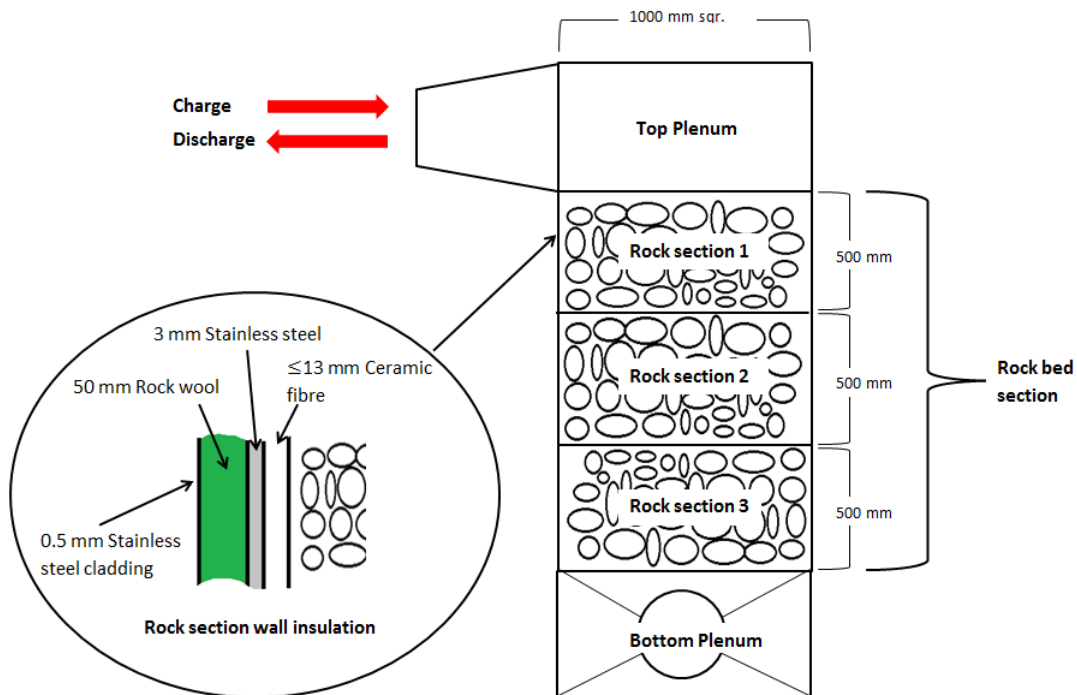


Figure K.1: Illustration of the Sauna

The Sauna rock bed test section is constructed out of stainless steel and insulated with rock wool. The inside of the rock bed section of the Sauna has an additional layer of ceramic fibre insulation, mainly to eliminate wall channelling.

The conductivity of stainless steel, the rock wool and ceramic fibre as given by the manufacturers is shown in Figure K.2. The ceramic fibre lines the inside of

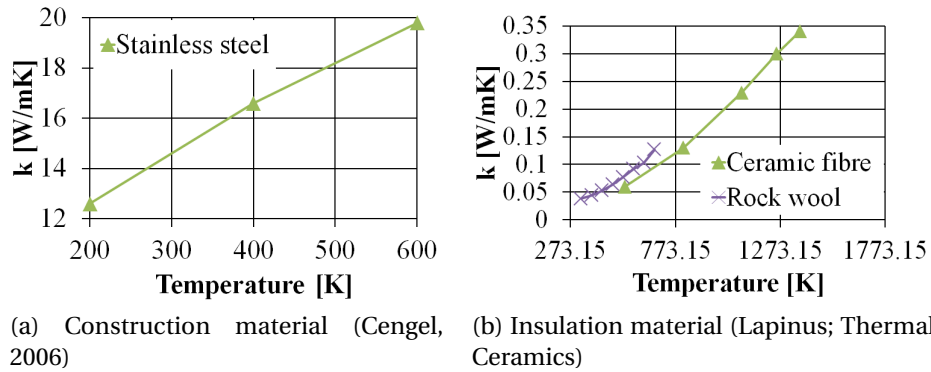


Figure K.2: Sauna insulation

the bed and is compressed by the rocks in contact with the walls. Therefore the thickness of the material varies as parts are compressed to a very small thickness. This study assumed that the average thickness of the material could be calculated from the following equation

$$t_{\text{ins}_{\text{avg}}} = t_{\text{ins}_{\text{max}}} \times \varepsilon \quad (\text{K.1.1})$$

where  $t_{\text{ins}_{\text{avg}}}$  and  $t_{\text{ins}_{\text{max}}}$  are the average and maximum material thicknesses respectively. The equation assumes that the bed's porosity is homogenous and that the surface porosity of the outer rock layer is equal to the beds porosity. From the literature review we know that the porosity oscillates in the region near a wall and that for spheres the porosity equals unity at the wall. However, due to the irregular shape of rocks (flat surfaces) it was expected that the porosity was possibly not unity at the wall, but somewhere in between unity and the beds average porosity. This assumption was expected to under estimate the insulation average thickness.

The thermal resistance was calculated from the Equation K.1.2.

$$R_{\text{series @ 410K}} = \frac{t_{\text{Rock wool}}}{k_{\text{Rock wool}}} + \frac{t_{\text{SST}}}{k_{\text{SST}}} + \frac{t_{\text{Ceramic fibre}}}{k_{\text{Ceramic fibre}}} = 1.362 \text{ K/W m}^2 \quad (\text{K.1.2})$$

$$\rightarrow k_{\text{effective}} = \frac{t_{\text{Total}}}{R_{\text{series @ 410K}}} = 0.0519 \text{ W/mK} \quad (\text{K.1.3})$$

Not shown in Figure K.1 are two perforated plates located in the top and bottom plenums of the Sauna. These plates are positioned at an angle of  $64^\circ$  and have a 25.45% open area. The purpose of the perforated plates is to ensure that the flow coming in from a right angle is evenly distributed over the rock bed inlet. The rocks in the rock bed section are supported on a steel grid.

Temperature measurements are taken at five positions in the bed. The positions are the top plenum, rock section one, rock section two, rock section three

and bottom plenum. Six thermocouples are used at each position in the test section. The thermocouples of rock section one, two and three are positioned at 200 mm, 700 mm and 1250 mm taken from the top surface of rock section one respectively. The pressure measurements are taken at the top and bottom plenums in order to determine the pressure drop over the test section. The pressure sensors are positioned roughly between 100-200 mm away from the top and bottom rock surfaces. The mass flow rate is measured with a bell mouth (see Figures K.5) at the inlet of the blower and a orifice plate (see Figures K.6) positioned in the outlet exhaust duct (Allen, 2012).



Figure K.3: Sauna diesel burner and blower view



Figure K.4: Sauna diesel tank and measuring and control equipment view



Figure K.5: Sauna bell mouth



Figure K.6: Sauna orifice plate

## List of References

- Al-nimr, M.A., Abu-qudais, M.K. and Mashaqi, M.D. (1996). Dynamic behaviour of a packed bed energy storage system. *Energy convers*, vol. 37, pp. 23–30.
- Allen, K., von Backström, T. and Kröger, D. (2012). Packed beds of rock for thermal storage. In: *SASEC*.
- Allen, K.G. (2010). *Performance characteristics of packed bed thermal energy storage for solar thermal power plants*. Master's thesis, Department of Mechanical and Mechatronic Engineering University of Stellenbosch.
- Allen, K.G. (2012). Personal communication between Allen, K. G. and Louw, A. D. R.
- Atmakidis, T. and Kenig, E. (2009). CFD-based analysis of the wall effect on the pressure drop in packed beds with moderate tube/particle diameter ratios in the laminar flow regime. *Chemical Engineering Journal*, vol. 155, pp. 404–410.
- Augier, F., Idoux, F. and Delenne, J. (2010). Numerical simulation of the transfer and transport properties inside packed beds of spherical particles. *Chemical Engineering Science*, vol. 65, pp. 1055–1064.
- Autodesk Inc. (2012). *Autodesk Inventor Professional 2013*. Autodesk Inc., San Rafael, CA, United States.  
Available at: <http://www.autodesk.com>
- Auwerda, G.J., Kloosterman, J.L., Winkelman, A.M., Groen, J. and van Dijk, V. (2010). Comparison of experiments and calculations of void fraction distributions in randomly stacked pebble beds. *PHYSOR*.
- Bai, H., Theuerkauf, J. and Gillis, P. (2009). A coupled DEM and CFD simulation of flow field and pressure drop in fixed bed reactor with randomly packed catalyst particles. *Ind. Eng. Chem. Res.*, vol. 48, pp. 4060–4074.
- Baker, M. and Tabor, G. (2010). Computational analysis of transitional air flow through packed columns of spheres using the finite volume technique. *Computers and Chemical Engineering*, vol. 34, pp. 878–885.
- Banks, D. and Schäffler, J. (2006). The potential contribution of renewable energy in South Africa. Tech. Rep., Johannesburg: Sustainable Energy & Climate Change Project, Earthlife Africa.

- Bauer, R. (1990). *Hemisphere Handbook of Heat Exchanger Design*. Hemisphere Publishing Corporation.
- Bejan, A. and Nield, D.A. (2006). *Convection in porous media 3rd edition*. Springer.
- Britannica (2013). Encyclopedia Britannica online academic edition, database. Online. (accessed 20 July 2013).  
Available at: <http://www.britannica.com/EBchecked/topic/160909/diabase>
- Calis, H.P.A., Nijenhuis, J., Paikert, B.C., Dautzenberg, F.M. and van den Bleek, C.M. (2001). CFD modelling and experimental validation of pressure drop and flow profile in a novel structured catalytic reactor packing. *Chemical Engineering Science*, vol. 56, pp. 1713–1720.
- Carman, P. (1937). Fluid flow through granular beds. *Institution of Chemical Engineers*, vol. 15, pp. 150–166.
- Cengel, Y. and Cimbala, J. (2006). *Fluid mechanics Fundamentals and Applications*. McGrawHill.
- Cengel, Y.A. (2006). *Heat and Mass Transfer: A practice approach*. McGra.
- Chandra, P. and Willits, D. (1981). Pressure drop and heat transfer characteristics of air-rockbed thermal storage systems. *Solar Energy*, vol. 24, pp. 547–553.
- Coussirat, M., Guardo, A., Mateos, B. and Egusquiza, E. (2007). Performance of stress-transport models in the prediction of particle-to-fluid heat transfer in packed beds. *Chemical engineering science*, vol. 62, pp. 6897–6907.
- Coutier, J. and Farber, E. (1982). Two applications of a numerical approach of heat transfer process within rock beds. *Solar Energy*, vol. 29, pp. 451–462.
- Deissler, R. and Boegli, J. (1958). An investigation of effective thermal conductivities of powders in various gases. *ASME Transactions*, vol. 80, pp. 1417–1425.
- Delele, M. A., Tijsskens, E., Atalay, Y. T., Ramon, H., Nicolai, B. M. and Verboven, P. (2008). Combined discrete element and CFD modelling of air flow through random stacking of horticultural products in vented boxes. *Journal of food engineering*, vol. 89, pp. 33–41.
- Dixon, A., Nijemeisland, M. and Stitt, E. (2013). Systematic mesh development for 3D CFD simulation of fixed beds: Contact points study. *Computers and Chemical Engineering*, vol. 48, pp. 135–153.
- Dixon, A.G. (1988). Correlation for wall and particle shape effects on fixed bed bulk voidage. *Canadian Journal of Chemical Engineering*, vol. 66, pp. 705–708.
- Dixon, A.G. and Nijemeisland, M. (2001). CFD as a design tool for fixed-bed reactors. *Ind. Eng. Chem.*, vol. 40, pp. 5246–5254.

- Dixon, A.G., Nijemeisland, M. and Stitt, E.H. (2006). Packed tubular reactor modeling and catalyst design using computational fluid dynamics. *Advances in Chemical Engineering*, vol. 31, pp. 307–389.
- Dixon, A.G., Taskina, M.E., Nijemeisland, M. and Stitt, E.H. (2011). Systematic mesh development for 3D CFD simulation of fixed beds: Single sphere study. *Computers and Chemical Engineering*, vol. 35, pp. 1171–1185.
- Dixon, A.G., Walls, G., Stanness, H., Nijemeisland, M. and Stitt, E.H. (2012). Experimental validation of high reynolds number CFD simulations of heat transfer in a pilot-scale fixed bed tube. *Chemical Engineering Journal*, vol. 200, pp. 344–356.
- Eisfeld, B. and Schnitzlein, K. (2001). Influence of confining walls on the pressure drop in packed beds. *Chemical engineering science*, vol. 56, pp. 4321–4329.
- Eppinger, T., Seidler, K. and Kraume, M. (2010). DEM-CFD simulations of fixed bed reactors with small tube to particle diameter ratios. *Chemical Engineering Journal*, vol. 166, pp. 324–331.
- Ergun, S. (1952). Fluid flow through packed columns. *ChemProg*, vol. 48, pp. 89–94.
- Eskom (2013). Ankerlig and Gourikwa gas turbine power stations. *Fact Sheet*, pp. 1–14.
- Fluent (2011a). *Fluent Theory guide version 14.0*. ANSYS.
- Fluent (2011b). *Fluent User's Guide version 14.0*. ANSYS.
- Forchheimer, P. (1930). *Hydraulik, 3 Aurf.* Leipzig and Berlin.
- Freund, H., Zeiser, T., Huber, F., Klemm, E., Brenner, G., Durst, F. and Emiga, G. (2003). Numerical simulations of single phase reacting flows in randomly packed fixed-bed reactors and experimental validation. *Chemical engineering science*, vol. 58, pp. 903–910.
- Fricker, H.W. (1991). High-temperature heat storage using natural rock. *Solar Energy Materials*, vol. 24, pp. 249–254.
- Gauché, P. (2012). Personal communication between Guaché, P. and Louw, A. D. R.
- GeoSUN AFRICA (2012). South africa: Dni [solargis]. Online. (accessed 20 Nov 2013). Available at: <http://www.geosun.co.za/wp-content/uploads/2012/07/SolarGIS-DNI-South-Africa-Lesotho-Swaziland-PR-map.jpg>
- Guardo, A., Coussirat, M., Larrayoz, M. A., a.R.F. and Egusquiza, E. (2004). CFD flow and heat transfer in non regular packings for fixed bed equipment design. *Ind. Eng. Chem. Res.*, vol. 43, pp. 7049–7056.
- Guardo, A., Coussirat, M., Larrayoz, M. A., a.R.F. and Egusquiza, E. (2005). Influence of turbulence model in CFD modelling of wall-to-fluid heat transfer in packed beds. *Chemical Engineering Science*, vol. 60, pp. 1733–1742.

- Guardo, A., Coussirat, M., Recasens, F., Larrayoz, M. and Escaler, X. (2006). CFD study on particle-to-fluid heat transfer in fixed bed reactors: Convective heat transfer at low and high pressure. *Chemical Engineering Science*, vol. 61, pp. 4341–4353.
- Gunjal, P.R., Ranade, V.V. and Chaudhari, R.V. (2005). Computational study of a single-phase flow in packed beds of spheres. *AIChE*, vol. 51, pp. 365–378.
- Heller, L. and Gauché, P. (2012). Rock bed storage based simulation of a 5 MWe combined cycle solar power plant. In: *SASEC 2012*.
- Hänchen, M., Bruckner, s. and Steinfeld, A. (2010). High-temperature thermal storage using a packed bed of rocks - heat transfer analysis and experimental validation. *Applied Thermal Engineering*, vol. 31, pp. 1798–1806.
- Holdich, R. (2002). *Fundamentals of Particle technology*. Midland Information Technology and Publishing.
- Horn, E. (2012). *The Calibration of Material Properties for Use in Discrete Element Models*. Master's thesis, Department of Mechanical and Mechatronic Engineering University of Stellenbosch.
- IEA (2010). Technology roadmap concentrating solar power. Tech. Rep., Paris: International Energy Agency.
- Itasca Consulting Group (2003). *PFC<sup>3D</sup>: Advanced three dimensional distinct element modelling for micromechanical analysis of geomaterials and particulate systems*. Itasca Consulting Group, Minneapolis, United States.  
Available at: <http://http://www.itascacg.com/PFC3D>
- Jafari, A., Zamankhan, P., Mousavi, S. and Pietarinen, K. (2008). Modelling and CFD simulation of flow behavior and dispersivity through randomly packed bed reactors. *Chemical Engineering Journal*, vol. 144, pp. 476–482.
- Jones, M.Q.W. (2003). Thermal properties of stratified rocks from witwatersrand gold mining areas. *The Journal of The South African Institute of Mining and Metallurgy*, pp. 173–186.
- Kehlhofer, R., Bachmann, R., Nielsen, H. and Warner, J. (1999). *Combined-cycle gas & steam turbine power plants*. PennWell.
- Kröger, D. (2012). SUNSPOT the stellenbosch university solar power thermodynamic cycle.  
Available at: <http://blogs.sun.ac.za/sterg/files/2011/05/SUNSPOT-2.pdf>
- Kuroki, M., Ookawara, S., Street, D. and Ogawaa, K. (2007). High-fidelity CFD modelling of particle-to-fluid heat transfer in packed bed reactors. *Paper no. 1102, ECCE-6 proceedings CD. European Congress of Chemical Engineering, 6. ISBN 978-87-91435-57-9*.
- Lapinus (). furnace/boiler slab 590. Product information.

- Lee, J., Yoon, S., a.G. and Lee, W. (2007). Turbulence-induced heat transfer in PBMR core using LES and RANS. *Nuclear Science and technology*, vol. 44, pp. 985–996.
- Löf, G. and Hawley, R. (1948). Unsteady-state heat transfer between air and loose solids. *Indust. Engng Chem*, vol. 40, pp. 1061–1070.
- Logtenberg, S. and Dixon, A. (1998a). Computational fluid dynamics studies of fixed bed heat transfer. *Chemical Engineering and Processing*, vol. 37, pp. 7–21.
- Logtenberg, S. and Dixon, A. (1998b). Computational fluid dynamics studies of the effects of temperature-dependent physical properties on fixed-bed heat transfer. *Ind. Eng. Chem. Res.*, vol. 37, pp. 739–747.
- Logtenberg, S., Nijemeisland, M. and Dixon, A. (1999). Computational fluid dynamics simulations of fluid flow and heat transfer at the wall-particle contact points in a fixed-bed reactor. *Chemical Engineering Science*, vol. 54, pp. 2433–2439.
- Louw, A., Nel, R. and Gauché, P. (2012). A DEM-CFD approach to predict the pressure drop through an air-rock bed thermal energy storage system: Part 2 of 2. In: *SASEC*.
- Magnico, P. (2003). Hydrodynamic and transport properties of packed beds in small tube-to-sphere diameter ratio: pore scale simulation using an eulerian and a lagrangian approach. *Chemical Engineering Science*, vol. 58, pp. 5005–5024.
- Malling, G. and Thodos, G. (1967). Analogy between mass and heat transfer in beds of spheres: Contributions due to end effects. *Int. J. Heat Mass Transfer*, vol. 10, pp. 489–498.
- Mawire, A. and McPherson, M. (2007). Experimental and simulated temperature distribution of an oil-pebble bed thermal energy storage system with a variable heat source. *Applied Thermal Engineering*, vol. 29, pp. 1086–1095.
- Mawire, A., McPherson, M., van den Heetkamp, R. and Mlatho, S. (2009). Simulated performance of storage materials for pebble bed thermal energy storage (tes) systems. *Applied Energy*, vol. 86, pp. 1246–1252.
- Microsoft Corporation (2010). *Microsoft Visual Basic 6.3*. Microsoft Corporation, Redmond, WA, United States.  
Available at: <http://www.microsoft.com>
- Mueller, G.E. (1991). Prediction of radial porosity distribution in randomly packed fixed beds of uniformly sized spheres in cylindrical container. *Chemical Engineering Science*, vol. 46, pp. 706–708.
- Muirhead, J. and Eaton, A. (2013 February). DNI values in SA are amongst the best in the world. Online. (accessed 27 Feb 2013).  
Available at: <http://social.csptoday.com/emerging-markets/dni-values-sa-are-amongst-best-world>
- NASA (2008). Examining spatial (grid) convergence. Online. (accessed 27 Jul 2013).  
Available at: <http://www.grc.nasa.gov/WWW/wind/valid/tutorial/spatconv.html>

- Nel, R.G. (2013). *Discrete element modelling of packed rock beds for thermal storage applications*. Master's thesis, University of Stellenbosch.
- Nijemeisland, M. and Dixon, A. (2001). Comparison of CFD simulations to experiment for convective heat transfer in a gas solid fixed bed. *Chemical Engineering Journal*, vol. 82, pp. 231–246.
- Nijemeisland, M. and Dixon, A.G. (2004). CFD study of fluid flow and wall heat transfer in a fixed bed of spheres. *Chemical Engineering Science*, vol. 50, pp. 706–708.
- NREL (2012a). Concentrated solar power with thermal energy storage can help utilities' bottom line, study shows. Online. (accessed 25 Feb 2013). Available at: <http://www.nrel.gov/news/press/2012/2052.html>
- NREL (2012b). Concentrating solar power projects. Online. (accessed 29 Feb 2013). Available at: [http://www.nrel.gov/csp/solarpaces/by\\_country.cfm](http://www.nrel.gov/csp/solarpaces/by_country.cfm)
- Nuclear Safety Standards Commission (KTA) (1981). Kta3102.3 reactor core design of high-temperature gas-cooled reactors part 3: Loss of pressure through friction in pebble bed cores.
- Nuclear Safety Standards Commission (KTA) (1983). Kta3102.2 reactor core design of high-temperature gas-cooled reactors part 2: Heat transfer in spherical fuel elements.
- Ookawara, S., Kuroki, M. and Ogawa, K. (2007). High-fidelity DEM-CFD modeling of packed bed reactors for process intensification. *Paper no. 1102, ECCE-6 proceedings CD. European Congress of Chemical Engineering, 6. ISBN 978-87-91435-57-9.*
- Reddy, R. and Joshi, J. (2008). CFD modeling of pressure drop and drag coefficient in fixed and expanded beds. *Chemical Engineering Research and Design*, vol. 86, pp. 444–453.
- Riaz, M. (1978). Transient analysis of packed-bed thermal storage systems. *Solar energy*, vol. 21, pp. 123–128.
- Romkes, S., Dautzenberg, F., van den Bleek, C. and Calis, H. (2003). CFD modelling and experimental validation of particle-to-fluid mass and heat transfer in a packed bed at very low channel to particle diameter ratio. *Chemical Engineering Journal*, vol. 96, pp. 3–13.
- Sagara, K. and Nakahara, N. (1991). Thermal performance and pressure drop of rock beds with large storage materials. *Solar energy*, vol. 57, pp. 157–163.
- Sanderson, T.M. and Cunningham, G.T. (1995a). Packed bed thermal storage systems. *Applied Energy*, vol. 51, pp. 51–67.
- Sanderson, T.M. and Cunningham, G.T. (1995b). Performance and efficient design of packed bed thermal storage systems. *Applied Energy*, vol. 50, pp. 119–132.
- Schumann, T.W. (1929). Heat transfer: A liquid flowing through a porous prism. *Journal of the Franklin Institute*, vol. 3, pp. 405–416.

- Scilab Enterprises (2012). *Scilab: Free and Open Source software for numerical computation*. Scilab Enterprises, Orsay, France.  
Available at: <http://www.scilab.org>
- Singh, R., Saini, R.P. and Saini, J.S. (2006). Nusselt number and friction factor correlations for packed bed solar energy storage system having large sized elements of different shapes. *Solar Energy*, vol. 80, pp. 760–771.
- Singh, R., Saini, R.P. and Saini, J.S. (2008). Simulated performance of packed bed solar energy storage system having storage material elements of large size. *The Open Fuels and Energy Science Journal*, vol. 1, pp. 91–96.
- Soleymani, A., Turunen, I., Yousefi, H. and Bastani, D. (2007). Numerical investigations of fluid flow and lateral fluid dispersion in bounded granular beds in a cylindrical coordinates system. *Chem. Eng. Technol*, vol. 30, pp. 1369–1375.
- Suekane, T., Yokouchi, Y. and Hirai, S. (2003). Inertial flow structures in a simple-packed bed of spheres. *AIChE*, vol. 49, pp. 10–17.
- Thermal Ceramics (). Blanket products - product information. Product information.
- Theron, W.G. (2011). *Numerical analysis of the flow distribution within packed columns using an explicit approach*. Master's thesis, School of Mechanical and Nuclear Engineering of the North-west University.
- van Antwerpen, W., du Toit, C. and Rousseau, P. (2010). A review of correlations to model the packing structure and effective thermal conductivity in packed beds of mono-sized spherical particles. *Nuclear Engineering and Design*, vol. 240, pp. 1803–1818.
- Venter, G. (). High-performance computing at Stellenbosch University. Online.  
Available at: <https://www0.sun.ac.za/hpc/images/b/b3/Hpc.pdf>
- Verboven, P., Flick, D., Nicolai, B. and Alvarez, G. (2006). Modelling transport phenomena in refrigerated food bulks, packages and stacks: basics and advances. *International Journal of Refrigeration*, vol. 29, pp. 985–997.
- Versteeg, H.K. and Malalasekera, W. (2007). *An Introduction to computational fluid dynamics the finite element method 2nd edition*. Pearson Education Limited.
- Vortmeyer, D. and Schaefer, R.J. (1974). Equivalence of one- and two-phase models for heat transfer processes in packed beds: one dimensional theory. *Chemical Engineering Science*, vol. 29, pp. 485–491.
- Wakoa, N., Kagueli, S. and Funazkri, T. (1979). Fluid dispersion coefficients on particle-to-fluid heat transfer coefficients in packed beds. *Chemical Engineering Science*, vol. 34, pp. 325–336.
- Yang, J., Wang, Q., Zeng, M. and Nakayama, A. (2010). Computational study of forced convective heat transfer in structured packed beds with spherical or ellipsoidal particles. *Chemical Engineering Science*, vol. 65, pp. 726–738.

Zanganeh, G., Pedretti, A., Zavattoni, S., Barbato, M. and Steinfield, A. (2012). Packed-bed thermal storage for concentrated solar power - pilot-scale demonstration and industrial scale design. *Solar Energy*, vol. 86, pp. 3084–3098.

Zavattoni, S.A., Maurizio, C.B., Pedretti, A. and Zanganeh, G. (2011). CFD simulations of a pebble bed thermal energy storage system accounting for porosity variations effects. In: *SolarPACES*.

Zho, R.P. and Yu, A.D. (1995). The packing of spheres in a cylindrical container: The thickness effect. *Chemical engineering science*, vol. 50, pp. 1504–1507.